DOCTEUR EN SCIENCES

A biomimetic approach for improved light extraction from solid-state sources: from fireflies to light-emitting diodes

Bay, Annick

Award date:
2013

Awarding institution:
Universite de Namur

Facultés Universitaires Notre-Dame de la Paix

Faculté des Sciences

Centre de Recherche en Physique de la matière
et du Rayonnement (PMR)

Laboratoire de Physique du Solide (LPS)

A biomimetic approach for improved light extraction from solid-state sources: from fireflies to light-emitting diodes

Thèse de Doctorat
présentée par
Annick Bay
en vue de l'obtention du grade
de Docteur en Sciences

Composition du Jury

Prof. Jean Pol Vigneron (*Promoteur,* Research Center in Physics of Matter and Radiation, LPS, FUNDP)
Prof. Laurent Houssiau (*Président*, Research Center in Physics of Matter and Radiation, LISE, FUNDP)
Prof. Serge Berthier (Institut des Nanosciences de Paris, France)
Dr. Dimitri Deheyn (Scripps Institution of Oceanography, UCSD)
Prof. Olivier Deparis (Research Center in Physics of Matter and Radiation, LPS, FUNDP)
Prof. Laurent A. Francis (Sensors, Microsystems and Actuators Laboratory of Louvain, UCL)

Avril 2013

University of Namur
Faculty of Sciences, Physics Department
Rue de Bruxelles 61, B-5000 Namur, Belgium

A biomimetic approach for improved light extraction from solid-state sources: from fireflies to light-emitting diodes

by Annick Bay

Since their first use, solid-state lighting devices have received a growing interest and popularity from engineers, physicists, industry and consumers. Their promising *internal* efficiencies, i.e. the high conversion rates of injected current to produced light, make them very appealing for the replacement of incandescent or fluorescent light sources. The major challenge for the development of these light sources is to enhance the *external* light extraction: the active material of light emitting diodes is in general a semiconductor with a high refractive index, which considerably limits the extraction of light into free space due to total reflexion. This lack of high external efficiency has generated an important amount of research and publications. Very different approaches have been considered to enhance the external light extraction efficiency: photonic crystals, photonic structures inside and above the active material, graded refractive index layer to reduce the high index contrast between the active material and air, plasmonic resonances and more.

In the present research, the bioluminescent organ's morphology of a Panamanian firefly is used as a source of inspiration to improve the light extraction efficiency of light-emitting devices. The internal efficiencies of light-emitting devices are nowadays very high, yet, the overall efficiency is limited by the total internal reflexion due to the high refractive index of the incident medium. Fireflies emit light in their dense bioluminescent organ and light extraction is equally limited by total internal reflection. During their million years of evolution, the bioluminescent organ had the time to improve both, its internal functioning and its light extraction efficiency.

The thorough analysis of the lantern's morphology shows several structures added on the light path, that could influence the light extraction efficiency. The jagged scales form a micrometric, two-dimensional and asymmetric structure which is shown, through simulations, to influence the light extraction positively. The new arrangement of the interface leads to a considerable increase in the light extraction efficiency. A similar analysis is then carried out with a two-dimensional and a three-dimensional symmetric structure. From the simulations it has been concluded that the firefly inspired structure is the most suitable for fabrication on light-emitting diodes. In the framework of a collaboration with microelectronics experts, the jagged-scale structure inspired from fireflies has been adapted to enhance the light-extraction efficiency of an GaN-based LED. Measurements confirm tendency that light extraction increases, as predicted by the simulations.

Université de Namur
Faculté des Sciences, Département de Physique
Rue de Bruxelles 61, B-5000 Namur, Belgium

Approche biomimétique pour l'amélioration de l'extraction de lumière des sources LED: des lucioles aux diodes électroluminescentes

by Annick Bay

Les diodes électroluminescentes ont reçu un intérêt croissant de la part des ingénieurs, physiciens, industriels et consommateurs, depuis leur première utilisation. Leur efficacité interne élevée, c'est-à-dire le taux de conversion élevé de courant injecté en lumière émise, les les place en bonne position pour remplacer les sources lumineuses incandescentes et fluorescentes. Une limitation persiste néanmoins sur l'efficacité globale de la diode: les matériaux actifs ont des indices de réfraction élevés par rapport au milieu émergent (l'air), ce qui limite considérablement l'extraction de lumière, et ainsi l'efficacité externe, à cause du phénomène de réflexion totale. Ce manque d'efficacité externe a généré une activité de recherche considérable avec une grande variété d'approches différentes pour résoudre le problème: cristaux photoniques, structures photoniques dans et au dessus du milieu actif, couches d'indice de réfraction adaptative pour réduire le contraste élevé entre le milieu incident et émergent.

L'organe bioluminescent d'une luciole du Panama est utilisée comme source d'inspiration pour l'amélioration de l'efficacité d'extraction de lumière des diodes dans la recherche présentée dans ce manuscrit. La lumière émise par les lucioles est générée chimiquement dans son organe bioluminescent, qui présente un matériau dense par rapport à milieu émergent (l'air). Pendant les millions d'années d'évolution, l'organe bioluminescent a pu avoir le temps d'améliorer son fonctionnement interne ainsi que l'extraction de lumière, c'est-à-dire son efficacité externe. L'étude morphologique de la lanterne a montré différentes structures qui peuvent influencer la propagation de la lumière entre l'organe émetteur et l'air libre. Les écailles inclinées forment un réseau micrométrique, bidimensionnel et asymétrique. Les simulations associées montrent que cette structure augmente considérablement l'extraction de lumière. Une analyse similaire est conduite pour deux modèles inspirées: une structure triangulaire (bidimensionnelle et symétrique), ainsi qu'une structure pyramidale (tridimensionnelle et symétrique). Les simulations permettent de conclure que la structure à écailles inclinées de la luciole est la mieux adaptée à la fabrication. Dans le cadre d'une collaboration avec des experts en microélectronique, la structure à écailles inclinées, inspirée par les lucioles, a été adaptée pour augmenter l'efficacité d'extraction de lumière d'une diode basée sur le GaN. La mesure réalisée confirme la tendance prédite par les simulations.

"*Be yourself! Everyone else is taken.*"
Oscar Wilde

"*Creativity is intelligence having fun.*"
Albert Einstein

Acknowledgments

First of all I would like to acknowledge my supervisor, Prof. Jean Pol Vigneron. This whole magnificent journey starting as a Master thesis could not have taken place without him. He gave me, during the pasts four years, the possibility to develop myself and supported me when needed. I would never have expected that a PhD in *Physics* would have led to all these great expeditions and experiences I had. Who could have known that we would go into the jungle to collect our samples? I really do believe in a biomimetic approach and this thesis was a great apprenticeship, both, for the science and as well from a personal point of view. Thank you for this beauiful opportunity!

I met Serge Berthier during the preparations of my first expedition in the tropics. This "Voyage des Masters" in French Guiana was a marvelous experience. The following years Serge gave me interesting comments and suggestions to complete the present work. He also gave me nice opportunities, such as talks at the very prestigious "Fondation Les Treilles" in Tourtour, France.

Michael Sarrazin has contributed significantly to the advancement and understanding of the simulations and I'm glad he joined our team during my PhD thesis. I am impressed by his drive and efficiency to solve given problems.

The collaboration carried out with Dr. Nicolas André to adapt and then create the factory-roof pattern of the firefly on an LED was a really enriching experience. It was a pleasure to work with Nicolas and I am really happy that this project turned out so well. In this framework, I would also like to thank Prof. Laurent Francis (UCL) and Prof. Vincent Aimez (University of Sherbrooke) who helped realize this biomimetic project.

A special thanks goes as well to Donald Windsor, entomologist at the Smithsonian Tropical Research Institute (STRI), who impresses me with his ability to spot *Charidotella* from his moving car. He is a great mentor for the field studies and his insights into entomology are precious.

Olivier Deparis pertinent remarks are beneficial to every work and indeed, as well to the present research.

Jeff Colomer, my dear colleague of the "Bureau de l'Essellence", taught me all the important aspects of the electronic microscopy and spend hours and hours with great patience during my Master thesis in front of the *JEOL*. The only questions we really don't agree on are the office temperature and style...

Cédric Vandenbem and Marie Rassart - who really surprised me at the end of Marie's public defense (!) - deserve as well a huge place in these acknowledgments. With Marie I went to my

first Spring School and Conference, a quite impressive experience when you are still a Masters student... We, “Cake Girls”, ruled the lab and when Marie left, I took over her role of “G.O.”. Now, that we take diving classes together, you are in a certain way again my “mentor”. Cédric always gave me interesting input for the completion of my thesis. I am really happy that I could be part of this “Bureau de l’Excellence” with him for three years.
Talking about the “Bureau de l’Excellence”, I am so glad that Lucie Gaouyat joined me and helped me defend style and room temperature against my opponents! It really missed a girlish touch in this office, which is now successfully installed.
During both stays at the European Synchrotron Radiation Facility (ESRF) in Grenoble, Peter Cloetens, Heikki Suhonen and Julie Villanova were dedicated to make our, quite complicated, experiments work at its best. These experiences clarified our SEM observations on the fireflies - and other insects - and I’m amazed of the efficiency of this experience and the operating of the ESRF.
Without the precious help of both, our system manager Frédéric Wautelet and our informatics correspondent Isabelle Derycke the outcome of my thesis would have been a little bit harder. The assistance offered by both of them for every problem were essential. You were of great help and as you said Isabelle: “There’s a solution to every problem!”. Verified on March, 25^{th} 2013.
I would like to give a special thanks as well to Eliane Richter, who was willing to read some parts of this manuscript. Moreover, she was a great help for the preciseness of the project statements submitted parallel - and in a great, great rush - to this manuscript. Be sure, there will be room for you in San Diego!
Victoria Welch gave me several precious informations about biological aspects or simply about basic English grammar rules.
I would like to as well recognize my Masters Classmates: Ben, Eloise, Anne-Catherine and Ivan. We had a great time during the last year of our studies: don’t forget about French Guiana, Budapest, our numerous trips to Paris and so on... The special TPPT courses were as well captivating: We had to bring in Serge especially from France... by the way, why not revive this memory soon?
All the members of the LPS laboratory made me feel welcome from the beginning and I enjoy being part of this laboratory. I hope I helpe contribute to the good vibe of the lab. Don’t forget, there is still one trip I think - I hope - I will help organizing before leaving: our next “Weekend de Labo” in Grenoble. Close to Anastasia.
Talking about Anastasia, I would like to thank as well the various running companions. This breath of fresh air at noon has (and is) a very important moment in the day, where stress and negative feelings can be shaken off. It all started with Jeff, Cédric, Luc and myself. Anastasia, Jeff’s sparkly post-doc, showed us how Russians run... The running sessions with Nicolas G. were the most beneficial, as we really cleared our minds in these 50 minutes. Now, the LISE has reinforced our training group and I am really fond that Xavier and Alex pushed me (before writing my thesis...) to achieve my best performance so far. From now on: training starts again and I wanna go even faster and further.
The BTS Team was also a good moral support through this amazing, but also sometimes quite

tough experience, which is the PhD. Their main actors, i.e. JD, Nicolas G. and the 131D School Of Physics (Mika, Steevo and Seb) really knows how to enlighten a gray grad student's day. Looking forward to see the new shirt!
I may not forget my friends, die Mädels: Claire and Cathy, my favorite twins full of good ideas for nice pranks. Claire and Vivi, I'm happy that we spend these last three and a half years together in Brussels. Vivi, let's go out more, as we said... Claire, don't worry, there will always be the inflatable mattress for you when you need to come back here to defend a cause that is close to your heart... I would like to give Anne and Babsy all my best wishes for the whole new journey they went on! It's just crazy, how everything evolves. I'm so happy for you! Anti, it's always fun to talk with you about the future, the possibilities and benefits of traveling and the "fourmis dans le c**". Jutte and Bella, our close friendship lasts now for several years and it even stays over long distances. Bella, our trip to India was reviving, gave me a lot of motivation and a whole new point of view. It put my feet back on the ground and the heart at the right place. Let's redo this! Jutte, we know for so long now, even if we were maybe not always "best friends" (You remember that??? Crazy!). However, during these last years our friendship got undoubtedly stronger through our shared experiences. And you are and will always be the girl who I talk the most to on the phone... Girls, you are a really important part of my life and I am glad, that you are there for me, in the same manner, as I will always be there for you... When is the next Schlomme???
Lucie T., its such a pleasure to go for a coffee, cake or a drink with you. Our nice little talks are always refreshing. And don't forget: "We NEED you to party!". Noemi, I'm happy that we started diving together and I'm sure that we are going to enjoy Brussels a little more this year! Looking forward to picnics in the summer... This list of friends is not extensive!
I'm glad as well to stay in touch with people I met during my studies. Louise, we spend a lot of time together during our studies and you inspired me with your ambition. Gaëlle and Xavier, small improvised dinners are always nice... and I know what to bring next time again: *Nero d'Avola* and *Coconut MeloCakes*! Not to forget the "Scapakot" girls (Lise, Flo and Careau) and the "Kot RUN" crew (Hélène, Camille, François, Nicolas, Guillaume and Jérémie)!
My family takes a huge place in my life as well. I would like to thank my parents for the support they gave me over all these years. Without you, I would never have gotten so far, as you gave me the basics, through my education, to achieve this work. As said Albert Einstein "Rejoice with your family in the beautiful land of life!". Charles, I'm so looking forward to our Milano trip!!!
Last, but surely not least, I'm going to thank Cristian, for being my closest friend, my charming entertainer, my shoulder to cry on and much more! I love you and spending time with you... Your support was essential during this difficult time and you can count on a compensation for these lots of "bad mood" and "Zickereien"!

Contents

Introduction

Luminescence

Broadly speaking, light sources can be classified as "hot" or "cold". The hot sources are those that rest on the production of Planck radiation from heated object [1]. The problem with these sources is that their temperatures should be high enough so that they can reach a significant amount of visible light. Typically, tungsten filaments (Fig. 1(a)) can be heated at temperatures high enough to allow for a reasonable performance but are limited by the metal evaporation rate, and by the metal's melting point (3422 °C). Close to the melting-point limit, the maximum Planck emission is still in the far infrared and much of the consumed energy ends up as heat without being turned into visible light. A halogen lamp addresses this efficiency concern, but in a quite indirect way: a small amount of gaseous iodine or bromine produces a chemical reaction in which tungsten is deposited back on the filament as it evaporates [2]. This does not only lengthen the lifetime of the lamp and keep the transparent envelope clean: it also allows for higher temperatures, with the consequence that the proportion of visible light in the global Planck spectrum is increased. Still, a large fraction of the emitted energy remains in the form of invisible light and heat. Cold sources implement a process called *luminescence* [3]. In this process, energy is delivered from various power sources to the electrons in the active material. The excitation energy is higher than those required for emitting visible photons, so that the restoration of these electrons to lower-lying energy states produces light with, usually, the excitation of available vibronic states, a process that limits – slightly – the energy conversion into visible radiation. `Luminescence` is then the production of light with very limited losses under the form of heat.

Luminescence is actually a transduction, i.e. the transformation of one form of energy into another, here visible photons. Several classes of luminescence have been identified, according to the origin of the primary energy : in *photoluminescence*, the excitation energy is received from short-wavelength light, such as ultraviolet. We distinguish *fluorescence* (Fig 1) from *phosphorescence* by the time delay between the primary photon absorption and the secondary, longer-wavelength, photon emission [4]. Following primary absorption, the electrons are promoted, in about 10^{-15}s to an excited singlet state (with paired spins) with vibrational excitation. The vibrational excitation is eliminated in 10^{-13} to 10^{-10} s, and internal conversion drives the excitation to the lowest singlet state in about the same time, much shorter than the final excited singlet state lifetime, of the order of 10^{-7} s. This is the time needed for the

electron to return to its ground state by emitting the fluorescence photon. Due to the emission of far-infrared radiation when eliminating vibrational excitation, the emitted photon has less energy – and longer wavelength – than the primary absorbed photon. In certain systems, the electrons on this final lowest singlet state can cross to a triplet state if its energy matches one of the triplet's vibrational state. In this case it ends up, in a time shortened by electron-phonon interaction, to the resting (vibrationless) triplet state, where it can stay for 10^{-4} to 10 s or even longer. In rigid solid-state environments, where collisional exchanges are minimized, radiative return to the ground state can only take that path. This is phosphorescence, involving a long-lasting energy storage before the emission of secondary photons.

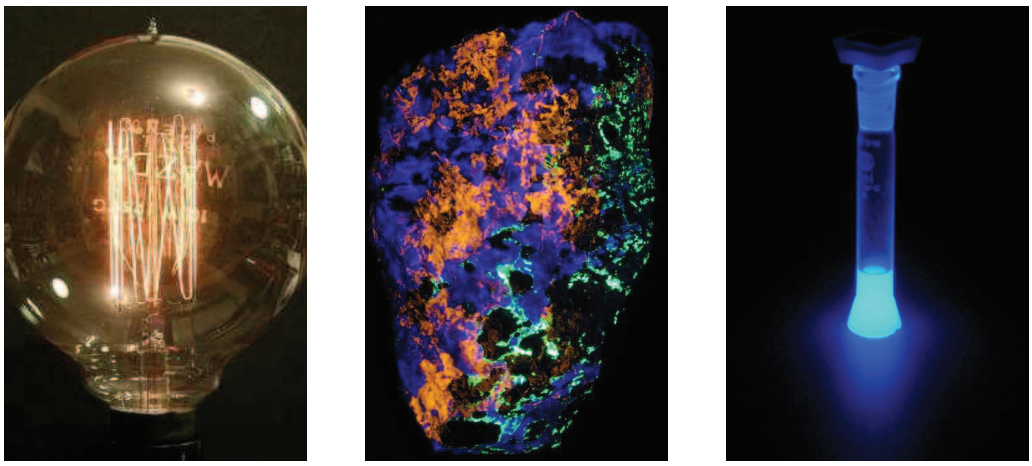

(a) Tungsten lamp

(b) Fluorescence in hardystonite

(c) Chemiluminescence of Luminol

Figure 1: Examples of light production

In *radioluminescence*, light is produced by the bombardment of a "phosphor" with ionizing radiation. This involves the excitation of an electron that belongs to atoms on the trajectory of a fast charged particle. Tritium, for instance, is a radioactive beta emitter with a half-life of 12.32 years [5]. In presence of a radioluminescent phosphor, it can produce light for 10 to 20 years. This is the way to make self-luminous paint, actually used today in exit signs, wrist watches, instrument dials... intended to be read under dim light. A *spinthariscope* is a radiofluorescent screen designed to help the detection of energetic charged particles. Radium-based luminescent materials were also used in the past, but have been left aside because they were found to be potentially hazardous to workers in their production plants.

Triboluminescence (and its more specific version *fractoluminescence*) needs mechanical action on the active material [6] such as the disturbance of surfaces by friction or creation of surfaces by fracture. The faint light emitted when breaking agglomerated sugar, rubbing quartz crystals, or rapidly peeling off a roll of scotch tape are examples of this effect. Using pressure on a piezoelectric crystal also generates light, a phenomenon referred to as *piezoluminescence*. Ferroelectric polymers have been shown to exhibit piezoluminescence and this phenomenon has also been reported in alkali halides, such as NaCl, KCl, KBr [7]. These need to be irradiated in

order to break the centro-symmetry at places, in order to allow for a piezoelectric coupling.

Finally, the kind of luminescence we will be interested in here is caused by the delivery of energy through a chemical reaction. This is *chemiluminescence* [8] (Fig 1(c)). If this reaction takes place in a living organism, this form of light production is referred to as *bioluminescence* (see the next section). Probably the best known example of an artificially synthesized chemiluminescent compound is luminol ($C_8H_7N_3O_2$), activated by an oxidant such as hydrogen peroxide (H_2O_2). The oxidation reaction can be catalyzed by iron, a fact that leads to an important application in forensic investigations: the luminescence reaction is used by criminalists to detect traces of blood at crime scenes. Spread uniformly over the suspect surface, the mix of luminol and peroxide reacts more effectively at sites where hemoglobin (an iron compound) has been deposited. `Bioluminescence` follows a similar reaction : in simple terms, the oxidation of luciferine in presence of a catalyst, the enzyme luciferase.

Bioluminescence

Light has been tremendously important to the genesis and the evolution of life. Plants use light for photosynthesis, taking carbon out of atmospheric dioxide to produce their constituting materials. The oxygen then released to the atmosphere is important for nearly all organisms, which themselves use light for thermal regulation, communication and more. Visual messages are important, for example, in defense strategies, in territory protection and in mating acceleration.

But what if sunlight disappears, at dawn, in caves or in the deep sea? Do living organisms use another carrier for information exchange? They surely do this in some cases, like bats, who use echolocation with acoustic waves to explore their environment [9]. But some organisms did better: they saved their vision capability by producing light from bioluminescence. This very efficient light production helps the organisms to avoid predation in many ways, to send toxicity signals, to help catching food, to attract potential mating partners and so on.

Marine Bioluminescence

Bioluminescence is present in the major groups of marine organisms and is distributed throughout all oceans from the deep-sea `benthic zone`[1] up to the surface, through the entire water column. The bioluminescence is specific for each of these different zones (`bathyal` benthic, `pelagic`,...) where organisms have to adapt to very different conditions [10]. Most marine animals use bioluminescence as primary visual stimulus and it is often produced by intrinsic `photophores`, rather than bacterial symbionts.

The variety is extraordinary: the anglerfish *Melanocetus johnsoni* (Family: Ceratioid) has a bioluminescent lure in front of its mouth (the *illicium*) to attract prey in the pitch-black darkness of the deep sea [11] (Fig. 2(a)). The deep-sea flashlight fish, *Photostomias guernei* (see Fig.

[1] Terms printed in `typewriter` font are explained in the Glossary at the end of this manuscript.

(a) Anglerfish *Melanocetus johnsoni*

(b) Dragonfish *Photostomias guernei*

(c) Squid *Abralia veranyi*

(d) Deep-sea shrimp *Parapandalus* sp.

(e) Venus fly trap anemone *Actinoscyphia*

(f) Ostracod *Vargula* sp.

(g) Brittlestar *Ophiochiton ternispinus*

(h) Dinoflagellates *Pyrodinium bahamense*

(i) Cnidarian *Aequora* sp.

Figure 2: Examples of bioluminescence in the sea.

2(b)), uses its bioluminescence equally for prey attraction and intra-specific communication [12]. The bioluminescence in these two cases is a result of symbiosis with bioluminescent bacteria (symbiotic photophores). But light can as well be created in the so-called intrinsic photophores, which are photogenic cells. An interesting example for the use of intrinsic photophores is the lantern shark (Family: Etmoperidae) [13]. The abdomen of this deep-sea fish is covered with photophores that lighten up to mimic the movement of the water surface and let the fish nearly disappear from the view of other organisms at greater depths. Certain cephalopods (Mollusc), such as *Abralia veranyi*, use as well this specific technique of mimicking the water movement to make themselves non-conspicuous to other organisms (Fig. 2(c)) [14]. About 70 luminous genera have been identified among the squids. Except for two species, the bioluminescence is produced by intrinsic photophores. Cephalopods use bioluminescence for counter-illumination, to distract predators, stun prey or for intraspecific communication. Osborn *et al.* report of a deep-sea swimming worm (*Swima bombiviridis*, Annelid:Polychaete) who is able to eject a bioluminescent "bomb" in order to distract and thereby escape its predators [15]. A similar

behaviour has been observed for a deep-sea shrimp *Parapandalus* sp. and a venus flytrap anemone *Actinoscyphia* sp. [10] (Fig. 2(d)-(e)). Ostracods, *Vargula norvegica* (Crustaceans), are also reported to eject a viscous light-emitting substance when seen in presence of their predators (Fig. 2(f)), deep-water eels (*Synaphobranchus kaupii*) [16].

The echinoderm group contains as well several bioluminescent groups, such as brittle-stars [17] (see Fig. 2(g)). Bioluminescent bacteria are common in the ocean and can create symbiotic bonds with other organisms, as seen in the example before. A well-known phenomenon related to bacterial bioluminescence is the so-called milky sea, where large areas of seawater glow at night due to the presence of such bacterias probably in combination with a microalgal bloom [18]. Dinoflagellates, like *Pyrodinium bahamense*, are unicellular organisms that emit light when disturbed [19] . This can lead to spectacular light emission in the sea with the movement of the waves (Fig. 2(h)), the wake of a boat or even turbulences created by a swimmer. Other groups of marine organisms that have been reported to include bioluminescent genera are Radiolarians, Cnidarians and Tunicates [20]. The phyla of Cnidarian got a special attention in 2008 as the Nobel price in Chemistry was attributed to three researchers (Shimomura, Chalfie and Tsien) for their discovery and development of the green fluorescent protein (GFP) from *Aequorea victoria* (see Fig. 2(i)) The bioluminescence is mainly blue in the sea. However red and yellow marine bioluminescence has been reported as well: *Tomopetris* (Annelids: planktonic polychaete worms) emit a golden yellow glow, when disturbed.

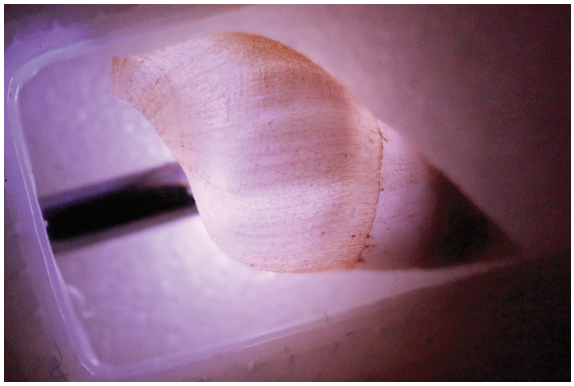

Figure 3: Shell of *Hinea brasiliana* illuminated by a Halogen-Deuterium source through an optical fiber. The illumination is homogeneous over the whole shell, by contrast to other species.

Another interesting case of bioluminescence in the sea is reported by Deheyn *et al.* [21]. The sea snail *Hinea brasiliana* emits light to deter its predators. The light organs are located in very limited spots on the snail-body. However, the entire shell lits up with equal intensity. The same observation is done when putting an optical fiber in the snail-shell: the light is equally distributed over a large part of the snail's shell (see Fig. 3). This contrasts the polished shell of an abalone (composed of the same material, aragonite) where the light is transmitted, but not scattered. This leads to the assumption, that the shell of *Hinea brasiliana* has a specific structure which scatters light very effectively. The applications of such a structure are numerous, first of all to create scatters ambient light from very punctual light sources like LED's.

Terrestrial Bioluminescence

On earth, bioluminescence is less common. Among terrestrial bioluminescence, insects are the main group with luminescent species. Out of about 35, only three phyla have been described to include bioluminescent genera: Annelida, Mollusca and Arthropoda. Most terrestrial bioluminescence is found in the Insecta class (Arthropoda). The larvae of *Arachnocampa* sp. (Diptera), a fungus gnat, is found in dark, damp places such as caves from New Zealand (*A. luminosa*) and Australia (*A. richardsae, A. flava and A. tasmaniensis*) [22]. Their use of bioluminescence is spectacular: vertical fishing lines (snares) hang out of their nests, holding droplets of sticky mucus to catch prey. The nest of the gnat is about 2.5× the size of the larvae (about 3 cm) and includes up to 70 snares. To attract prey the larvae produces blue-green light in its bioluminescent organs, diffracted by the droplets of mucus (see Fig. 4(a)). Viviani *et al.* report of another fungus gnat, *Orfelia fultoni*, found in North America and different by its bioluminescent organ as well as by the light producing chemical reaction [23]. Another example of the Insecta class are click-beetles of the genus *Pyrophorus* (Elateridae). They are found in tropical and subtropical America, emit light when flying and when disturbed. The particularity about this bioluminescent insect is the striking light color polymorphism [24]: two bioluminescent spots are located on the dorsal side of their `pronotum` which emit green to yellow-green light. One other bioluminescent spot is located on the abdomen and emits yellow-green to orange light. It is quite difficult to see this third bioluminescent organ as it is hidden by the elytra and only visible during the flight. Its light emission is seen over long-distances in the dark forest of subtropical regions. The railroad worm *Phrixothrix hirtus* (Phengodidae) is particular as it emits yellow-green bioluminescence on its body but orange-red on its head (Fig. 4(d)) [23]. The reaction substrate, called luciferin, is the same, but the enzyme, luciferase, is different for the two emissions. The bioluminescent earthworm *Diplocardia longa* on Fig. 4(c) is an example of bioluminescence for Annelids [25].

The most popular bioluminescent species on earth is probably the firefly, which lights up warm summer evenings in our regions and in nearly all temperate or tropical zones. DeCock describes the larval and adult emission of three European fireflies (Lampyridae) species: *Lamprohiza splendidula*, *Lampyris noctiluca* and *Phosphaneus splendidula* [26]. The green-yellow light emitted by these species peaks at 546 nm.

Beside insects, freshwater bacteria *Vibrio chloreae* and terrestrial bacteria *Photorhabdus luminescens* has been reported to emit light [27,28]. Altough the knowledge of the biochemistry and genetics is quite extensive for bioluminescent bacteria, the physiological function of the bioluminescent system is not well understood. One hypothesis claims that the luminescent character plays a role in the dissemination of the bacteria through feeding animals. Other hypothesis include a detoxifying reaction as luciferase activity can consume a large amount of oxygen [29].

In New Zealand, the limpet *Latia nerotides*(Mollusc), emits a greenish luminescent mucus

when disturbed [30]. The land snail *Dyakia striata* (Mollusc), also known as *Quantula striata* is found in most regions of southeast Asia and has been reported by Counsilman and Ong (1988) as the only luminescent terrestrial gastropod [31].

Currently around 80 luminescent fungal species are known, spread over the globe [32]. *Mycena chlorophos* (Basidiomycetes), a luminescent fungus of subtropical areas of Japan, emits continuously light with a maximum wavelength of about 530 nm [33] (Fig. 4(f)). Bioluminescent fungus of Basidiomycetes are found growing on decaying wood or leaves which gives them their common name "glow wood" [34]. Up to now, the ability of emitting light has never been reported for flowering plants nor terrestrial vertebrates like birds, amphibians or mammals.

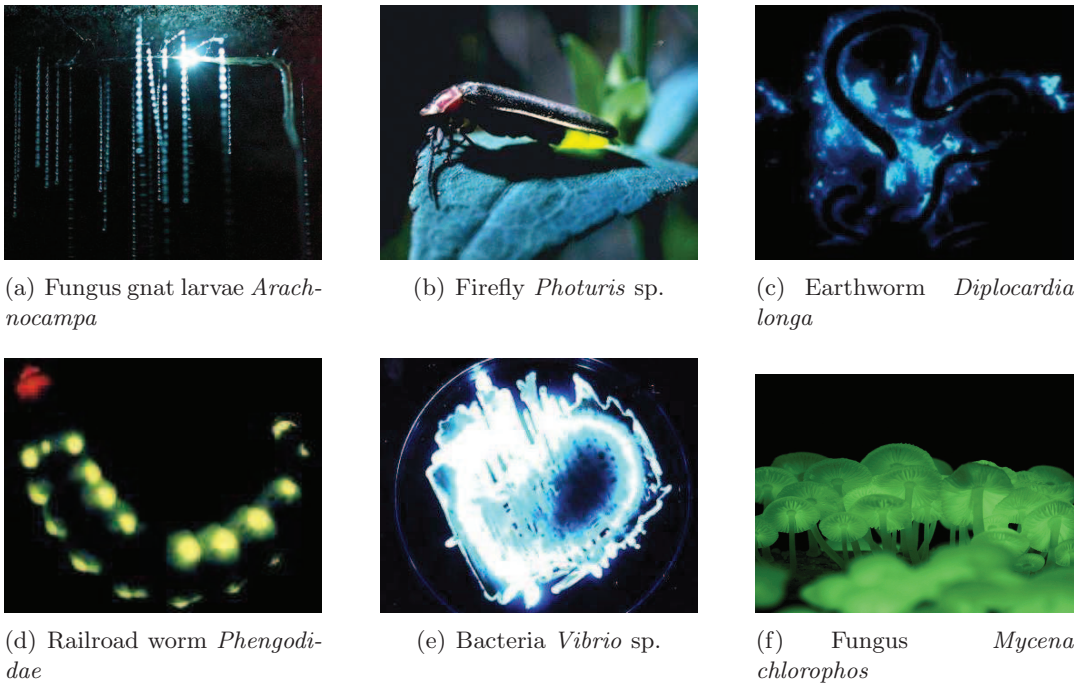

(a) Fungus gnat larvae *Arachnocampa*

(b) Firefly *Photuris* sp.

(c) Earthworm *Diplocardia longa*

(d) Railroad worm *Phengodidae*

(e) Bacteria *Vibrio* sp.

(f) Fungus *Mycena chlorophos*

Figure 4: Examples of terrestrial bioluminescence

Bioluminescence is very abundant in the ocean and rather rare in terrestrial zones. One point should be noted: in both cases, marine and terrestrial bioluminescence, the ability to produce light originated several times during evolution, which is reflected in the biological and biochemical diversity and its sporadic `phylogenetic` distribution [35].

Spectral distribution and photophore diversity

This considerable diversity in bioluminescent species is somehow reflected in the distribution of the emission color varying as a function of the organisms habitats (see Fig. 5(a)). On earth, the bioluminescence is mainly found in the green-yellow range of the spectrum (510 - 590 nm) such as fireflies and fungi, but exceptions emit blue (*Diplocardia longa*) or red-orange light (back lantern of *Pyrophorus*). The coastal, shallow regions of the sea receive considerable amounts

of sunlight during the day and the maximal emission is shifted to the green-blue range of the spectrum (490 - 520 nm) in comparison to terrestrial light emission *Hinea*). In the `pelagic` zone the bioluminescence is mostly present in the blue range (450 - 490 nm). Blue light, which has a shorter wavelength than green and yellow light, can penetrate deeper through the water, due to lesser absorption and scattering than longer visible wavelengths. This can explain why blue is the dominant emission color of the pelagic organisms. In the deep sea, up to 1000 m, the little sunlight that remains is also mainly blue. The sensitivity of most of these organisms is therefore limited to blue light, but several living species take this limitation as advantage by emitting red (and therefore invisible) light screening the ocean to search for food or escaping their predators.

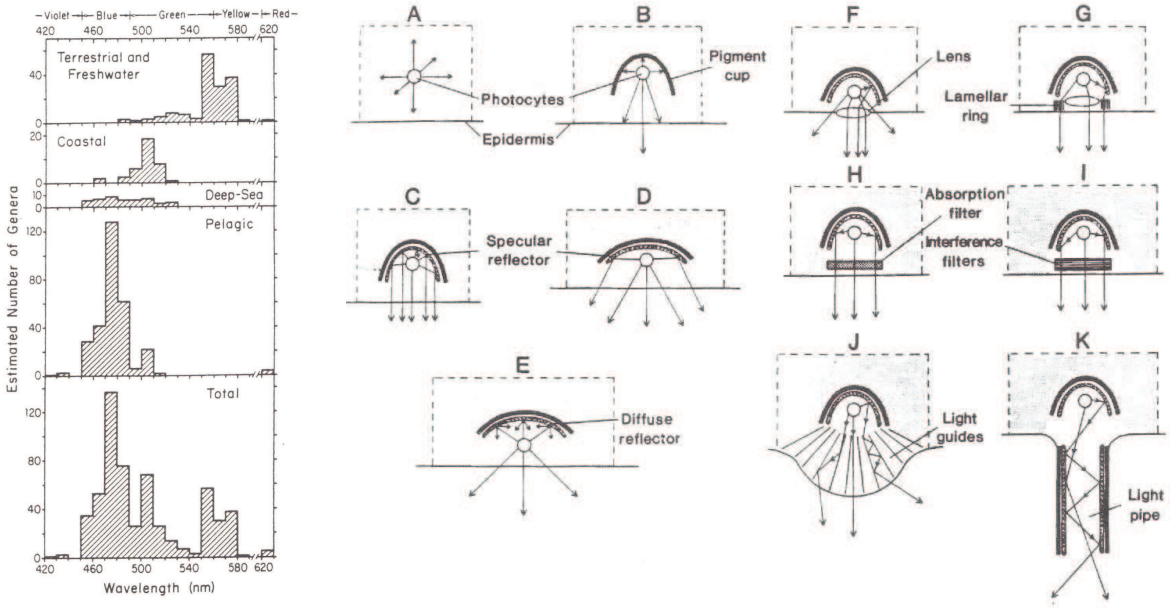

(a) (b)

Figure 5: (a) Distribution of the emission spectra maximal of bioluminescent terrestrial and marine genera estimated by Hastings and Morin [36]. (b) Diversity of the photophores (Credit: Hastings et Morin [36])

Dove *et al.* show in their work a strong similarity between the focusing lens of the photophores and the lens used for visual perception in the midshipman fish *Porichthys notatus* [37]. The photophore and the eye lenses share a similar developmental origin and an analogous function. The bioluminescence of this fish is essential for anti-predatory counterillumination and therefore essential for the specie's preservation. These two evidences gives a strong indication that the photophores in this genus have *evolved* to this stage of complexity.

Figure 5(b) shows different types of photophores, more or less complex. The basic photophore (Fig. 5(b) A) is simply a group of `photocytes`, where light is emitted homogeneously in all directions. The photophore represented in Fig. 5(b) B has a pigmented layer which absorbs light emitted away from the outer interface. This allows to avoid the transmission of the light through the organisms body, eventually translucent, as in the case of Ctenophores or

Cnidarians. Adding a reflective layer helps to increase the part of emitted light that reaches free space (C-E). Adding outer lenses, interference filters and light guide scatterers, the photophores become more and more complex (F-K), in combination with the use of muscles to focus lenses, open/close shutters, deform the photophore shape... From this growing complexity in the different photophore types and the importance of the bioluminescence function of the species preservation, we can consider that the bioluminescent organ is subjected to evolutional improvements. Further it is reasonable to assume that terrestial organisms have been subjected to similar evolutional improvement processes.

Terrestrial bioluminescence, physics and technology

The emission of light by living organisms is a form of a chemiluminescence which takes place in an optically dense material. The physics of this process can be paralleled with a technology endeavor: the construction of cold light sources from semiconductor. Light emitting diodes are based on electron-hole recombination at a semi-conducting junction. The quantum yield of this process is very high but the external efficiency is, as in the biological lantern, limited by optical constraints such as total internal reflection. The light extraction problem is especially important for terrestrial bioluminescent organisms as the emergent medium is air with a refractive index of n_{air}=1. For sea organisms the interface with water is less reflective and the total internal reflexion is therefore less restricting. Terrestrial organisms that deliver bioluminescence are on earth since at least a hundred million years [35]. Because of the biological importance of the emission of light for these animals, it can be expected that evolution has optimized the extraction of light. This represents a strong reason to examine closely the structure and optical efficiency of the lantern. It is the purpose of the present work: In a first step we analyze the morphology and optical behavior of a specific firefly lantern. It will be important to investigate thoroughly the optical behavior in order to determine how far this biological device stands from an ideal case. Building on this understanding, we will not only suggest a way to improve existing light-emitting diodes, but also describe a prototype of overlayer, which, as an artificial firefly cuticle, allows for a better external emission efficiency.

This work is based on a `biomimetic` approach. Lepora *et al.* define "biomimetics" as *"the development of novel technologies through the distillation of principles from the study of biological systems*" [38]. A formal study of biological processes and mechanisms can be used as a model for designing and creating synthetic materials and structures with similar properties by transferring biological functions. The subject has known an explosive growth in the first decade of this century with a number of published paper doubling every 2-3 years. In the mid-1990s less than 100 papers were published. Currently, the number of published papers in this field reaches 3000 per year. Biomimetic subjects are present in different fields and can be found in several conferences, such as the SPIE (International Society for Photonics and Optics), ROBIO (Robotics and Biomimetics) or the EMBS (Engineering in Medecine and Biology Conference). In the present work, the biomimetic approach is focused on *photonics*[2]. Biomimetic applica-

[2]Photonics is derived from the Greek *photos* "light" and the ending *-ics*, which indicates a research field [39].

tions in photonics include the creation of an anti-reflective layer by nanoimprint lithography inspired by the moth-eye structure [40] to increase the performance of solar cells; *Morphotex*, an unstained, structurally colored and iridescent textile using interference structures similar to the one found on the bright blue *Morpho* butterfly [41] and the fabrication of an iridescent multilayer inspired by the cuticle of a woodboring beetle [42].

Chapter 1

Total internal reflection and light extraction

One important technological issue of the 21th Century will be to phase out incandescent and fluorescent light sources in order to replace them by highly efficient solid-state devices: light-emitting diodes, organic or inorganic. The electroluminescent mechanism at the heart of these devices encounters two limiting factors: (i) the internal conversion quantum yield, limited by the excitation of vibronic states and (ii) the light extraction, limited by the total reflection at the external surface of the active material. In modern light-emitting diodes, the internal quantum yield is very high [43, 44] due to the small energy of elemental vibronic excitations, representing losses not larger than a few percent. The problem of light extraction, i.e. external efficiencies, is much more stringent as backscattering losses can easily exceed more than 50%. The origin of the latter problem can actually be traced back to the total internal reflection occurring at the surface of a high refractive index active material in the direction of air. The present chapter will specifically discuss this problem. The first section describes in simple terms the total reflexion phenomenon and its incidence on the functioning of solid-state light sources. We will also review some of the engineering work that were developped to attempt increasing the external efficiency of light-emitting diodes.

1.1 Total internal reflexion

This chapter aims at properly explaining the problem of light extraction which has actually been the starting point of the present research. All the efforts developed for this investigation come from a quite well-known and geometrical optics issue: total internal reflection. The efficiency of lighting devices where the light source is embedded in a high refractive index material, is limited by this quite basic physical phenomenon. In this section, we will first examine Snell's laws and then consider the impact of these on the light extraction, using Fresnel's equations.

1.1.1 Snell's Laws

When light is traveling from a medium with high refractive index into a medium with a lower refractive index, the reflexion angle θ_r is equal to the incidence angle θ_i and the emergence angle θ_t is related to the incidence angle by Snell's law. Defining those angles from the normal to the surface and neglecting all absorption

$$\theta_i = \theta_r$$

$$n_i sin(\theta_i) = n_t sin(\theta_t)$$

n_i and n_t being the refractive indexes in the incidence and emergence media, respectively. If $n_i > n_t$, $\sin\theta_t$ can be predicted to be larger than 1, which means that `transmission` cannot take place. The reflexion is then total for incidence angles larger than a critical angle θ_{crit} defined by:

$$sin(\theta_{crit}) = \frac{n_t}{n_i} \tag{1.1}$$

Past this angle, no light can escape into the emergence medium. This, of course, limits drastically the intensity transferred to the emergence region and the efficiency of the internal emitting source.

More quantitatively, what fraction of the emitted light can we expect to cross the surface? Let's take the hypothetical case of a firefly. The firefly cuticle is mainly composed of chitin, which has a refractive index of n_{chit}=1.56 [45]. Though we will be more specific later, it can be assumed that internal tissues in the lantern have roughly the same refractive index. The emergent medium is air with a refractive index of n_{air}=1.0. From Equ.1.1 the resulting critical angle takes the value of 40°.

The value of the refraction index can be considered as moderate, as it is close to the refractive index of air, in comparison to the one for semiconductors which can easily reach up to $n_{semicond}$=4 or even higher. Light-emitting diodes (LED) for example use a variety of inorganic semiconductor materials such as Gallium Arsenide (GaAs), Aluminium Gallium Indium Phosphide (AlGaInP) or Gallium Nitride (GaN). These components have quite high refractive indexes such as n_{GaN}=2.5 and $n_{AlGaInP}$=4.2 at a wavelength of 425 nm. The critical angles are then even smaller, $\theta_{GaN} = 23°$ and $\theta_{AlGaInP} = 14°$. The light extraction is very limited. The case of the Gallium Nitride will be examined in chapter 6 when applied to a biomimetic approach for an actual GaN-based light-emitting diode.

1.1.2 Electromagnetic approach

From Fresnel Laws, the fraction of incident energy that is reflected and transmitted can be extracted. This approach will give us the light extraction efficiency (LEE) of the considered system.

Let's take a monochromatic incident wave with a pulsation ω_i and a wave vector $\overrightarrow{k}$ [46]:

$$\overrightarrow{E_i} = \overrightarrow{E_{0i}} \cos(\overrightarrow{k_i}.\overrightarrow{r} - \omega_i t)$$

In our case, $\overrightarrow{E_{0i}}$ is a real constant and the above equation represents linear polarized wave or plane wave.

The expressions for the reflected and transmitted waves are as follows:

$$\overrightarrow{E_r} = \overrightarrow{E_{0r}} \cos(\overrightarrow{k_r}.\overrightarrow{r} - \omega_r t + \varphi_r)$$

$$\overrightarrow{E_t} = \overrightarrow{E_{0t}} \cos(\overrightarrow{k_t}.\overrightarrow{r} - \omega_t t + \varphi_t)$$

ε represents the phase constants, which leads to a spatial and temporal origin that is not unique.

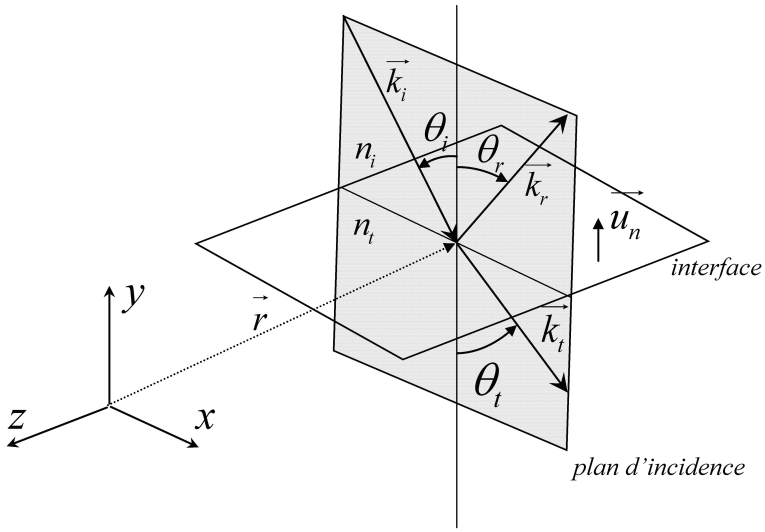

Figure 1.1: Description of the wave vectors of a plane wave arriving on the plane interface of two isotropic, homogeneous media.

Transverse Electric (TE)

$\overrightarrow{E}$ is perpendicular and $\overrightarrow{B}$ parallel to the plane of incidence (defined by x, y, see Fig. 1.1). The boundary conditions at the interface impose that the tangential components of the electric and magnetic fields at the interface are continuous for every time t and at every position x, y.

$$\overrightarrow{E_i} + \overrightarrow{E_r} = \overrightarrow{E_t}$$

$$E_{0i} + E_{0r} = E_{0t} \tag{1.2}$$

Fig. 1.2 shows the electric and magnetic fields and their respective directions. The electric fields $\overrightarrow{E_i}$, $\overrightarrow{E_r}$ and $\overrightarrow{E_t}$ are perpendicular to the plane of incidence and point all in the same direction. The tangential components of the magnetic field are continuous by a factor of μ^{-1}.

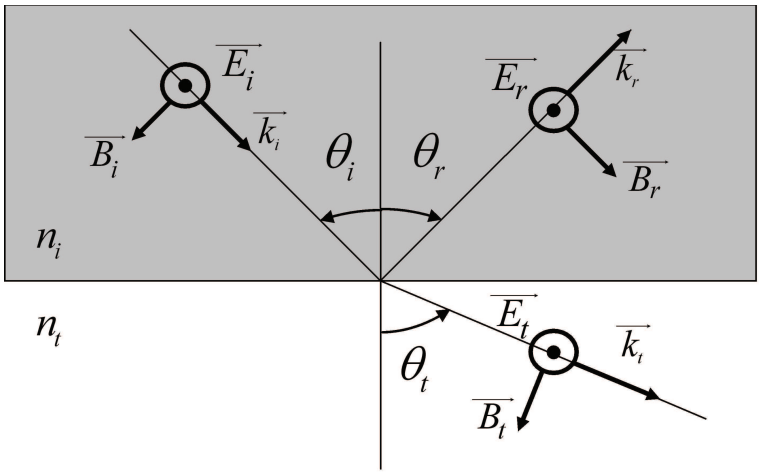

Figure 1.2: Boundary conditions at the interface. Directions of the electric and magnetic field in the transverse electric (TE) mode.

$$-\frac{B_i}{\mu_i}\cos\theta_i + \frac{B_r}{\mu_i}\cos\theta_r = -\frac{B_t}{\mu_t}\cos\theta_t$$

As $E = vB$, $\theta_i = \theta_r$ and $n = c/v$ the above equation can be simplified.

$$\frac{n_i}{\mu_i}(E_{0i} - E_{0r})\cos\theta_i = \frac{n_t}{\mu_t}E_{0t}\cos\theta_t \tag{1.3}$$

When combining Equ.1.2 and 1.3 and considering that the magnetic permeabilities are identical in the two considered regions, i.e. $\mu_i = \mu_t$, Fresnel's equations in the TE mode are obtained.

$$r_\perp = \left(\frac{E_{0r}}{E_{0i}}\right)_\perp = \frac{n_i\cos\theta_i - n_t\cos\theta_t}{n_i\cos\theta_i + n_t\cos\theta_t} \tag{1.4}$$

$$t_\perp = \left(\frac{E_{0t}}{E_{0i}}\right)_\perp = \frac{2n_i\cos\theta_i}{n_i\cos\theta_i + n_t\cos\theta_t} \tag{1.5}$$

Transverse Magnetic (TM)

In this case, $\overrightarrow{E}$ is parallel and $\overrightarrow{B}$ is perpendicular to the incidence plane. The boundary conditions are written as:

$$E_{0i}\cos\theta_i - E_{0r}\cos\theta_r = E_{0t}\cos\theta_t$$

$$\frac{B_{0i}}{\mu_i} + \frac{B_{0r}}{\mu_i} = \frac{B_{0t}}{\mu_t}$$

By the same procedure, we obtain the Fresnel equations in the TM mode.

$$r_{//} = \left(\frac{E_{0r}}{E_{0i}}\right)_{//} = \frac{n_t\cos\theta_i - n_i\cos\theta_t}{n_t\cos\theta_i + n_i\cos\theta_t} \tag{1.6}$$

$$t_{//} = \left(\frac{E_{0t}}{E_{0i}}\right)_{//} = \frac{2n_i \cos\theta_i}{n_t \cos\theta_i + n_i \cos\theta_t} \tag{1.7}$$

Equ.(1.4), (1.5), (1.6) and (1.7) can now be simplified by Snell's Law to obtain the following set of equations.

$$r_\perp = -\frac{\sin(\theta_i - \theta_t)}{\sin(\theta_i + \theta_t)} \tag{1.8}$$

$$r_{//} = \frac{\tan(\theta_i - \theta_t)}{\tan(\theta_i + \theta_t)} \tag{1.9}$$

$$t_\perp = \frac{2\sin\theta_t \cos\theta_i}{\sin(\theta_i + \theta_t)} \tag{1.10}$$

$$t_{//} = \frac{2\sin\theta_t \cos\theta_i}{\sin(\theta_i + \theta_t)\cos(\theta_i - \theta_t)} \tag{1.11}$$

For this first calculation, we will consider that the incident light has no preferential polarization. To simulate unpolarized light, we take the intensity average of the TE and TM mode.

1.1.3 Transmitted percentage through a plane surface

In order to identify the exact percentage of light that is transmitted through the interface and thereby escapes the incident medium, we need to calculate the ratio of incident and transmitted intensities. The Poynting vector $\overrightarrow{S}$ gives the direction of the energy-propagation of the wave and measures the energy flux transmitted by the wave.

$$\overrightarrow{S} = \overrightarrow{E} \times \overrightarrow{H}$$

The irradiance is the density of the radiant flux and it is calculated by taking the time-averaged value of the Poynting vector $\langle S \rangle$. Using the Maxwell-Faraday equation

$$\overrightarrow{\nabla} \times \overrightarrow{E} = -\frac{\partial \overrightarrow{B}}{\partial t}$$

the magnetic field $\overrightarrow{H} = \mu \overrightarrow{B}$ can be expressed as a function of the electric field $\overrightarrow{E}$. The wave-vector $\overrightarrow{k}$ is expressed as

$$\overrightarrow{k} = \frac{\omega}{c} n$$

The incident, reflected and transmitted irradiance become then respectively:

$$\begin{cases} I_i = \frac{v_i \varepsilon_i \varepsilon_0}{2} E_{0i}^2 \\ I_r = \frac{v_r \varepsilon_r \varepsilon_0}{2} E_{0r}^2 \\ I_t = \frac{v_t \varepsilon_t \varepsilon_0}{2} E_{0t}^2 \end{cases} \tag{1.12}$$

The reflectance is the ratio of the reflected power over the incident power. The power can be described as $IA\cos\theta$, where A is the encountered surface and I the irradiance.

$$R = \frac{I_r A \cos\theta_r}{I_i A \cos\theta_i}$$

Using Equ.(1.12) and Snell's Laws, the reflectance can be written as

$$R = \frac{I_r}{I_i} = \left(\frac{E_{0r}}{E_{0i}}\right)^2 = r^2 \tag{1.13}$$

The `transmissivity` is the ratio of the transmitted power over the incident power. Using $\mu_i = \mu_c$ and Snell's law it can be expressed as

$$T = \frac{I_t A \cos\theta_t}{I_i A \cos\theta_i} = \frac{n_t \cos\theta_t}{n_i \cos\theta_i}\left(\frac{E_{0t}}{E_{0i}}\right)^2 = \frac{n_t \cos\theta_t}{n_i \cos\theta_i} t^2 \tag{1.14}$$

By Equ.(1.13), (1.14) and the law of energy conservation, one can easily show that $R + T = 1$.

To calculate the transmissivity we can therefore use the following equation, established by Equ.(1.8), (1.9) and (1.13).

$$R = \frac{1}{2}\left(\left\{\frac{\sin(\theta_i - \theta_t)}{\sin(\theta_i + \theta_t)}\right\}^2 + \left\{\frac{\tan(\theta_i - \theta_t)}{\tan(\theta_i + \theta_t)}\right\}^2\right) \tag{1.15}$$

The transmissivity as a function of the incident polar angle (see Fig. 1.3) can be calculated knowing $T = 1 - R$ and Equ. 1.15. The light is very well extracted up to the critical angle determined earlier by Snell's laws, i.e. 40°. It then falls to an exact zero (black line on Fig. 1.3). However, one has to consider the three-dimensional nature of the problem. Even if the light extraction is very high at small angles, the encountered surface dS - defined by the solid angle $d\Omega$ (Fig. 1.4)- is small. The light extraction efficiency is therefore highly reduced in these small angle areas (red line on Fig. 1.3(a)) compared to more oblique directions, where the encountered surface is larger. The brown surface on Fig. 1.3(b) shows the `light extraction cone` defined by the critical angle. Light rays arriving with an incident polar angle θ, smaller than the critical angle, are refracted and can escape the incident material into free space (represented by the blue rays on Fig. 1.3 (b)). Light rays with a polar incidence higher than the critical angle are reflected and no light can escape from the incident medium (red lines) in these large angle regions.

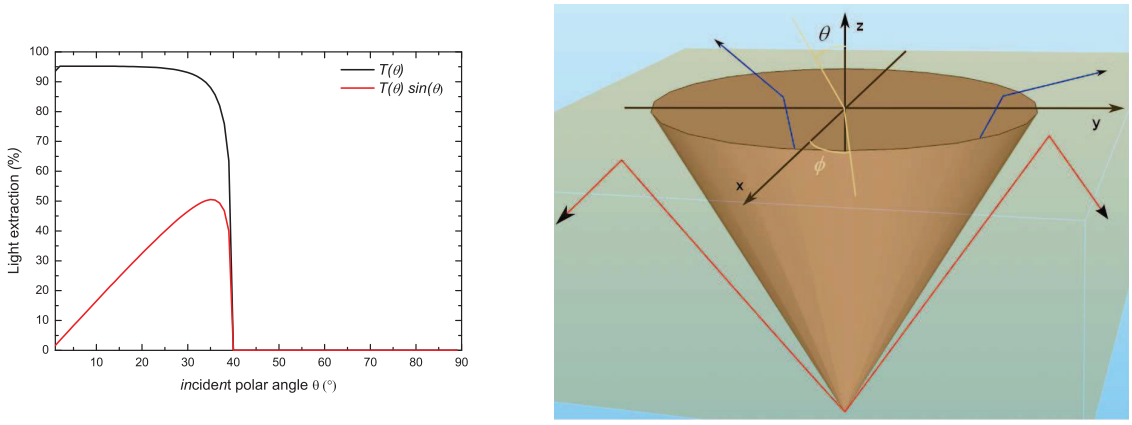

(a) (b)

Figure 1.3: (a) Light extraction for a plane surface as a function of the incident polar angle θ. The red line shows the influence of the surface perceived by the light rays. (b) The light extraction cone, represented by the brown surface, delimits the boundary between refracted (blue) and totally reflected (red) light rays.

In the case of a punctual source, the emitted intensity I_0 is uniform on the solid angle element $d\Omega$ of the sphere. This solid angle element arrives on the plane surface element dS (Fig. 1.4).

$$d\Omega = \frac{dS\cos\theta_i}{\rho^2} = \frac{dS\cos\theta_i\sin^2\theta_i}{r^2}$$

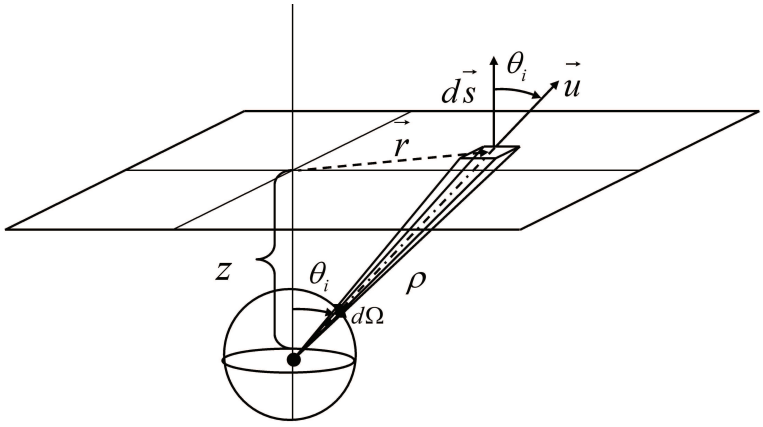

Figure 1.4: Light emission by a punctual source under a plane surface.

Let's now calculate the irradiance for all the solid angles of the upper hemisphere that are intercepting the material-air interface.

$$I_{inc} = \int_{2\pi} I_0 d\Omega = I_0 \int_{2\pi} \frac{\cos\theta_i\sin^2\theta_i}{r^2} dS$$

where $dS = rdrd\phi$

$$I_{inc} = I_0 \int_0^{\infty} \int_0^{2\pi} \frac{\cos\theta_i \sin^2\theta_i}{r^2} r dr d\varphi$$

By performing the substitution $\tan\theta_i = \frac{r}{z}$ the previous equation can be simplified.

$$I_{inc} = 2\pi I_0 \int_0^{\pi/2} \sin\theta_i d\theta_i$$

$$I_{inc} = 2\pi I_0$$

The transmitted intensity can then, by the same reasoning, be written as

$$I_{trans} = 2\pi I_0 \int_0^{\pi/2} T(\theta_i) \sin\theta_i d\theta_i$$

The ratio of the transmitted intensity over the incident intensity gives us then the transmitted percentage.

$$\frac{I_{trans}}{I_{inc}} = \int_0^{\theta_c} T(\theta_i) \sin\theta_i d\theta_i \tag{1.16}$$

As the transmissivity $T(\theta_i)$ falls to zero at angles above the incident critical angle the expression only needs to be integrated up to this critical angle θ_c.

1.1.4 Transmitted percentages

Let's consider as a first example the theoretical and hypothetical case of a bulk, chitin, homogeneous material as incident medium, ended by a plane interface to calculate the percentage of light transmitted through the interface, using Equ. 1.16. The emergent medium is air. Only about 20% of the light produced in a medium with refractive index of chitin can be extracted considering a plane chitin-air interface. This 20% value is effectively very low especially considering, that the refractive index is still quite moderate in comparison to the refractive indices of semiconductors. The light extraction is low (i) because of a the total reflexion which takes place after the critical angle $\theta_{crit} = 40°$. This phenomenon limits the light extraction significantly. (ii) The extraction of light from the dense material is high for angles below the critical angle. However, the intercepted durface dS is very small for small incident polar angles and the efficiency is therefore highly limited in small angle regions.

In the case of the a Gallium Nitride incident medium, we saw earlier, that the critical angle is reduced to 23° and therefore only 6% of the incident light can escape from the material. For an AlGaInP active material the critical angle is even smaller, which gives a value for the light extraction of only 2%. The efficiencies are very poor and lead to unacceptable energy losses.

These low extraction efficiencies which lead to large energy losses are mainly determined by the refractive indexes of the incident and emergent medium. The higher the contrast of refractive indexes, the lower the overall light extraction efficiency will be, due to a small escape cone for light. Considering these low extraction efficiencies, one can understand that even an increase in the light extraction efficiency (LEE) of some percents can be considered as significant and considerable. The idea that even a low increase can be considered as succes should be kept in mind during the reading of this manuscript.

The following section describes several recent publications that consider the light extraction enhancement of light-emitting devices by several different approaches.

1.2 Light extraction enhancement in current solid-state lighting

As we saw in the previous section there is a tremendous gap between the internal and the external efficiency of a light-emitting diode. Even if internal efficiencies of such solid-state lighting can reach up to 99.7% [47], the external efficiency is still very poor, due to the narrow escape cone in which exiting light is confined. This problem that occurs in solid-state lighting is well known and has already received considerable attention. Yablonovitch *et al.* announced already in 1993 an external quantum efficiency of 30% for a textured, thin-film LED [48]. For a GaAs LED, with a refractive index $n = 3.5$, only a mere two percent of the light created in the LED can be extracted into free space. By nanotexturing the thin-film surface using lithographic techniques, strong scattering can be achieved which leads to angle randomization. For a very high material quality and low parasitic losses this external quantum efficiency can even be enhanced up to 50%. Another technique used by Yablonovitch *et al.* to enhance the external efficiency (or light extraction efficiency LEE) consists in surrounding the edges of the light-emitting thin film with a 2D photonic crystal. This photonic crystal is meant to cause coherent scattering to extract the internally trapped light [49].

In order to avoid the high contrast between the refractive indexes of the material and air, several groups tried to enhance the light extraction by inserting an adaptive layer. Dylweicz *et al.* describe a graded-index antireflection layer formed by reactive ion etching and sparsely coated with a submonolayer of randomly placed silica spheres (diameter of 200nm) (Fig. 1.5(a-b)). They performed both, measurements and experimental analysis to quantify the resulting enhancement. With these random structures, theory announces an extraction efficiency enhancement of 22.31% (Fig. 1.5(c)), which corresponds to an increase of the apparent brightness of 1.63×. This value is even outreached by the measurement in an integrating sphere comparing the standard, commerical GaN blue LED and the structured LED, which gives an increase in apparent brightness of 2.2× [50]. The discrepancy between the simulated value and the measured value is explained by a graded refractive index effect in the actual sample, which has not been considered in the simulations, as these were focused on the escape cone increase. This technique shows already good results but is not easy to control and is not reproducible due to the random character of the structural parameters.

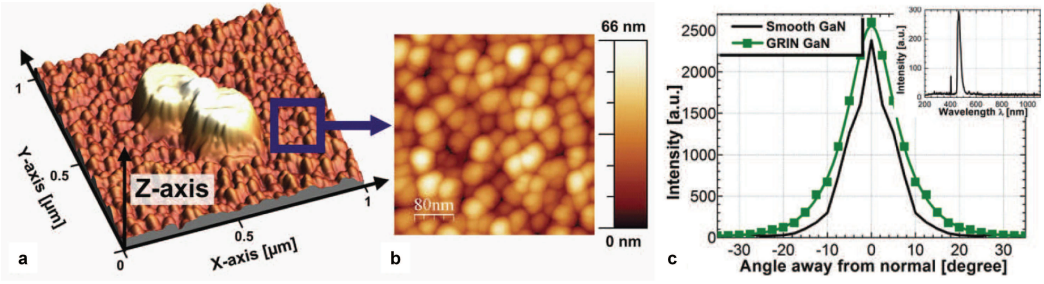

Figure 1.5: (a)AFM scan of the etched GaN surface showing GaN pillars in the middle. (b) A close up of the AFM scan. (c) ANgle-resolved photoluminescence spectra from the non-etched GaN wafer (black line) and the etched GaN wafer (green line). Both were excited by a 405 nm laser beam. The inset shows the photoluminescence and the pump laser light (smaller peak). (Credit: Dylewicz *et al.* [50])

The work of Hsu *et al.* [51] analyses four kinds of close-packed periodic structures with fixed structural parameters: nanorods, inverted nanorods, pyramids and inverted pyramids. The theoretical analysis shows that the inverted pyramid structure leads to a theoretical enhancement of 153% for a period of 350 nm and a height of 700 nm. These structures lead to diffraction in addition to the index-adapative layer. These examples are based on an anti-reflective index-adapting layer.

Soft holographic interference lithography can be used to create microlens-arrays on a glass substrate above an organic light-emitting diode to enhance the light extraction efficiency [52]. The diode is deposited on the ITO side of the glass and the microlens-array is patterned with a structure of 2 μm period and 1.2 μm height on the other side. A first measurement was realized for one diode covered by a 25×25 mm^2 microlens-array area. The light extraction from the glass slab is enhanced by 121%. For a LED array below a 5-fold larger microlens-array area, the light extraction is still enhanced up to 94%. Another group suggested to work with colloidal microlens arrays on III-Nitride LEDs: an InGaN LED is covered with large SiO_2 spheres ($\phi = 1$ μm) and smaller polystyrene (PS) spheres (ϕ=100 nm). The refractive indices are $n_{SiO_2} = 1.58$ and $n_{PS} = 1.46$ and thereby much lower than the refractive index of the active material. The spheres are deposited using rapid convection deposition (RCD). The tickness of the intermittent PS-layer, can be tuned with annealing (heating at 140°) from 0 to 810 nm. The total output powers for a current density of 80 A/cm^2 is 2.7 × higher for a PS-layer of 650 nm in comparison to planar LED. This enhancement is attributed to the scattered light extraction in large angular directions [53].

To improve the efficiency, LED are grown on Patterned Sapphire Substrate (PSS) which reduce the dislocation density by the lateral growth system [54]. Lee *et al.* combine, in addition to the PSS, an imprinted microstructure and a surface roughness to enhance the LEE. The pyramid microstructure was imprinted on the surface of the LED with a silicon mold, with a period of 5.16 μm and a heigth of 2.2 μm. To create an additional nano roughness, high-

density plasma was used on the imprinted microstructure. In comparison to a conventional LED, the LED processed on the PSS with a pyramid microstructure and the surface roughness achieves an overall enhancement of 85.9% [55]. Embedding a micrometrical air-structure on a PSS grown GaN-LED can as well increase the efficiency of the diode due to the decrease of the refractive index. Lysak *et al.* announce an increase of 54% for such an embedded 3D air-conical structure [56] (Fig 1.6). In this case a huge increase in efficiency is achieved by reducing the incident refractive index and thereby enlarging the light extraction cone.

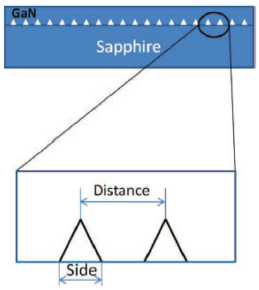

Figure 1.6: Embedded air prism in the active material. (Credit: Lysak *et al.* [56])

Photonic crystals are as well used for surface nano structuring in an attempt to enhance the light extraction of diodes. A triangular air hole array has been fabricated by focused ion beam (FIB) on a limited area of the GaN layer of a InGaN/GaN diode. The diameter of each hole is 150 nm and the depth is chosen to be either 50 nm or 200 nm (Fig 1.7(a)). Different lattice values were considered and the highest enhancement was measured for a 200 nm lattice . The peak illumination intensity was enhanced by 58% for a patterned ratio area of 21% ($60\times60\mu m^2$ patterned area for an illumination area of 170×100 μm^2), which has been confirmed by simulations. When the ratio is increased to 85% (60×60 μm^2 patterned area for an illumination area of 65×65 μm^2), the peak illumination intensity is even enhanced up to 91% [57] (Fig 1.7(b)).

A similar work has been conducted on a two-dimensional nano-cavity air-void photonic crystal [58]. The master template for the UV-curable nano-imprint process consists of a nano-pillar array with the following structural parameters: a diameter of 300 nm, a pitch of 600 nm and a heigth of 220 nm. Here the resulting patterned layer is glued to the light-emitting diode using a UV photo-initiator diluted with ethanol. This leads to an internal photonic crystal formed by air voids. The electroluminescent emission is thereby increased by 10%. Zuo *et al.* describe in their work the enhancement of light extraction efficiency by large-scale laser pattern on the surface of a GaN based blue light-emitting LED [59]. Elliptical stripes are engraved in the p-GaN layer of the LED by laser ablation, leaving alternatively ablated and non-ablated surfaces (width about 68μm) (see Fig 1.8 (a-b)). The ablated regions show high rugosity and offer the light more paths to be extracted from the active media (Fig1.8 (c)). The enhancement reaches 83.5%, but shows a high anglular dependence (Fig 1.8 (d)). When comparing the electroluminescent spectra for a patterned and a non-patterned LED as a function

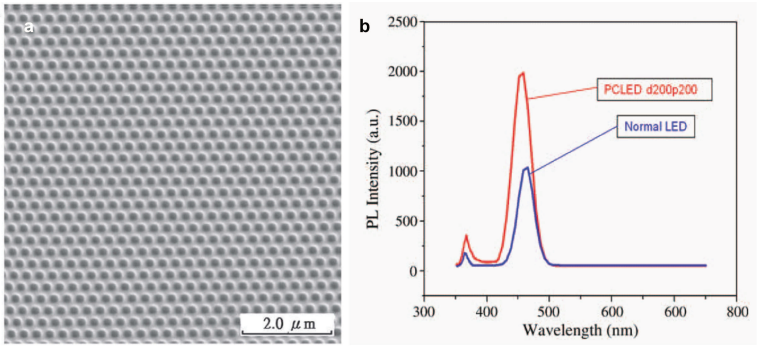

Figure 1.7: (a) SEM of the nano-structured photonic crystal fabricated on the nitride LED by FIB. (b) Photoluminescence spectra of the reference LED (blue line) and the nano-structured LED (red line). The extraction is increased by 91% for peak illumination. (Credit: Wu *et al.* [57])

of the emergent angle, two specific position for the detector show very high enhancement rates (50° and 150°). However, when considering the contribution from all angles, the light extraction efficiency is still enhanced by 34.9%.

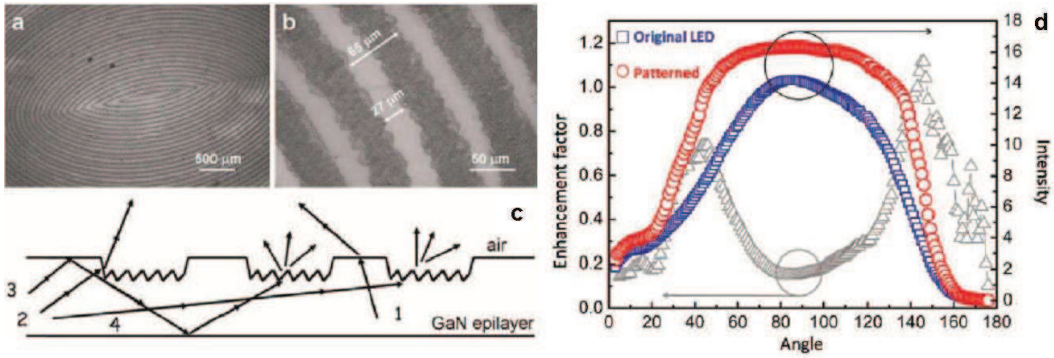

Figure 1.8: (a) and (b) SEM images of the GaN surface of the elliptical stripes engraved with laser patterning at different scales. (c) Light extraction paths taken by the light rays with the specific structure. (d) Spectrum of the electroluminescence of the unpatterned (blue squares) and unpatterned LED (red circles) as a function of the measurement angle. The light extraction is not uniform and presents a high angle dependence (grey triangles). (Credit Zuo *et al.* [59])

Embedding a metallic photonic crystal in a light-emitting diode could couple out light by two mechanisms (i) localized surface plasmons waveguide resonance and (ii) surface plasmon tunnel resonance. A square lattice of cylinder unit cells is embedded in the p-GaN layer and forms the metallic photonic crystal. Simulations show that the theoretical light extraction can be enhanced up to 4.6× [60].

These examples show that the problem of light extraction has raised a strong interest in the past few years. The problem has been addressed with several different approaches, like anti-reflective layers, micro- and nano-structuring. Significant improvements of external light

extraction efficiency have been announced. However, at the moment, it is difficult to exactly compare these results as different groups use different definitions of the light extraction efficiency. In addition, some of these papers describe only theoretical or only experimental results.

1.3 Light extraction efficiency and light extraction efficiency gain

In the present work we analyze first of all the problem from a theoretical standpoint. We then incorporate experimental results in order to consolidate the theory. The theoretical `light extraction efficiency` ζ is defined as the ratio of the light intensity extracted into free space I_{trans} over the light emitted in the active material I_{inc} (Equ.1.17). This leads to theoretical values which can be compared.

$$\zeta(\%) = \frac{I_{trans}}{I_{inc}}.100 \tag{1.17}$$

Another value, that will be considered is the `light extraction efficiency enhancement` $\Delta\zeta$ defined as follows from the structured device ζ_{struct} in comparison to the reference model ζ_{ref} :

$$\Delta\zeta(\%) = \frac{\zeta_{struct} - \zeta_{ref}}{\zeta_{ref}}.100 \tag{1.18}$$

In this chapter, the difficulty with light extraction has been explained. In the present work, we will adopt a biomimetic approach to find a way for light extraction improvement, i.e. first of all analyze the bioluminescent organ of a firefly. The next chapter focuses on bioluminescence in fireflies and gives an overview of its function and mechanisms.

Chapter 2

Bioluminescence in fireflies

Fireflies are found on all continents, except for the Antarctic. In Europe, three firefly species are known: *Lamprohiza splendidula*, the common glowworm *Lampyris noctiluca* and the lesser glowworm *Phosphaenus hemipterus* (all Lampyridae) [26]. The male of *Lamprohiza splendidula* is the only European flying and bioluminescent firefly. All European females are flightless, as well as the *Phosphaenus hemipterus* male. The male of *Lampyris noctiluca* does not possess any bioluminescent organs. These three examples of European firefly species show already a certain diversity. Bioluminescence has appeared several times during evolution. How and why exactly this property of living organisms appeared is not well known. This chapter gives an overview to the (possible) origin of the bioluminescence of fireflies and explains briefly how it is produced in the light-emitting organ of these insects. Finally, the light-emission wavelength of fireflies is briefly described and the spectra of two fireflies light emission is shown.

2.1 Why do fireflies emit light?

Fireflies are known for their ability to produce light. In several species, all the stages of development, from egg to adult, are bioluminescent. The firefly light organs undergo in that case radical changes. Larval light organs are only able to produce a continuous glow, whereas light-producing organs of adults of several species have the capacity to display complex flash patterns. Strause *et al.* described that the replacement of light-emitting organs in the different stages are accompanied by a neural reorganization [61]. Even the eggs and pupae of some fireflies species appear to be bioluminescent, showing a faint and continuous overall glow [62] (Fig. 2.1(a-c)). The function fulfilled by luminescence of Coleoptera larvae is not understood. Suggestions include startle warning, camouflage and luring of prey [63]. De Cock and Matthysen provide evidence for `aposematism` signalling of bioluminescence from glow-worm larvae [64]. The emitted light is used as a warning signal, similar to a color pattern for diurnal organisms [65]. Many lampyrid species are distasteful and even toxic [66,67] for a variety of generalist predators, such as arthropods, birds, amphibians reptiles and fishes. Knight *et al.* reported that the ingestion of *Photinus* fireflies can even be fatal to Australian bearded dragons (*Pogona* sp.) [68]. These observations can reinforce the aposematism hypothesis [69].

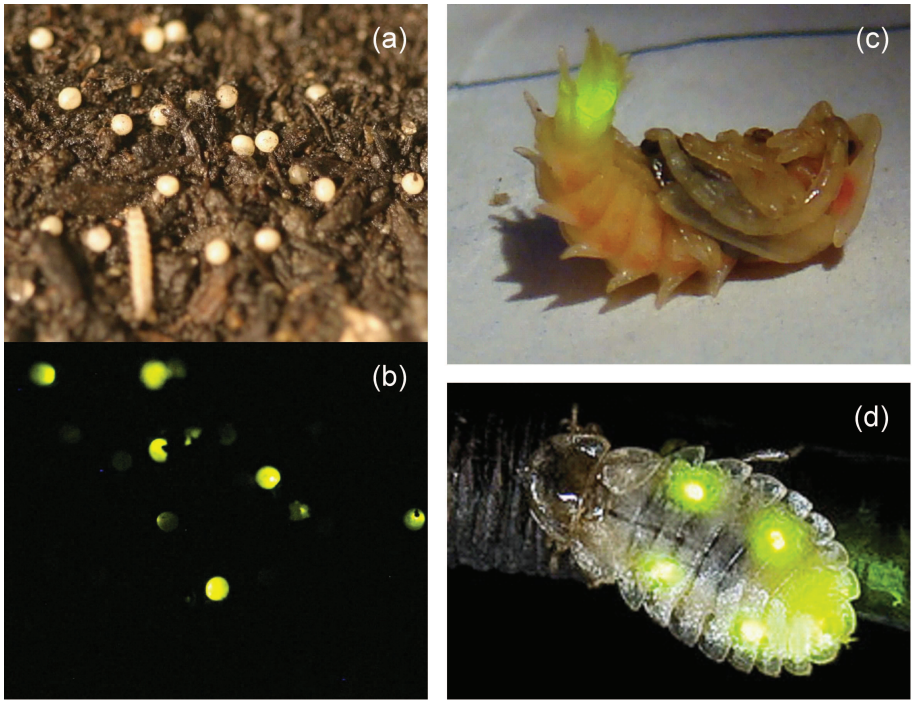

Figure 2.1: Different stages of the firefly development that display bioluminescence. (a) Eggs under artificial illumination. (b) Eggs emitting bioluminescence. (c) Pupa *Lucidota atra*. (d) *Lamprohiza splendidula* female.

In adult fireflies, the bioluminescence is used for courtship. Lloyd describes three biological groups within the Lampyridae family [70]: (i) In the "fireflies" group, the males emit precise flashing patterns to attract the attention of the females, such as *Photuris*, *Photinus* and *Pyractomena*. (ii) In the "glow worms" group, the females are bioluminescent and `brachypterous`, `apterous` or larviform (Fig. 2.1(d)). They emit light to attract the attention of the males. These are `macropterous`, using their wings to search aerally for their females, but do not emit light in most cases. Their big and sensitive eyes help them to locate the females. Genera in this group include *Pausis*, *Microphotus* and *Pleotomus*. (iii) The last group is called "daytime dark fireflies" and do not use bioluminescence for communication, as they are diurnally active.

The firefly studied in our case (*Photuris* sp.) belongs to the first biological group. The males are emitting light flashes to attract the attention of their females and these sit in the grass waiting and responding to the specific light pattern[1]. In this case, when both, males and females, are bioluminescent, complex flash patterns can be used to communicate and localize the partner. Figure 2.2 gives an example and shows the male-female dialogs of three different *Photinus*

[1] As observed during collection, see Materials and Methods.

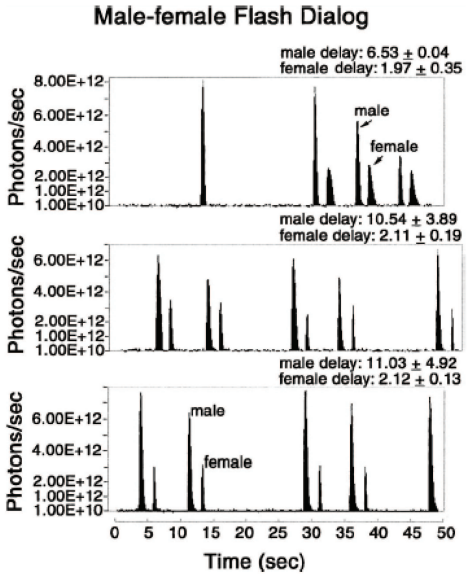

Figure 2.2: Male-female dialogs of *Photinus pyralis* measured by an integrating sphere in an flight emulation setup described by Case *et. al* (Credit: Case *et. al* [71])

pyralis pairs [71]. In the *Photuris* genus, Lloyd described cases of aggressive `mimicry`, where the macropterous females mimic the flash-responses of *Photinus* females to attract *Photinus* males and devour them [72] (Fig. 2.3). The *Photuris* female ingests in this way the toxic components of the *Photinus* male, which provides a protection against its predators [73].

Figure 2.3: *Photuris* firefly "femme fatale" feeding on a male *Photinus* prey. (Credit: J. E. Lloyd. With the permission of the author.)

2.2 How does bioluminescence work?

Bioluminescence originates from an enzyme-catalyzed chemical reaction. It is often described as the oxidation of the substrate luciferin catalyzed by the enzyme luciferase, but this is an oversimplified statement for a quite complex chemical reaction. In reality, the chemical reaction derives from more fundamental metabolic mechanisms in agreement with the evolution theory. Firefly luciferin reacts with adenosine-triphosphate (ATP) which generates luciferyl-adenylate. Oxyluciferin, CO_2 and adenosine-monophosphate are then produced by the oxidation of the luciferyl-adenylate in the presence of molecular oxygen. This photon-emitting reaction taking place at room temperature needs to be very exergonic, as one photon of green light (around 500 nm) corresponds to about eight time the energy released by the hydrolysis of adenosine triphosphate (ATP) into adenosine diphosphate (ADP), i.e. about 60 kcal/mole [74].

Figure 2.4 shows the steps involved in the luciferin-luciferase reaction. The luciferin forms a `ternary complex` with the ATP and the luciferase. Luciferyl adenylate (carboxilyc group of luciferin and AMP) is formed and pyrophosphate (PPi) released (Fig. 2.4(a)). Pyropohosphate ($P_20_7{}^{4-}$) is formed by the hydrolysis of adenosine triphosphate (ATP) into adenosine monophosphate (AMP) in cells. This adenylate is then oxidized into firefly dioxetanone, a cyclic peroxide (Fig. 2.4(b-d)). Oxyluciferin in a singlet electronically excited state is formed after the `decarboxylation` of dioxetanone (Fig. 2.4(e)). This electronically excited oxyluciferin decays rapidly to its ground state releasing a photon (Fig. 2.4(f)). The luciferin in fireflies (and beetles) is the same, but the light displayed can range in color from green (λ_{max}=530nm) to red (λ_{max}=635nm) [75]. Several factors can determine the color of bioluminescent emission in fireflies, including the amino acid sequence of the luciferase and the polarity of the micro environment [76].

The oxygen-consuming bioluminescent substrate is described as a potential antioxidant,which could be a possible pre-bioluminescent function in the evolution of bioluminescence [77]. Numerous different luciferin-luciferase reactions have been determined from several and phylogenetically diverse organisms, which indicates that bioluminescence has evolved independently several times [75].

A study conducted on the luciferin contents in luminous and non-luminous beetles showed that the *Photinus pyralis* firefly contains on the average 2.1 nmol of luciferin in its `lantern` and *Photuris pennsylvanica* even up to 100 nmol in its adult stage [78].

The quantum yield[2] of the bioluminescent reaction of firefly luciferin and luciferase was described in 1960 to be 0.88 [79]. A more recent study by Niwa *et al.* showed that the quantum yields of the luciferase (at a pH 8.0) from three different firefly species are 0.48 for *Photinus pyralis* and 0.43 for *Luciola cruciata* and *Luciola mingrecila* [80].

Another interesting fact worth to note is that the firefly flashing increases the metabolic rates only by 37% above resting values, while in comparison, firefly walking increases the metabolic rates by 57% [81].

[2]The quantum yield (QY) is defined as the efficiency of the production of photons from a single reactant molecule.

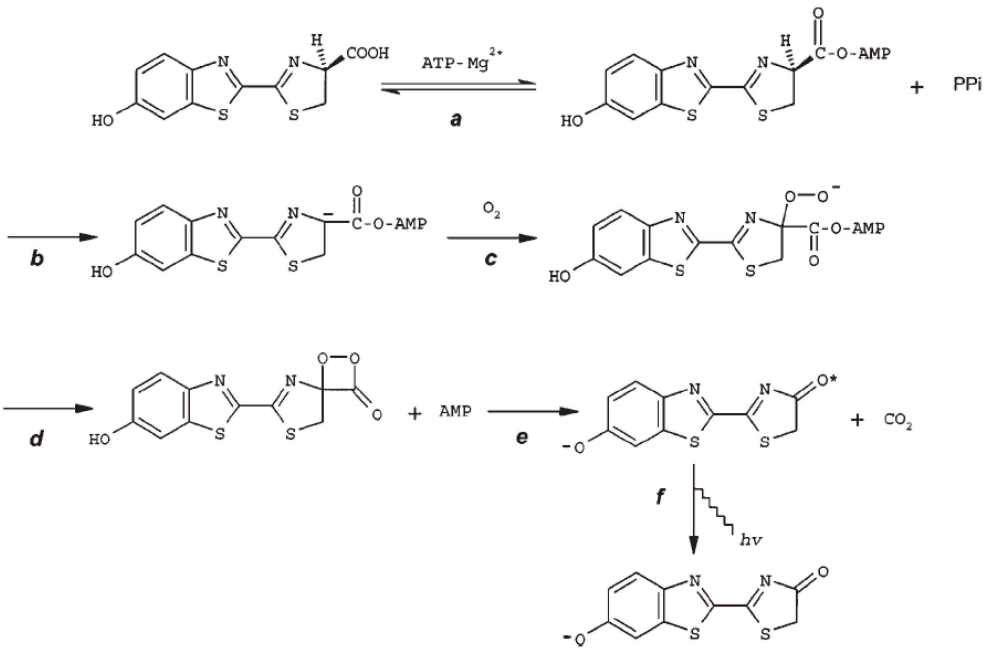

Figure 2.4: Steps of the bioluminescence reaction. (Credit: Day *et al.* [75])

2.3 Emission wavelength

The emission of two fireflies species were measured in order to determine the wavelength of the emitted light. The measurements were carried out with an *Avaspec 2048 Avantes* spectrometer. The aim of this measurement was to determine the spectral position of the emission peak of the firefly luciferin. Two species could be kept alive in the laboratory to perform the measurements: the European firefly *Lamprohiza splendidula* and *Aspisoma ignitum* from the Lesser Antilles[3]. The graph in Fig. 2.5 shows the emission spectra. The peak wavelength for *Lamprohiza splendidula* is 554 nm with a full width at half maximum (FWHM) of 58 nm. This narrow emission peak corresponds to a yellowish green emitted light, which could be observed during the measurement. For *Aspisoma ignitum* the peak wavelength is a little bit larger at 565 nm with a FWHM of 52 nm. This wavelength corresponds to a more yellow-green color.

Seliger and McElroy studied the light emission of several firefly species including one in the *Photuris* genus and several in the *Photinus* genus. The peak wavelength of the emitted light reaches from 552 nm to 575 nm [79]. The genus of the species studied in this work has been determined as *Photuris* sp. The species is not known. For simulations, we will therefore consider an average value taken from the above described wavelengths.

[3]More information about the collecting and taxonomic determination of these fireflies can be found in the Materials and Methods section.

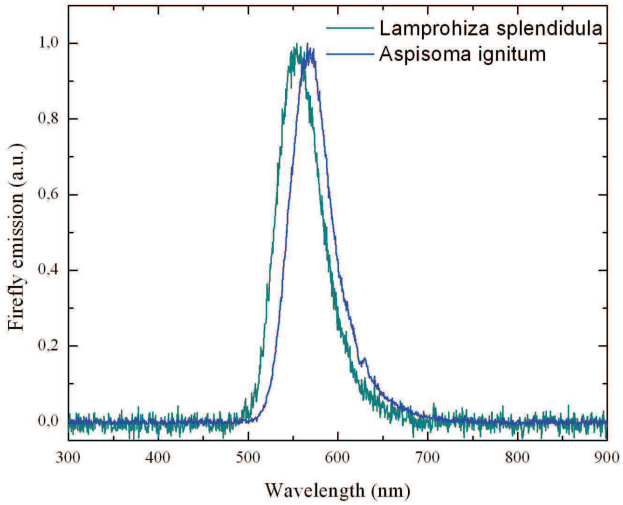

Figure 2.5: Firefly emission of two firefly species kept alive in the laboratory: *Lamprohiza splendidula* (green line) and *Aspisoma ignitum* (blue line).

Chapter 3

Morphological investigation of the bioluminescent organ of fireflies

A thorough study of the bioluminescent organ of the *Photuris* firefly, started as a Master thesis, showed several interesting structures [82]. In this chapter we detail these substructures and complete the previous data by a nanotomographic analysis. Moreover the impact of each structure on the light extraction is briefly described.

Figure 3.1 shows the European firefly *Lamprohiza splendidula*, collected in Belgium. The bioluminescent organ is located on the ventral side at the tip of the abdomen. In the studied macropterous adult male firefly species, the bioluminescent organs are located under the 5th and 6th segments.

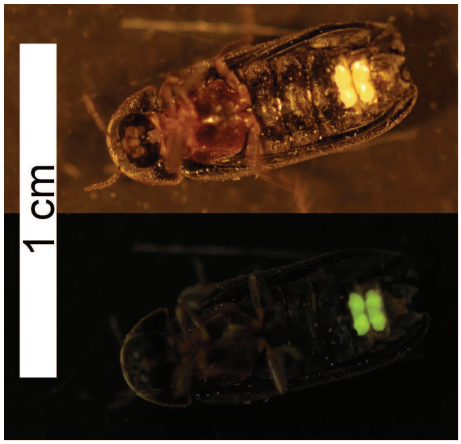

Figure 3.1: European firefly *Lamprohiza splendidula* under artificial illumination (above) and emitting bioluminescence in the dark (below). The bioluminescent organ is located on the ventral side, at the end of the abdomen and can be clearly distinguished in both images. In darkness the location of the organ is obvious (green light emission) and under artificial illumination it can be easily defined as the two non-pigmented, whitish segments.

3.1 Scanning electron microscopy

A first investigation has been carried out with two scanning electron microscopes (SEM): a Phillips XL20 SEM and the higher resolution field-emission SEM JEOL 7500F. Electron microscopy is an appropriate observation technique, as we expect to have structures of the size of the wavelength or several times the wavelength, i.e. 560 nm. The resolution accessible by the SEM JEOL 7500F is about 1 nm under ideal observation conditions. Details about the sample preparation and observation condition are explained in the Material and Methods Chapter at the end of this manuscript.

3.1.1 *Photuris* sp.

The first investigated species is a *Photuris* sp. firefly, collected in Panama in 2009[1]. Figure 3.2 shows the longitudinal cut through one of the bioluminescent segments.

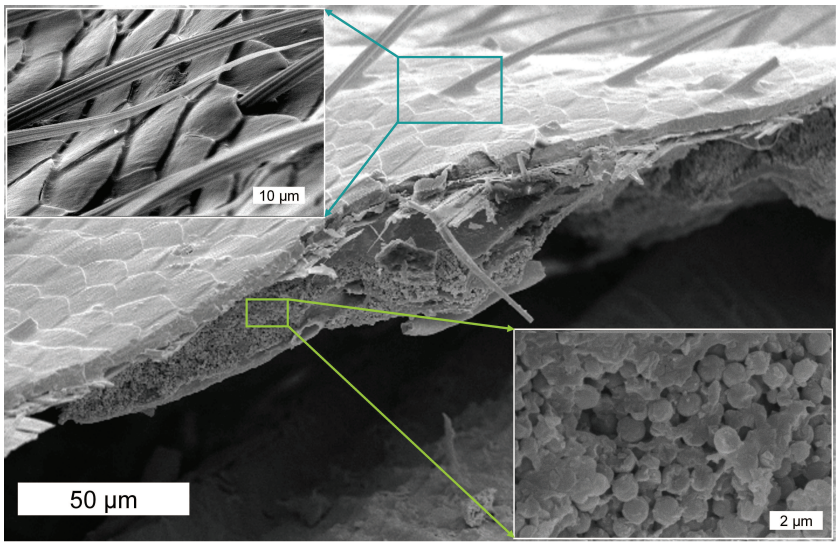

Figure 3.2: SEM pictures of the firefly abdomen: bioluminescent segment. The cuticle of the firefly is structured by protruding scales. The bioluminescent organ, just below the cuticle, is filled with peroxisomes.

The bioluminescent organ is located below the firefly cuticle. This bioluminescent organ, also called `lantern`, is composed of several big cells called `photocytes` [83]. The lower inset shows a small, magnified area inside one of these photocytes, where spheres of 1 μm of diameter can be seen. These spheres have been identified as `peroxisomes` [84,85]. These peroxisomes are mainly composed of urate, which has a lower refractive index than chitin(n_{urate}=1.4). It is not unusual to find peroxisomes in cells as metabolic waste is stored there, but not in such a huge amount [86]. Smalley *et al.* investigated the origin of the bioluminescence inside the cell of a *Photuris* firefly

[1]For more details about the collection of these specimens, as well as the sample preparation, please refer to the Materials and Methods Chapter at the end of this manuscript.

by fluorescence [87]. They emitted the hypothesis that the bioluminescent reaction takes place in these peroxisomes. The arrangement of the spheres looks disorganized in the SEM pictures, but SEM does not allow to conclude immediately on a disordered arrangement.

The upper inset shows the outer structure of the cuticle. This cuticle is not flat, but presents a specific structure: scales are found on the cuticle. These scales are neither matching to form a flat surface, as in other Coleoptera, nor overlapping as observed in many other insects such as butterflies. The scales are slanted so that they form a series of steps, due to a pronounced misfit. This specific arrangement of the scales leads to a complete new geometry of the chitin-air interface, which will influence the light propagation. One can view these scales as small two-dimensional prisms aligned next to each other with their protruding end oriented in the direction of the abdominal tip. These prisms occur with a main period of about 10 μm and the protruding end reaches around 3 μm. This pattern will be referred to as jagged scales in the following.

Figure 3.2 shows `setae` on the cuticle of the abdomen. These setae could work as guides to extract the light, but their small density implies that the thereby augmented efficiency would not be sufficient. Moreover it seems more likely that these setae have another function, such as sensing. A short-scale corrugation has as well been found on the outer surface of each individual scales (Fig. 3.3). Its profile is approximately sinusoidal, with a period of 250 nm and a height of 100 nm.

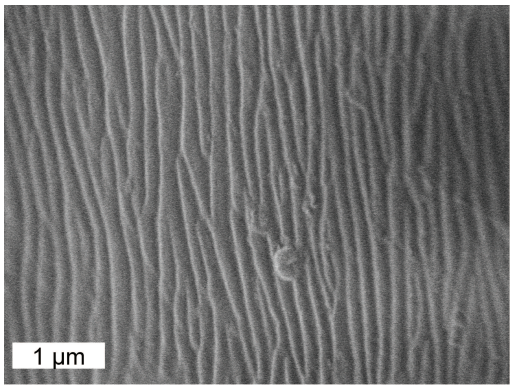

Figure 3.3: SEM pictures of the cuticle of the bioluminescent segments. In addition to the long-scale structure, a structure with a smaller periodicity appears.

The bulk of the cuticle is not homogeneous, but constituted of a multilayer stack. One bilayer is composed of one plain chitin layer and one layer where the chitin forms a similar sinusoid as found on the cuticle and described earlier (Fig. 3.4). This sinusoid leads to spacing in the layer. The whole multilayer has a thickness of 2.4 μm and contains about 30 bilayers of 80 nm each. The plain chitin layer has a height of 30 nm and the structured layer with a sinusoidal profile is characterized by a height of 50 nm and a period of 250 nm.

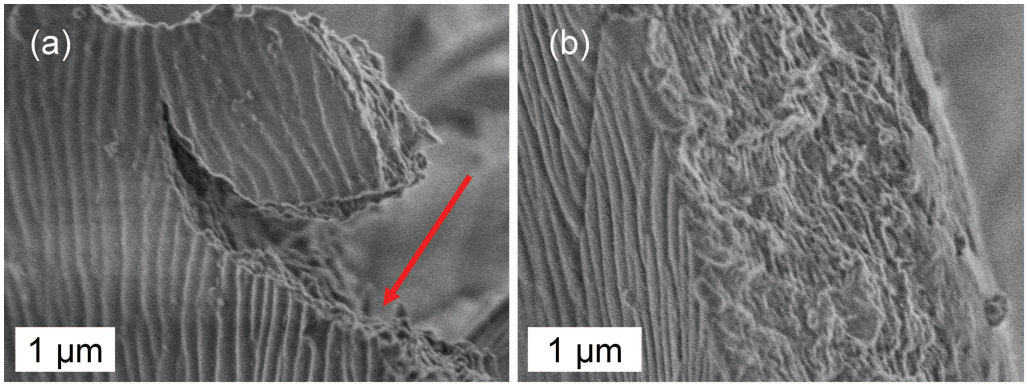

Figure 3.4: SEM pictures of the firefly exoskeleton. (a) The outer small scale structure is visible and at the broken parts, one can see that the exoskeleton is not plain. (b) A multilayer structures of the bulk of the exoskeleton.

Figure 3.5 shows a larger view of the exoskeleton section. The external surface can be seen in the upper part of the image (blue arrow). The multilayer which makes the bulk of the tegument in the abdominal part is located below (red arrow). Between the multilayer and the cellular wall of the bioluminescent organ (right lower corner of Fig. 3.5) fibers are found (purple arrow). The cellular wall of the bioluminescent organ has a thickness of 60 nm approximatively. These fibers could be muscular fibers. It is not unusual to find muscles in proximity of the cuticle, as the cuticle is not a rigid and fixed organ. These muscles could help to scatter the reactant liquids in the bioluminescent organ quickly enough to produce the observed flashes. These assumptions were formulated during a discussion with the marine biologist Laure Bonnaud of the "Université de Paris Diderot" (Paris 7) [88]. At another conference, a discussion with Dr. Dimitri Deheyn, marine biologist at the Scripps Institution for Oceanography (UCSD, USA) gave additional informations [89]: the fireflies bend their abdomen during the flash which obviously needs strong muscles.

3.1.2 *Aspisoma ignitum*

A similar investigation was conducted on the firefly collected in the Lesser Antilles. The SEM analysis of the cuticle of *Aspisoma* does not show any particular long-scale structure. However, the interior of the bioluminescent organ is different from the one found in *Photuris* (Fig. 3.6). This firefly has been collected in Guadeloupe, an island in the Carribean Sea 600 km apart from the closest continent. This specific localization of this firefly species could give important information about the evolution of the bioluminescent organ. This species evolved completely cut off from the specimens on the continent. Fireflies from the *Aspisoma* genus are much larger and survive much longer in captivity than fireflies from the genus *Photuris*. It would be interesting to conduct a determination of the genome of these fireflies species to study the phylogenetic connection. We should note already here, that this difference in the cuticle and the bioluminescent organ could give an important indication about the necessity of specific light extracting structures. The specific arrangement of the *Aspisoma* lantern could already give an increase in

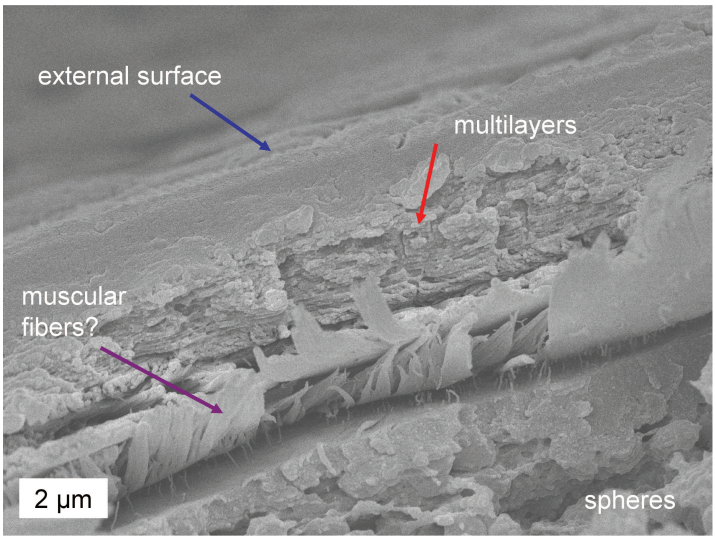

Figure 3.5: SEM pictures of the cuticle volume of the bioluminescent segments. The cuticle volume has several structures: outer small scale structure, multilayer and muscular layer.

the light extraction efficiency and no additional structures would be necessary[2].

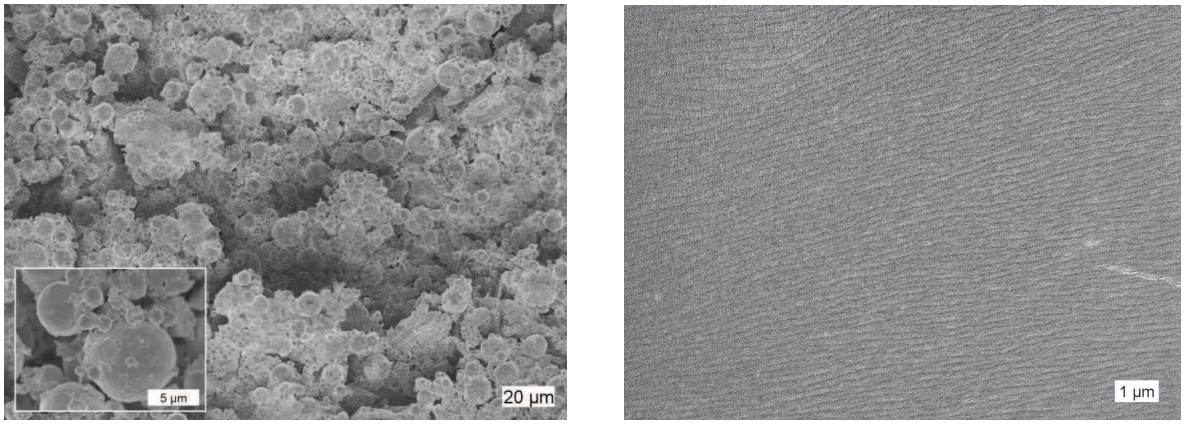

(a) (b)

Figure 3.6: The bioluminescent organ of *Aspisoma ignitum*. (a) Interior of the lantern showing spheres with a polydisperse distribution of the diameter size. (b) Cuticle surface above the lantern. The corrugation found on the cuticle is similar to the small-scale structure found on the *Photuris* firefly. No scales appear on this cuticle.

3.1.3 *Lamprohiza splendidula*

The European firefly shows neither the large scale structure nor the small scale corrugation. The bioluminescent organ is filled with spheres in the same way as in the *Photuris* case. The

[2]This assumption seems reasonable, but has not been studied yet

European firefly seems to be less evolved compared to both *Photuris* or *Aspisoma*. The observation of these fireflies during their active period shows that the light is emitted continuously; the other investigated species show a flashing behavior to communicate. This can give an indication that the European firefly has a smaller complexity level of its bioluminescent lantern, as described by Buck [90] and could therefore be in a former state of evolution.

3.2 Optical Microscopy

In order to check the transmission through the cuticle, we put a small part of the abdomen of the *Photuris* firefly under the microscope and illuminated it with the microscope source located below the cuticle. To ease the illumination from below, we spent time eliminating as much as possible the remaining interior of the firefly. We did not remove all the organic material and left the photocytes just below the cuticle. However at one spot this organic material was cracked and it appeared that we could observe only the transmission through the cuticle. The highly illuminated line on Fig. 3.7 shows the crack in the organic material, where light only passes the cuticle with the jagged-scales structure. The light extraction on the protruding edges of the scales (perpendicular to the cracked zone) appear to be much higher than in the rest of the cuticle. The inset shows the profile of the illumination on one of the protruding edges. One can see a high increase in intensity around this edge. This image from an optical microscope leads to the assumption that the protruding edges can enhance the overall light extraction of the firefly.

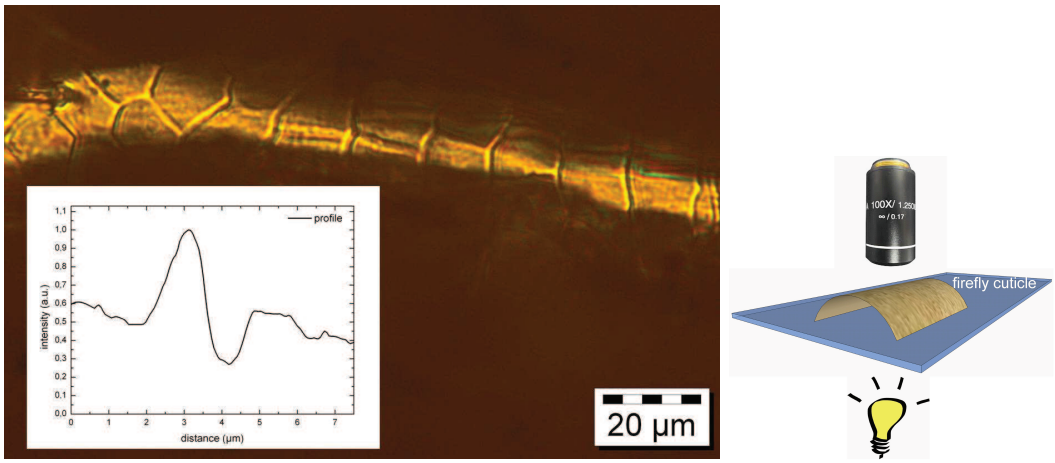

(a) (b)

Figure 3.7: (a) Optical microscopy of the cuticle: transmission mode. The light source is located below the sample and the microscopy image is taken from the upper, tilted-scale side. The enlightened region shows the light transmission through the cuticle only. The jagged-scales show an increased light extraction at the sharp edges. (b) Schematic representation of the observation conditions.

3.3 Hard X-ray nanotomography

A particular question could not be answered with the scanning electron microscope: How are the spheres distributed in the bioluminescent organ? This question is important as a specific arrangement of the spheres could direct the emitted light in one particular direction, which could be useful for the extraction enhancement. The disadvantage of the electron microscope is that to observe the inner organ, we have to cut the insect abdomen. By doing this, the interesting structures could be displaced or even damaged. To avoid this effect we went to the European Synchrotron Radiation Facility (ESRF) in Grenoble (France) to perform hard X-ray nanotomography on the lantern of the fireflies. This technique does not require any intervention and the whole bioluminescent organ can be analyzed. Different samples of *Photuris* and *Aspisoma* were prepared. The details of the sample preparation can be found in the Material and Methods Chapter at the end of the manuscript.

3.3.1 *Photuris* sp.

Figure 3.8(a) shows a slice of the reconstructed three-dimensional data obtained at the ESRF. One can clearly see the peroxisomes distributed in the bioluminescent organ. The white areas represent empty spaces and correspond to the `tracheoles`, a fine respiratory tube, of the firefly.

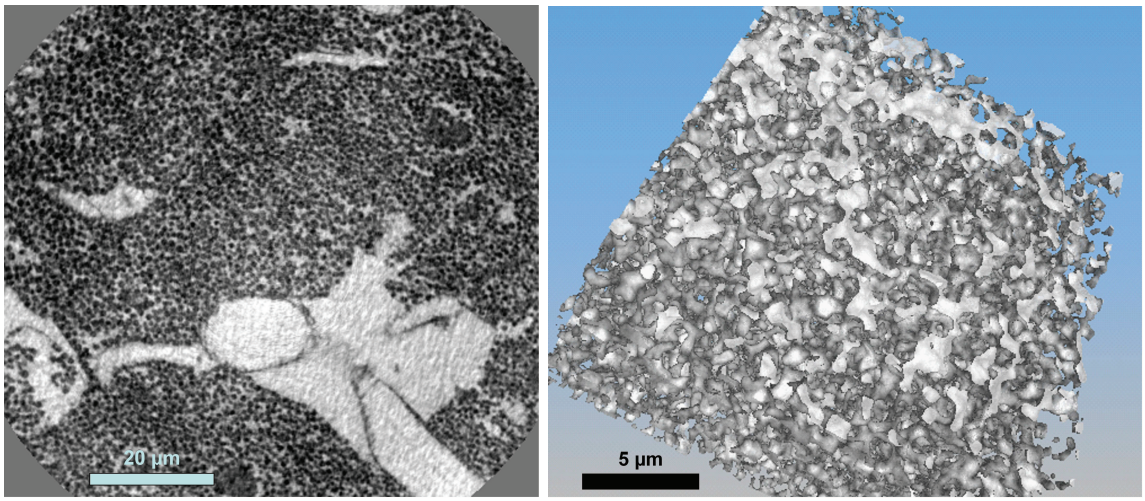

(a) 2D View. Slice of X-ray nanotomography data. (b) 3D View. Detail of the slice.

Figure 3.8: *Photuris* sp. X-ray nanotomography data from the bioluminescent organ of the firefly. The peroxisomes does not have a particular arrangement and appear completely disordered.

The three-dimensional representation (see Fig 3.8(b)) confirms, that the spheres are arranged in a complete random way.

3.3.2 *Aspisoma ignitum*

Figure 3.9 shows slices of the reconstructed data obtained at the ESRF from the *Aspisoma* firefly. One particular difference can be immediately seen. The bioluminescent cells are way

more defined and smaller as in *Photuris*. The bioluminescent organ is composed of several large cells: the photocytes. In the lantern of *Photuris*, these photocytes were not easily distinguished as the lantern appears more as one big photogenic cell. In *Aspisoma*, we could observe small irregular spheres under the microscope. During the analysis of the X-ray tomography data, we could define these spheres as the photocytes (see Fig. 3.9(a)). The photocytes can be seen in the upper left corner of Fig. 3.9(a). When taking a look into the interior of the photocytes (inset of Fig. 3.9(a)), one can again distinguish a granular environment. Figure 3.9(b) shows a close up of the photocytes. Contrasting the former sample, this one consists of two photocytes which were glued immediately to the sample holder under the optical microscope. One can see the cellular wall of each photocyte in the middle of the image (enhanced in red on the left photocyte). The data obtained by nanotomography confirms the observation with SEM, the distribution in sphere diameter is polydisperse with a smaller and a larger diameter. The smaller spheres have the same dimension as the peroxisomes described in the *Photuris* firefly. By contrast, the exact function of the larger size spheres has not been determined yet. It would be interesting to understand the purpose of these large diameter spheres in the lantern of *Aspisoma*.

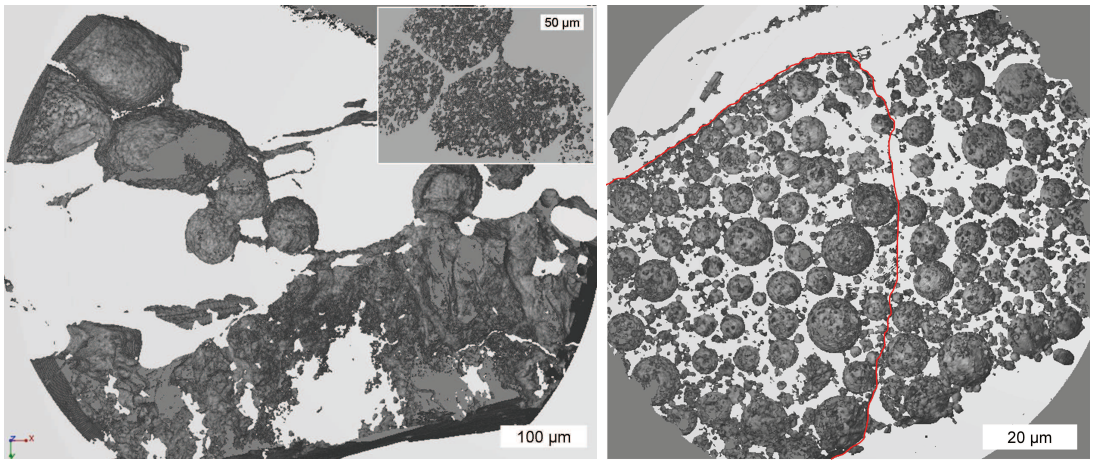

(a) 2D View. Overview of the photocytes. (b) 2D View. Inside of the photocytes

Figure 3.9: *Aspisoma ignitum*. X-ray nanotomography data from the bioluminescent organ of the firefly. The lantern of this species of fireflies is different from the *Photuris* lantern. The peroxisome-diameter size is monodisperse in the *Photuris* lantern and polydisperse in the *Aspisoma* lantern with two average diameter sizes.

The conclusion which can be taken from the data obtained by hard X-ray nanotomography at the ESRF, is that the sphere are arranged in a completely random way. This information is as well reinforced, as we have a dispersion in the diameter size of the peroxisomes, monodisperse for *Photuris* and *polydisperse* for *Aspisoma*. The knowledge about the spheres arrangement is important, as it indicates how we can modelize in the most correct way the light propagation through the insects abdomen. The randomness in the spheres size and distribution indicates that random scattering is taking place in the bioluminescent organ. The light rays are scattered in all directions. The refractive indexes of the lantern are probably smaller than the one of

pure chitin: the peroxisomes are composed mainly of urate and the voids between the spheres are probably filled with liquids carrying the reactants necessary for the bioluminescence. In the simulations, described in the following chapter, we will therefore make the hypothesis of an isotropic homogeneous incident material.

3.4 Comment on the substructures found on *Photuris* and *Aspisoma*

The morphology of the outer cuticle and the lantern in *Aspisoma* is different than in the *Photuris* firefly. Regarding the phylogenetic relationships between these two species[3], they are included in two different subfamilies: Lampyrinae and Photurinae respectively. The throughout analysis of the the lantern morphology of these phylogenetically different species, can give indications about potential interesting structures for light extraction increase. One notable difference lays in the geometry of the cuticle surface: the *Aspisoma* firefly has only the small scale corrugation on the outer surface, whereas the *Photuris* firefly has a large tilted-scale structure on the outer surface.

In this work we will limit our theoretical analysis to the structures in and on the cuticle. The interior of the lantern with its disorganized arrangement of the spheres will be treated as a homogeneous medium with an average refractive index. Different reasons motivate this decision: (i) The difference of refractive index between the spheres (urate) and the interstitial fluid is weak (of the order of 0.1) so that the interface will not generate any appreciable scattering. (ii) The randomness of the spheres location implies an isotropic response, excluding any oriented diffraction effect. (iii) The main goal of this work is to find a device, or layer, to increase the light extraction efficiency of existing LED's. We do not have in mind to rethink the fabrication process of the active material of diodes. The mean refractive index of the homogenized lantern is lower than the value of chitin, which will as well increase the light extraction efficiency, due to an enlargement of the extraction cone (see chapter 1). However, in the case of the LED, we can not decrease the refractive index of the active material easily, as we are bound to the composition of the semiconductors available on the market. (iv) The modelization of an incident medium with a complete random arrangement of spheres with different sizes is a quite difficult undertaking. Several algorithms have been developed to address this problem (such as the "Multiple sphere T-matrix" algorithm [91]), but none of them fits the requirements of the given problem, i.e. large scale scatterers - in comparison to the wavelength - and with a large random distribution (up to several mm).

3.5 Summary

The morphology of three different species of fireflies was investigated. *Aspisoma* and *Lamprohiza* are included in the Lampyrinae subfamily, whereas *Photuris* is included in the Photurinae

[3]See Materials and Methods

subfamily. *Photuris* sp. was the only analyzed species that showed the jagged scales morphology. It was important for our work to analyze other species of fireflies, to be able to compare potentially interesting structures. The Carribean *Aspisoma*, the European *Lamprohiza*, another unidentified firefly collected in Costa Rica and others, provided by the Royal Museum for Central Africa do not have the micrometric jagged-scales structure on their cuticle. The bioluminescent organ of the Carribean firefly is more complex, than that found on *Photuris*. The arrangement of the inner lantern alone could enhance the light extraction sufficiently for *Aspisoma*, so that evolution did not need to put any more effort in surface structuring. It is important to understand, that other species of fireflies included in another Family[4] could evolve in a different way. This is actually quite probable, as bioluminescence originated several times during evolution. The means by which each species of firefly increases its light extraction could be unique. These informations are important for the following chapters, as we chose - partly from this observation[5] - to focus on and only investigate further the the jagged-scale structure found on the *Photuris* firefly.

The detailed analyze of the *Photuris* firefly with all the substructures is described in my Master thesis [82] and was published in *Optics Express* [92]. In this manuscript, we will focus mainly on the jagged-scales shape found on the cuticle of the *Photuris* firefly. This structure appeared, from our earlier work, to be the most effective and the complete modelization of this structure is described in detail in the following chapter.

[4] see phylogenetic relationships in the Materials and Methods chapter.
[5] This decision was also motivated by calculations explained more in detail in the following chapter

Chapter 4

Pattern on the lantern of *Photuris* for light extraction enhancement

The jagged-scale shaped arrangement of the scales enhances the light extraction of the light extraction significantly. This result can be concluded from the previous work published in *Optics Express* [92], based on works initiated during my Master thesis [82]. In this chapter we will specifically explain how the light propagates through this specific interface and compare the result to those generated by a plane interface, as described in chapter 1. The arguments will be based on computer simulations. The first section gives details about the simulation technique used and the model derived from the jagged scale or jagged-scale pattern found on the firefly. We will then analyze rigorously the light extraction performed by this specific structure. Then a study as a function of the geometrical parameters of the prisms will give an insight about the best geometry of this pattern. Finally we will confirm our simulations thanks to optical measurements.

4.1 Model and Scattering Matrix Algorithm

For the light extraction calculations, we use the Scattering Matrix Algorithm [93] (see Materials and Methods E). This allows us to solve Maxwell's equations in a non-homogeneous medium, where propagation occurs. We use a fully vectorial representation of the light waves and we account for multiple scattering at all stages of the calculations. In the present work, we will simulate a non-polarized incident light, as we have no information about the polarization mode of the firefly light emission. To simulate non-polarized light, we average over the intensity of the two polarization modes, i.e. transverse electric and transverse magnetic. The incident material and the specific structure are considered to be chitin with a refractive index of n_{chitin}=1.56. Julian Vincent, Chair in Biomimetics in the Department of Mechanical Engineering at the University of Bath, advised me that the cuticle of the firefly is made of a chitin-protein composite with a varying amount of water, which could have a significant impact on the refractive index of the incident region. It should be noted that our samples, when submitted to morphology and optical investigations, are dried and that proteins are organic materials with polarizability

similar to chitin. To simplify the simulations and, as we do not have more precise informations about the protein and water amount in the cuticle for the moment, we will consider the incident material as a medium with a homogeneous refractive index of 1.56. The physics behind the specific structure should not be influenced by the precise value. Moreover we will compare the light extraction efficiency of the jagged-scale structure ζ_{struct} (LEE) to the LEE of the plane surface ζ_{plane}, considering the exact same medium as incident region.

$$\zeta(\%) = \frac{I_{trans}}{I_{inc}}.100 \tag{4.1}$$

As the firefly light emission presents a quite narrow spectrum, we will start the simulations for one single wavelength. From chapter 2 we take an average value of 560 nm for the incident light emission. We simulate non-polarized light by taking the intensity average over the TE and TM mode. The assumption of using unpolarized light is justified as no evidence of a firefly response to polarized light could be shown until now.

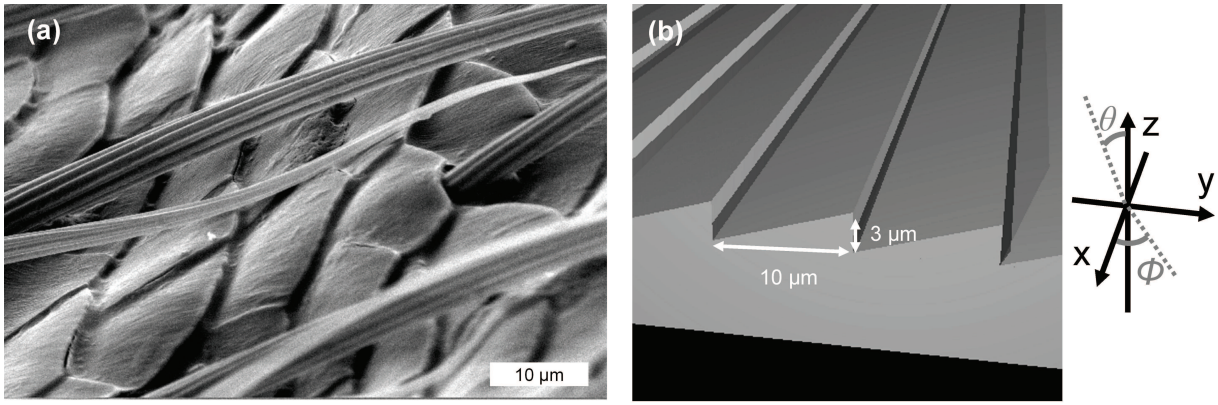

Figure 4.1: Jagged-scale structure. (a) Jagged scales on the firefly cuticle. (b) Inspired jagged-scale pattern used for simulations.

As revealed by SEM, the scales on the cuticle of the *Photuris* firefly protrude with an average height of 3 μm towards the abdominal tip. This protrusion appears with an average periodicity of 10 μm, which is the longitudinal dimension (y-direction) of the scale (see Fig. 4.1). The light propagation could be influenced by two mechanisms with this specific structure: (i) The prisms introduce an angle which changes the distribution of incidence angles in comparison to a plane surface. (ii) Scattering can take place at the sharp edges.

The z-direction is defined perpendicular to the interface. The x and y-direction are defined in the plane of the interface, where the x-direction is defined parallel to the sharp edges and the y-direction perpendicular to the sharp edges. In order to describe the light propagation completely, we should account for the whole range of incident angles. However, the symmetry of the system allows us to reduce the incident polar angles (θ) accounted for from 0° to 90° and incident azimuthal angles (ϕ) from 90° to 270°.

4.2 Light extraction simulations

4.2.1 Convergence with the number of computed diffraction orders

A convergence study has been carried out to establish the number of diffraction orders to be accounted for. The wavelength is fixed to 560 nm and the light is simulated unpolarized. Fig. 4.2 shows the light extraction efficiency (LEE) as a function of the incident polar angle θ, for various numbers of diffraction orders. The azimuthal angle ϕ has been fixed to 90°, i.e. perpendicular to the sharp edge. When accounting for a small number of diffraction orders, the light extraction as a function of the incident polar angle is similar to the extraction curve of the plane interface (see chapter 1). One can already see the effect of the jagged-scale shape, as the light can escape the incident medium over the critical angle of 40°. This effect is increased using 4 and 8 diffraction orders. A radical change in the light extraction behavior is observed with 16 plane waves: the light escapes the incident medium nearly over the whole range of incident polar angles and is not limited by any critical angle. For 32 accounted diffraction orders, the intensity of this effect is again increased. More diffraction orders show nearly complete convergence and are not necessary as the difference between the calculated light extraction intensities is less than 1%. For the following calculations, we will therefore account for 32 diffraction ordres.

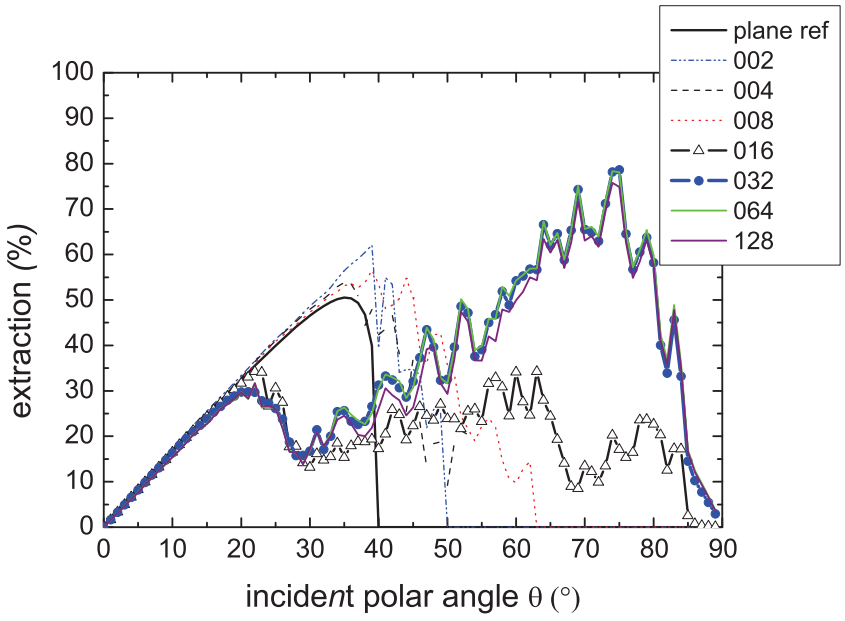

Figure 4.2: Light extraction as a function of the incident polar angle (θ) for a fixed incident azimuthal angle (ϕ=180°), for several computed diffraction orders (λ=560 nm).

4.2.2 Dependence on incident wavelength

To check the dependence of the light extraction as a function of wavelength, values from 400 nm to 800 nm, covering the visible spectra, have been considered (see Fig. 4.3). The calculations

have been carried out for a fixed azimuthal incidence in the direction of the sharp edge ($\phi = 90°$) with 32 plane waves. As the dispersion of chitin is very low [94, 95], i.e. light propagation in chitinous material is not wavelength-dependent, we will fix the value of the refractive index of the incident material and the structures to n_{chitin}=1.56. In this way we can analyze precisely the light extraction dependence for this structure as a function of the wavelength.

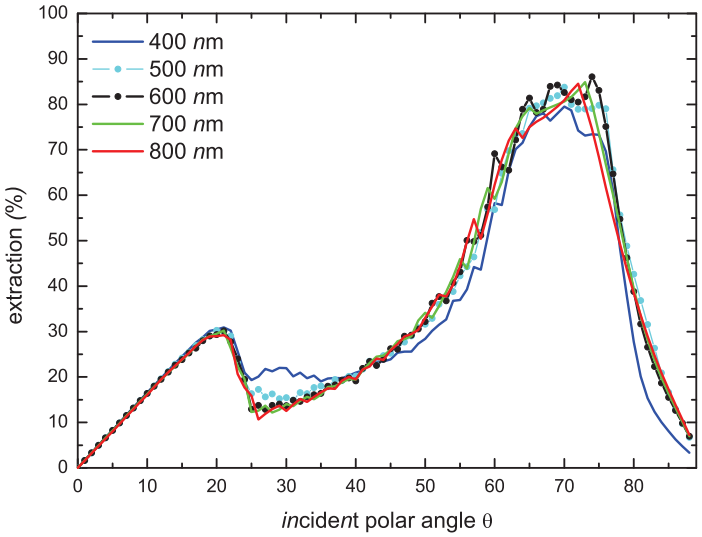

Figure 4.3: Variation of the extraction intensity as a function of the wavelength.

wavelength	$\zeta_{(\phi=90°)}$
400nm	31.7 %
500nm	33.8 %
600nm	33.7 %
700nm	33.3 %
800nm	32.9 %

Table 4.1: Integrated intensity for a fixed azimuthal incidence $\phi = 90°$ as a function of the wavelength.

The integrated intensity changes only by two percent when varying the wavelength (see Table 4.1). This result is not surprising: The period and height of the considered structure are in the range of several micrometers, which is much larger than the considered wavelengths. It is known, that a structure with dimensions close to the size of the wavelength will induce spectral variations to the behavior [96]. In that case, the size of the structure geometry should of course be adapted to the specific wavelength emitted. However, in the firefly case, the period and height of the structures are several times larger than the wavelength and the effect of the structures on the light propagation is therefore nearly independent of the wavelength in the visible range.

4.2.3 Light extraction map

After all these considerations, we can now calculate the light extraction efficiency for the jagged-scale pattern. Figure 4.4 shows the light extraction map for (a) a plane surface and (b) the structured surface. These maps show the light extraction intensity as a function of the incident polar angle θ and the incident azimuthal angle ϕ. The intensity is represented with a logarithmic scale: black areas correspond to zero transmissivity and white areas to maximal transmissivity. The light extraction in the case of the plane interface (Fig. 4.4(a)) is limited by the critical angle of total internal reflection, as seen before (chapter 1). Light that impinges on the interface with a polar angle larger than $\theta = 40°$ cannot escape the material because of the total internal reflection. This phenomenon is independent of the incident azimuthal angle ϕ, because of the symmetry of the interface. The light extraction map of the jagged-scale shaped interface is completely different (Fig. 4.4(b)). Light extraction is not limited by total internal reflection over the whole range of incident azimuthal angles ϕ anymore. By contrast, for an azimuthal angle perpendicular to the sharp edge (ϕ=90°), the light can escape the incidence region without any limitation imposed by a critical angle. This behavior has been observed already during the convergence study (see section 4.2.1). When the light rays impinge on the interface parallel to the sharp edges $\phi = 180°$, the light extraction is again limited by the critical angle and the light extraction falls to zero beyond the polar incident angle of θ=40°. With this specific azimuthal incident angle, the structure is invariant in the direction parallel to the incident wave vector and the propagation is weakly influenced by the jagged-scale pattern. The limitation of the extraction is consistent with the translational symmetry of the structure. When the polar incidence is again perpendicular to the sharp edge, but this time in the direction of the slope ($\phi = 270°$), the light extraction is again enhanced and not disturbed by total internal reflection. The effect is somewhat less effective than in the case $\phi = 90°$. This is clearly understandable, considering the asymmetry of the interface.

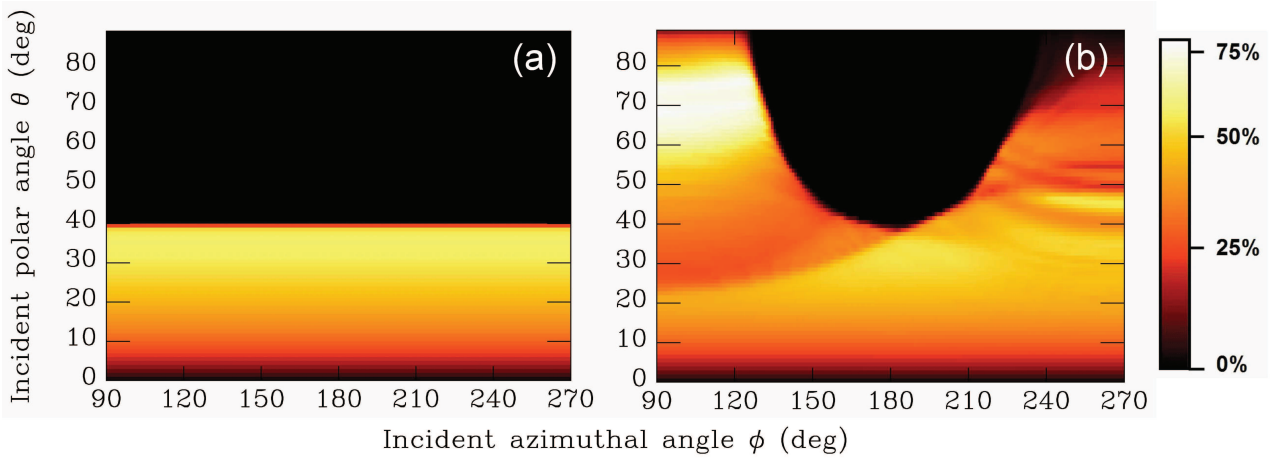

Figure 4.4: Light extraction maps, logarithmic scale. (a) Plane surface. (b) Jagged scale pattern.

The graph on Fig. 4.5 shows the light extraction as a function of the incident polar angle θ for various fixed azimuthal angles ϕ (90° - 180° - 270°). One can see that the light extraction is enhanced above the critical angle for incidences perpendicular to the sharp edges. When the incidence gets parallel to the protruding end, the light extraction gets similar to the one of the plane surface (see Fig. 4.4).

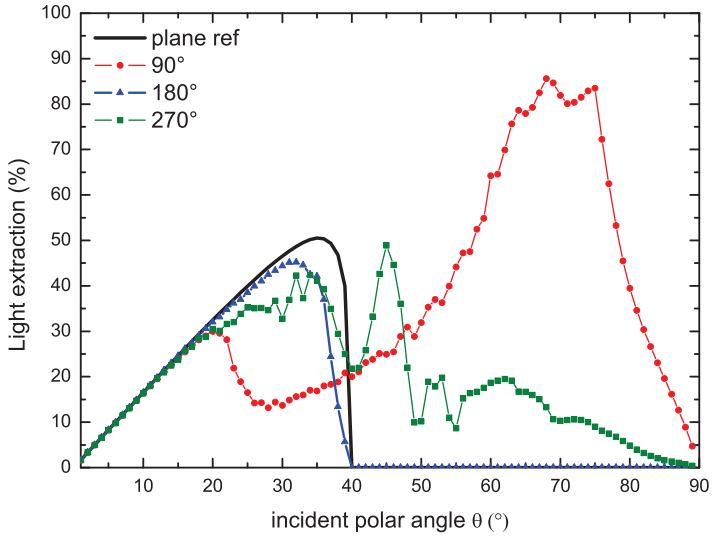

Figure 4.5: Light extraction for the jagged-scale surface as a function of the incident polar angle θ. Fixed azimuthal angles ϕ.

These graphs show readily that the specific structure of the firefly enhances the light extraction efficiency. However, one value is still missing: in the second chapter we saw that only 20% (ζ_{plane}) of the produced light inside the chitin can effectively escape the material into air, which gives a very poor efficiency. When adding the jagged-scale structure 29% (ζ_{struct}) of the light can escape the incident medium, which gives an LEE improvement of $\Delta\zeta$=45%. This gain is achieved mainly through two mechanisms: (i) the prisms change the geometry of the interface completely. An angle which would impinge with an angle bigger than the critical angle onto the hypothetical plane interface can still be under the critical angle in this new jagged-scale shape. This bypasses the effect of the total reflection for a specific range of azimuthal angles ϕ. (ii) The sharp edge gives rise to a scattering mechanism which opens a new channel to allow for light to exit and thereby enhances light extraction.

4.3 Influence of the all the substructures on the light extraction efficiency

It should be recalled, that in the firefly lantern, other optical inhomogeneities also contribute to the light extraction. The detail of these calculations are not exposed in this manuscript, as they were detailed in my Matserthesis [82] (in French) and published in *Optics Express* [92]. Figure 4.6 shows a schematic view of the construction of the bioluminescent organ and the cuticle above it. The cuticle shows – besides the jagged scales – a smaller-scale, sinusoidal corrugation. The period of this structure is 250 nm and height of 100nm. The hypothesis of an anti-reflective layer was emitted, but the simulations showed that the LEE is only enhanced by 1%. This structure was therefore neglected in the following. The light is emitted in the peroxisomes (represented here as brown spheres). As the experiment at the ESRF showed that the distribution of the spheres is completely random, we can take an average value for the refractive index to simulate the incident medium. The peroxisomes contain urate, which has a lower refractive index than chitin (n_{urate}=1.4). The inter-spherical space is probably filled with liquids, for which we will consider a refractive index of n_{liquid}=1.33. The filling factor of the spheres has been estimated to f=0.74 for a close packed arrangement of the spheres [97]. The mean value of the refractive index can then be calculated by the following expression

$$\overline{n} = \sqrt{\overline{\varepsilon}} = f\ (n_{urate})^2 + (1-f)\ (n_{liquid})^2 = 1.38$$

For a refractive index of n=1.38 of the incidence medium, the critical angle is increased up to 46.6° which enhances already the light extraction efficiency for a plane surface up to $\zeta_{plane,n=1.38}$=28%. The presence of the intermediate layers, which constitute the bulk of the firefly cuticle, has been taken into account as well. The first encountered layer for the emitted light is the cellular wall of the photocyte, followed by the muscular layer (green and red, respectively, on Fig.4.6). For the multilayer in the volume of the cuticle (Grey on Fig. 4.6) we calculated an average refractive index considering the incident light polarization, using the directions described by Vigneron *et al.* [98]. Table 4.2 summarizes the values of refractive indexes and thicknesses of the intermediate layers considered for simulation.

layer	$\overline{\mathbf{n}}$	**thickness**
cellular wall	1.56	60 nm
muscular layer	1.33	90 nm
multilayer	1.38	2.4 μm

Table 4.2: Summary of the intermediate layers between the bioluminescent organ and the jagged scales structure.

The light extraction is then nearly doubled: $\zeta_{Photuris}$=40% [92]. The explanation therefore stays (i) essentially in the lower refractive index of the incidence region. Actually, only two parameters define the value of the critical angle: the refractive index of the incidence medium and the refractive index of the emergence medium. Their ratio determines the aperture of

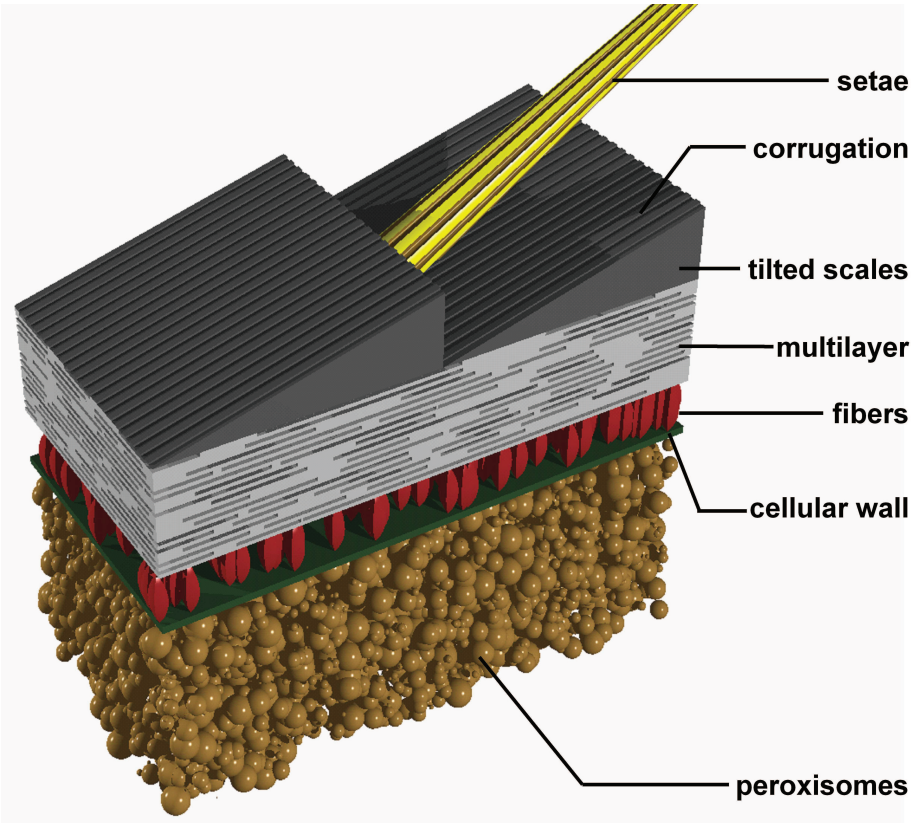

Figure 4.6: Schematic representation of the bioluminescent organ and the cuticle.

the extraction cone for light into free space and thereby highly influences the extraction efficiency. (ii) Moreover, the intermediate layers have intermediate refractive indexes between air and chitin. These layers can help to introduce an adiabatic adaption of the refractive index. However, former calculations, where only the influence of the mutlilayer was taken into account, showed that the light extraction id enhanced only by 1%. (iii) The main contribution to LEE enhancement is the specific structure of the cuticle, referred to as jagged-scale, as seen in this chapter.

The jagged-scale pattern of the firefly has been shown to have the largest influence on the overall LEE regarding the structures on or of the cuticle. We will therefore focus the calculations on this specific micrometric jagged-scale pattern in the following work. This decision is motivated as well by our goal to increase the LEE of light-emitting devices. Lowering the refractive index is not easily possible, as the current LED are based on semiconductors with higher refractive indexes.

4.3.1 Partial geometrical explanation of the higher LEE for the tilted-scales structure

The angle at the base of the tilted-scale is 17°, considering an opposite side of 3 μm and an adjacent side of 10 μm. One can see that the highest extraction efficiencies are found at an

incident azimuthal angle close to 90° and an incident polar angle of 70°. This can surely not be a coincidence, as the light-rays are nearly parallel to the tilted slope when considering these polar incidences. They arrive then on the abrupt side (opposite side of the right triangle) with a very small polar incidence and are easily extracted considering that they are then included in the extraction cone defined by Snell's laws (Fig. 4.7).

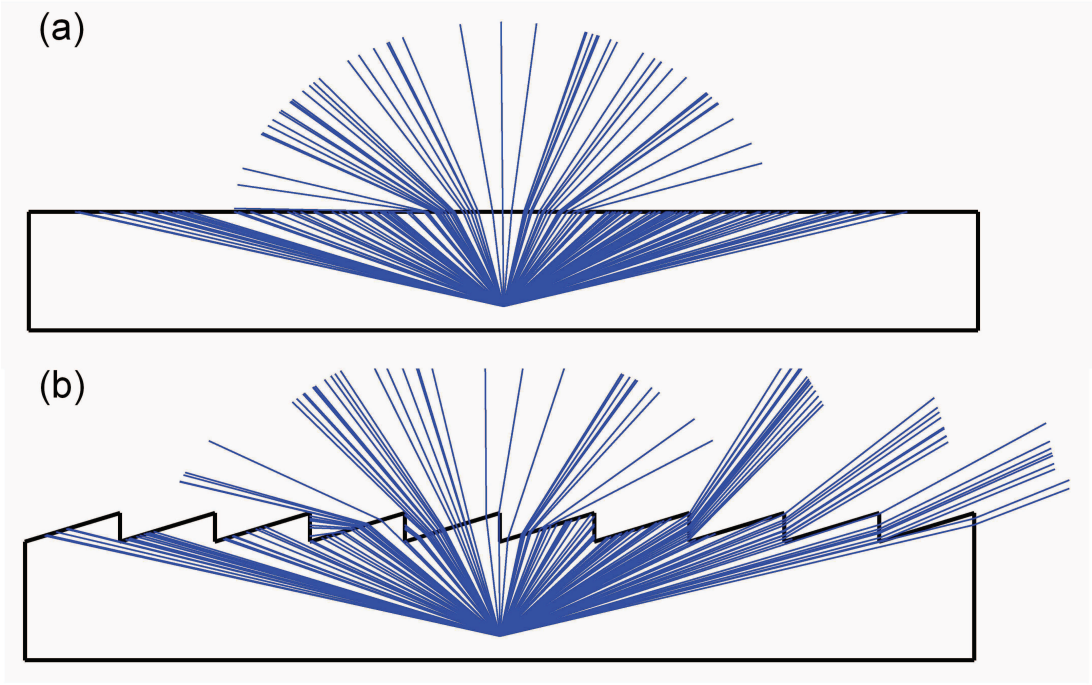

Figure 4.7: Ray tracing. Paths of the light rays in the case of (a) a plane interface and (b) the tilted scale geometry. The light rays have more and wider escape possibilities for the jagged-scale interface as in the plane interface.

4.4 Geometry with the highest LEE?

The geometrical parameters of the jagged-scale structure used for the simulations have been determined as 3 μm for the period and 10 μm for the height. However, will this geometry give the highest possible LEE in a specific range? Figure 4.8 shows the light extraction efficiency as a function of the period (x-axis) and the height (y-axis) of the jagged-scale for values varying from 1 μm to 15 μm with 1 μm steps. This specific range of values has been chosen to fit the requirements of future fabrication techniques used in this work (see chapter 6). The white cross shows the geometrical parameters measured on the firefly. One can see, that this cross is not exactly located where light extraction is as its highest values. Nevertheless, it is really close to the highest LEE. Different aspects have to be taken into account to explain this small difference: (i) Nature faces multi-optimization, i.e. several functionalities have to be taken into account. The firefly cuticle for example should be hydrophobic and present good mechanical stiffness as well as lightness in addition to good light transmission. Therefore the structure may represent

a global for several functions. (ii) The study has been conducted on particular fireflies collected in one spot in the Darien Forest (Panama). Other species could be in a higher evolutional state and have even more efficient structures. (iii) The firefly bends its abdomen over during the light production and the flashing [89]. This induced curvature could slightly change the geometrical parameter of the jagged-scale structure. With a reduced period and an increased height, not present on the dead specimens, a better match with the calculated highest LEE values (Fig. 4.8) may be reached by living specimens.

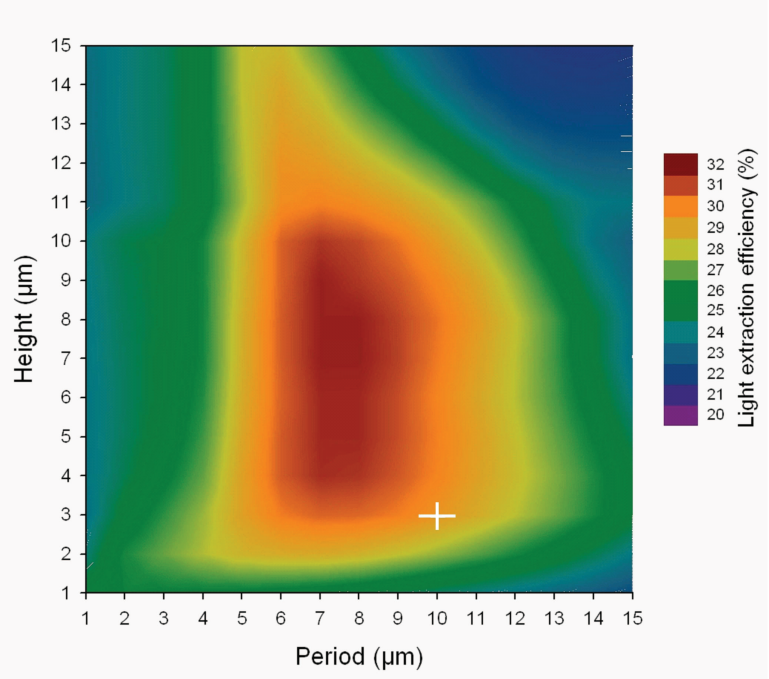

Figure 4.8: Light extraction intensity as a function of the geometrical parameters period (x-axis) and height (y-axis) of the prisms. The white cross indicates the geometric parameters of the firefly (i.e. p=10 μm and h=3 μm)

4.5 Supportive measurements for LEE enhancement for the jagged-scale surface

A measurement has been conducted to give experimental support to the assumption that the jagged-scale structure on the cuticle is mainly the reason for the light extraction increase. As no living fireflies were available, we conducted the experiment on a dead, dried specimen. The abdomen was cut off and isolated. An optical fiber, connected to a high power, highly stable white halogen light source, was introduced at the opening. In that manner we can illuminate the photocytes and simulate approximatively an inner light-production. We then measured the hemispheric radiance of the firefly ventral side with an *ELDIM EZContrast XL*80*MS* scatterom-

eter[1]. We accounted for wavelengths close to the emission peak of the firefly bioluminescence and measured in a solid angle spanning all azimuthal and polar angles from 0° to 80°. The hemispheric transmissivity of the firefly abdomen was calculated by an integration over the measured solid angle. The integrated radiance of the firefly abdomen is shown by the red line on Fig. 4.9. The second measure was carried out on the same firefly abdomen, which has been induced with a certified refractive index liquid, matching exactly the refractive index of chitin, i.e. n_{liquid}=1.56 (*Cargille Labs*). This oil is supposed to reduce the sharp corrugation of the protruding edges and in this manner reduce as well the light extraction. The result is shown by the blue line on Fig. 4.9. Only the ratio of this measurement can be compared to the theoretical values, as the reference systems are optically different. The measured efficiency enhancement due to the corrugation in comparison to the coated surface reaches 7%.

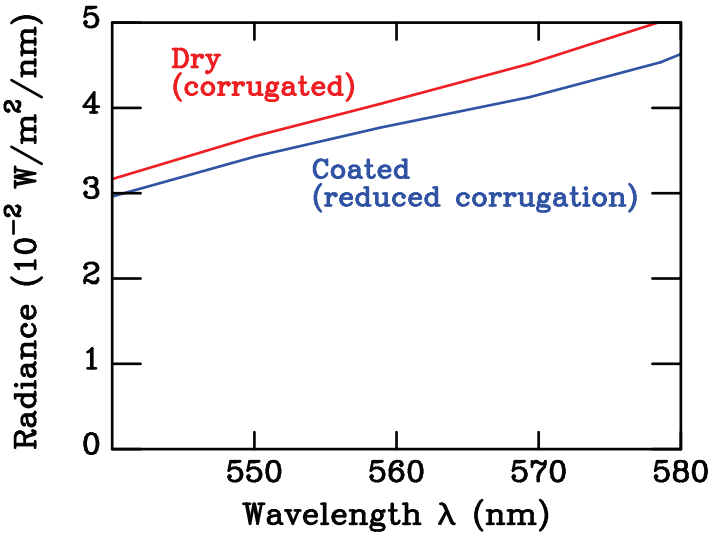

Figure 4.9: Measurement of the light transmittance through a firefly abdomen, comparing a structured surface with a coated surface. The diagram shows the hemispheric integrated intensity as a function of the wavelength.

This value has to be taken with some precautions: The references taken for the simulation and the measurements are different and it is not possible, for the moment, to recreate the exact same conditions in measurements as for the simulations. A possible measurement which could be considered as equivalent to the simulations would be to measure the emission of a firefly kept alive and compare this to the "oil-coated" firefly emission. This measurement will as well be difficult, as the firefly often stops the light emission when put in inconvenient positions. Another factor that is not really controlled is the coating "quality" of the firefly abdomen. As seen before, the firefly has a multi-functionalized cuticle with hydrophobic properties. The coating with the oil could therefore be not optimal and also not eradicate the jagged-scale structure completely. However, the measurement indicates a tendency which confirms the positive influence on the light extraction efficiency from the jagged-scale pattern as seen in the simulations earlier in this

[1]For details about the scatterometer, refer to the "Materials and Methods " chapter at the end of this manuscript (chapter 6.6).

chapter.

4.6 Conclusion

As a conclusion of this chapter, we can say that this studied firefly species displays a structure on the cuticle -a jagged-scale structure - which enhances effectively the light extraction efficiency. The structure found on the cuticle is only a rearrangement of existing scales, which changes the properties of the interface in such manner that the light can easily escape the chitin body of the firefly and in that way minimizes photons losses by total internal reflection.

Chapter 5

Modeled structures inspired by the jagged scales

In the previous chapter, we analyzed the factory-roof shape inspired by the jagged scales of the lantern cuticle. The light extraction efficiency (LEE) is largely enhanced by this asymmetric shape in comparison to a plane surface. In this case, nature seems to have indicated a good way to improve the LEE. However a question that is often raised is the efficiency of a similar, but symmetric shape. Would it not be even better?

In this chapter we will consider structures inspired by the firefly factory-shape and analyze these in the same manner, i.e. make a convergence study, calculate the geometry of structure with high light extraction efficiencies and draw the light extraction map. We have already published the work described in this chapter was published in *Optical Engineering* [99]. The simulations here are however more precise as simplifications, done in the former paper for the three-dimensional structure, could be avoided.

5.1 Two-dimensional symmetric triangular structure

The first structure is a two-dimensional pyramid structure which is very close to the former described factory-roof shape (Fig. 5.1). The main difference between those two structures is the symmetry, respectively the asymmetry. The slanted slope is similar in both cases, however the highest point of the structure is less sharp in the triangular case than in the firefly case.

5.1.1 Light extraction paths

Figure 5.2 shows the light extraction intensity as a function of the incident polar angle θ for a fixed azimuthal incidence (ϕ=90°) and for different values of the accounted plane waves. We recalled the results of the firefly acquired earlier to start the comparison of efficiency between these different structures. The black continuous line on each graph shows the result for a plane surface. The conditions of calculation are similar to the conditions in the previous chapter: (i) For the incident refractive index we take the value of chitin, i.e. n_{chitin}=1.56. (ii) As the

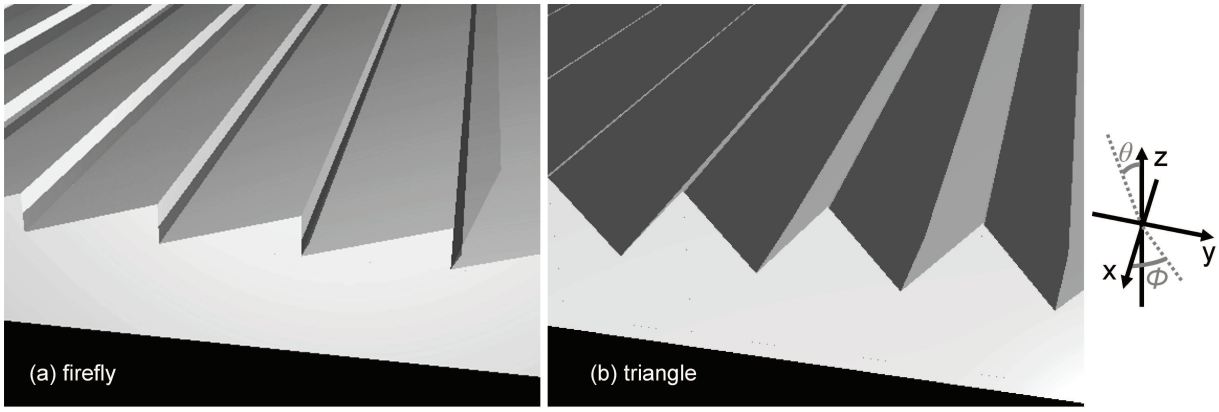

Figure 5.1: (a) Firefly inspired factory-roof shape. (b) Symmetric triangular shape. By contrast to the firefly shape, the triangular shape is symmetric.

dispersion of chitin is low and the structures are to big to be sensitive to the wavelength, we use only one wavelength for calculations, i.e. λ=560 nm (see chapter 4). (iii) We simulate non-polarized light by taking the intensity average over the TE and TM mode.

One can easily see that, by accounting for 32 plane waves, we can properly simulate the light propagation through the triangular structure (Fig. 5.2) and that this shape is more effective than a plane interface (represented by the black line on the graphs of Fig. 5.2). The extraction intensity falls to zero only *after* the critical angle of θ=40°. The extraction intensity of the firefly is still more effective in this specific azimuthal incidence, as the enhancement above the critical angle is higher. However, these graphs can not lead to any conclusion, as the extraction intensities are dependent of the azimuthal incidence and we only considered the incidence with the highest extraction of the firefly case. The next steps are (i) calculate the overall integrated extraction intensity for different geometrical parameters and (ii) analyze the light extraction map for the best geometry.

5.1.2 Search for the maximal-LEE geometry

The maps on Fig. 5.3 show the integrated light extraction intensity as a function of the period and height of the considered structures (as seen in the previous chapter, section 4.4), for values varying from 1 μm to 15 μm with 1 μm steps. The map corresponding to the triangular shape shows variations akin to those of the firefly structure. However, the highest extraction intensities are reached only for larger heights, starting at 5 μm instead of 3 μm as in the firefly case. The geometry with the highest LEE for the triangular structure has a period of 8 μm and a height of 7 μm and gives an integrated extraction intensity of 30%. This value is lower than the highest achieveable value for the firefly case, i.e. 32% (p=8 μm - h=7 μm). It would be interesting to see how the firefly structure is more effective than the other structures. This information can be deduced from the light extraction map and will be treated in the next section.

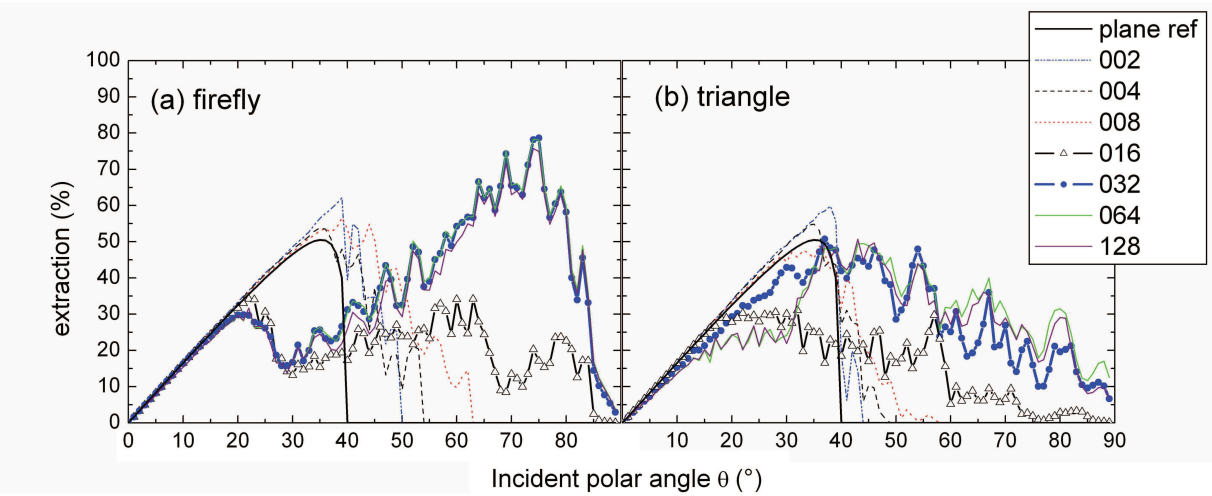

Figure 5.2: The convergence calculation of the different structures have been realized for a fixed azimuthal angle $\phi = 90°$. 32 plane waves are enough to account properly for the effect of the structures in both cases.

5.1.3 Light extraction maps

The maps show on Fig. 5.4, as in the previous chapter, the hemispherical integrated light extraction intensity as a function of the incident polar angle θ and the incident azimuthal angle ϕ. The intensity is represented by a logarithmic scale, where black areas correspond to zero transmissivity and white represents maximal transmissivity. The map of the triangular structure is similar to the one of the firefly structure. Light is extracted above the critical angle for azimuthal incidences from 90° up to 150° and again at azimuthal incidences above 210° in the analyzed range. Contrasting the firefly map, the light extraction enhancement is symmetric, which can be traced back to the symmetry of the structure. It should be noted that the main difference in this structure is the wedge: in the firefly case it is sharper and more abrupt as in the triangular case. Scattering is stronger in the case of the firefly sharp edge than in the case of the triangular wedge.

This hypothesis can be made from the previous convergence analysis, where the intensity of the light extraction above the critical angle was smaller in the triangular case than in the firefly-case (see Fig. 5.2).

5.2 Three-dimensional symmetric pyramid structure

In this section, we will consider the light extraction by a three-dimensional pyramidal structure. To compare the two-dimensional firefly structure with a three-dimensional pyramid structure, some cautions should be applied. In the case of the firefly, we accounted for 32 plane waves in the y-direction, i.e. the direction of the factory-roof shape. This value has been determined by a convergence calculation. The x-direction is invariant and we accounted therefore only for one plane in this direction. In the case of the pyramid structure, we cannot take the same

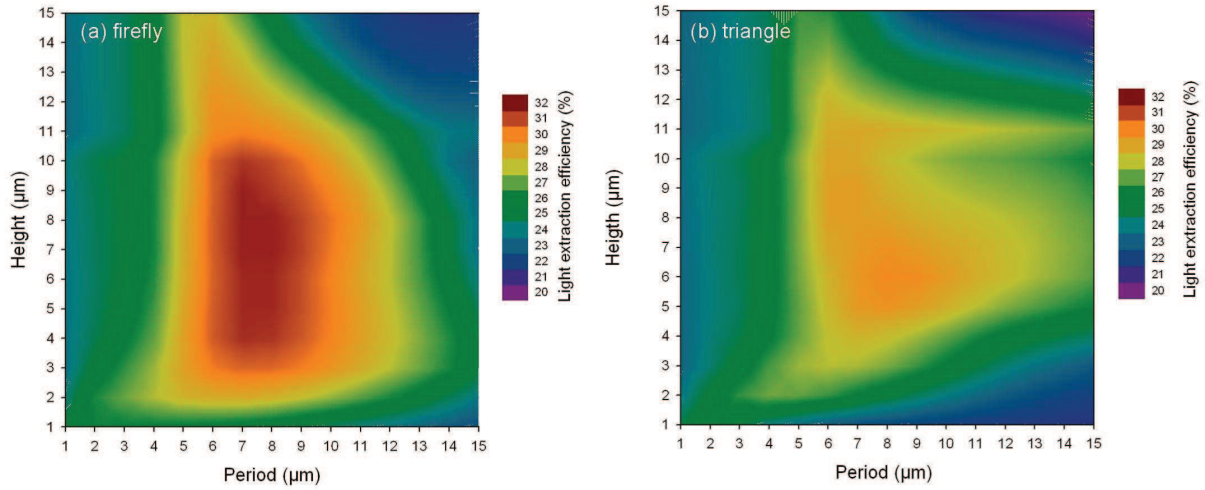

Figure 5.3: Light extraction intensity as a function of the geometrical parameters period (x-axis) and height (y-axis) of the structures. (a) Firefly. (b) Triangle.

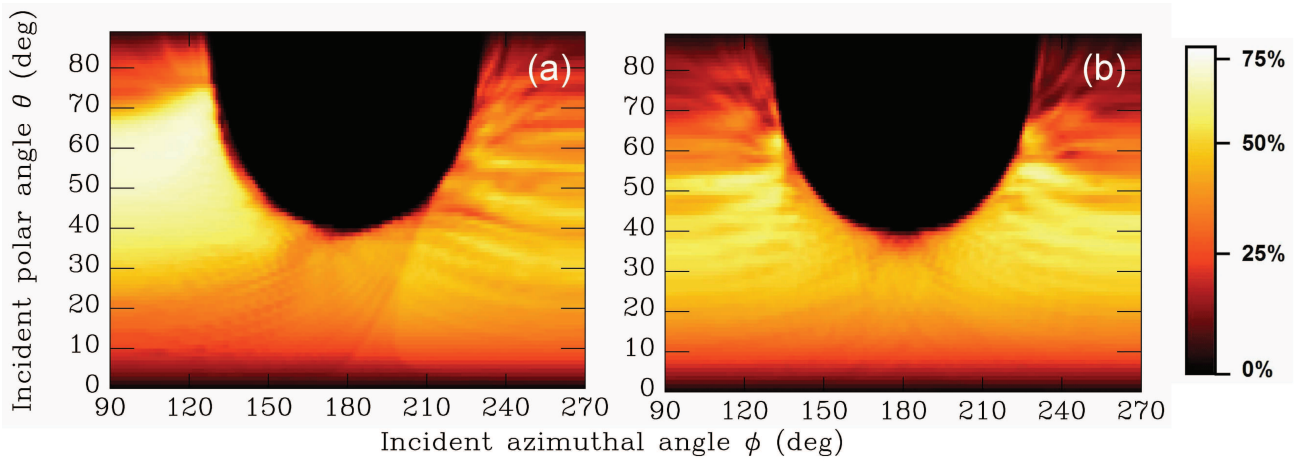

Figure 5.4: Light extraction maps. Logarithmic scales. (a) Firefly. (b) Triangle.

values, as the x- and the y-directions are both inhomogeneous. The other way around, it is not necessary and has no physical meaning to send more than one plane wave to investigate an invariant direction (firefly case). The calculations for these two different structures can, at this moment, not be carried out under the exact same conditions. For the firefly study, we would need 32 plane waves. For the pyramid structure, we would then need 32 plane waves in both directions. This gives a total of 1024 incident plane waves, which requires to much memory for the current computing system available.

Relaxing accuracy requirements, it was determined that the calculations in this section could be carried out with a total of 64 plane waves (8×8). This plane waves basis was commonly accepted for similar three-dimensional grating problems with moderate refractive index contrasts.

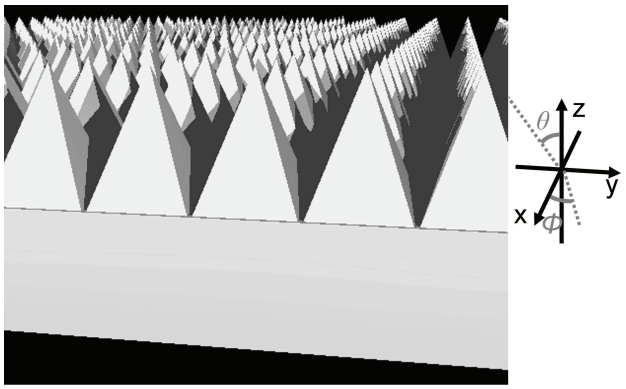

Figure 5.5: Three-dimensional pyramid structure.

5.2.1 Search for the maximal-LEE geometry

The map of the overall integrated light intensity as a function of the period and height of the pyramidal structure clearly shows parameters of the structure geometry with maximal LEE (Fig 5.6). The range of maximal LEE values is more limited than in the case of the firefly and the light extraction efficiency decreases more rapidly with growing size. Moreover the period and the height of the high-LEE geometry is much smaller than in the previous case, p=3 μm - h=2 μm and p=8 μm - h=7 μm with extraction values of $\zeta_{pyramid}$=32% and $\zeta_{firefly}$=32%, respectively. The high-LEE geometry in the considered range of values, gives a simiar light extraction efficiency ζ as in the firefly case. However, it should be noted, that the light extraction efficiency decreases much more rapidly beside the range of high-LEE values than in the firefly case. These values are very localized and a slight change in the geometry has agreater impact on the LEE than the height of the structure. For a fixed period in the high LEE range, several heights give good extraction efficiencies.

5.2.2 Light extraction map

Figure 5.7 shows the light extraction map for the pyramid structure. Light extraction is enhanced over the whole range of incident azimuthal angles ϕ. The extraction cone is enlarged up to an incident polar angle of 70° to 75°, depending on the azimuthal incidence. When we compare this result to the firefly case two differences can be noticed: (i) The extraction efficiency is still limited to a specific angle. Extraction does not occur for angles higher than 75°. (ii) On the other hand the phenomenon is equally distributed over the whole range of incident azimuthal angles. In the two-dimensional case preferential incident azimuthal directions exist. The latter difference is easily understood, when taking the symmetry of the three-dimensional pyramid structure under consideration: the symmetry would allow to compute the light extraction only for an azimuthal angles range extended over 90°. The simulations were done over a range of 180° to be consistent with the light extraction maps shown in the previous section and previous chapter. The reminiscent presence of a critical angle in the three-dimensional case by contrast to the two-dimensional case is less obvious. In the two-dimensional firefly case, the

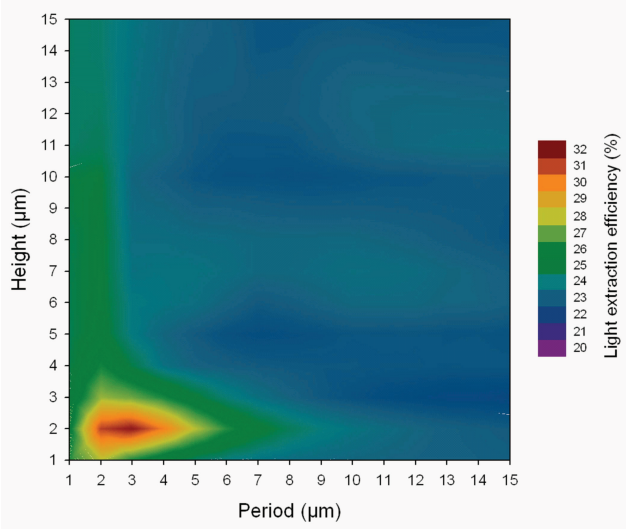

Figure 5.6: Light extraction intensity as a function of the geometrical parameters period (x-axis) and height (y-axis) of the structures.

paths of the light extraction were simulated by ray-tracing (see chapter 4, Fig. 4.7). For this structure it is possible to transpose the reasoning to a one-dimensional case and the schematic representation explains very well the increased light extraction for high polar incidences. In the three-dimensional case, this reasoning can not be applied as easily because the structure varies in the x-direction as well and the pyramid-tip surface is therefore limited. The translational invariance in the x-direction gives an advantage in comparison to the three-dimensional structure.

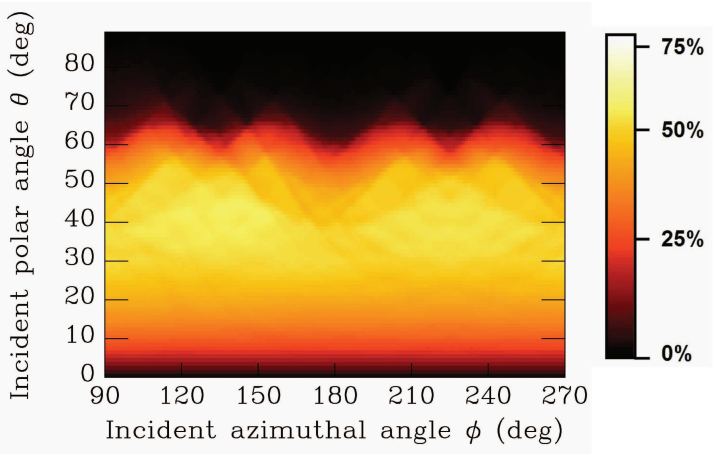

Figure 5.7: Light extraction map of the pyramid structure. Logarithmic scales.

5.3 Firefly, triangle or pyramid for fabrication?

This chapter studied two new morphologies: (i) a two-dimensional symmetric triangular structure and (ii) a three-dimensional symmetric pyramid structure. In both cases an investigation of the maximal LEE geometry was performed. Table 5.1 summarizes the main characteristics of each studied structure. The high-LEE geometry for the two-dimensional triangular structure is very close to that found for the firefly structure, whereas the three-dimensional pyramid structure has high-LEE values at a smaller scale. Another difference that should be noted is that the light extraction efficiency decreases much more rapidly for the three-dimensional structure and is thereby more sensitive to the geometrical parameters. This means that the fabrication process needs to be more precise as a small change in the geometry has a strong impact on the LEE. The light extraction efficiencies achieved by each high-LEE structure are comparable for the firefly and the three-dimensional pyramid structure.

	Firefly	**Triangle**	**Pyramid**
LEE$_{max}$	32%	29%	32%
Geometry	2D	2D	3D
High-LEE geometry	p=7 μm h=8 μm	p=7 μm h=8 μm	p=3μm h=2μm
High-LEE range	large	large	small

Table 5.1: Summary of the characteristics for LEE of each studied structure.

With these characteristics in mind, we will prefer the larger scale asymmetric firefly structure, for several reasons: First of all, fabrication can be easier for two-dimensional and larger structures, than complex three-dimensional shapes. Moreover, the firefly structure gives a greater range of high-LEE geometrical parameters. The firefly structure gives for equal LEE a higher flexibility for fabrication processes than the three-dimensional structure.

The research works described in the first chapter concerning the light extraction enhancement of LEDs (section 1.2), use often three-dimensional structures to achieve better efficiencies. In photovoltaics and solar thermal energy systems, where the problem is reversed (in terms of refractive indexes) and the highest possible percentage of light should be absorbed. We can also find a large amount of literature about three-dimensional transmission-enhancing structures (for example [100–103]). It is then somehow surprising to conclude, in the present work, that the most efficient structure in the light extraction case is two-dimensional.

Chapter 6

Biomimetic inspiration for light extraction enhancement of existing light-emitting devices

The previous chapters asserts that the factory-roof structure on the cuticle of the firefly lantern enhances the light extraction considerably and the comparison with similar shapes, showed that the firefly structure is the most suitable for the following fabrication process. In this chapter a biomimetic application is described: the specific firefly structure is adapted by simulations to be deposited on an existing light-emitting device (LED). Nicolas André, then postdoctoral researcher at the University of Sherbrooke and now researcher at the University of Louvain-la-Neuve, has found a way to reproduce the structure in photoresist by laser-lithography on a blue GaN-based LED. We applied optical measurement techniques similar to those used for characterizing the natural structure to asses the light extraction improvement. All the different simulations that provided parameters for this fabrication and all the measurements to characterize the final product were carried out at the University of Namur. The fabrication of the device was carried out at the University of Sherbrooke (Canada). The work described here was published in *Optics Express* [104].

6.1 LED layout

The considered light-emitting device is a gallium-nitride (GaN)-based LED. LED's have been developed for several years now. Electroluminescence has been discovered in 1907 by the British experimenter H. J. Round (Marconi Labs) [105]. In 1955 the Radio Corporation of America reported on infrared emission from gallium arsenide (GaAs) and other semiconductor alloys [106]. The first developed visible-spectrum LED emitted red light and was developed by Holonyak *et al.* in 1962 [107]. Orange, yellow and green LED could be developed and the emission improved quite easily after the first steps taken. However before a white LED could be created, the emission of blue light was needed. In 1974 the electroluminescence of GaN was discovered in the blue range. The problem for the creation of blue light-emitting diodes was the p-doping of the

III-V nitrides, and specifically GaN. The first high brightness blue InGaN/AlGaN LED was described in 1994 by Nakamura *et al.* [108], as the group could perform the first efficient p-doping with magnesium of the AlGaN layer. There are two ways to create white LEDs: (i) using an RGB-system, where the white light is created with three colored LED's (red-green-blue) or (ii) using an phosphorescent material to convert monochromatic light into a broad-spectrum white emission. White high power LEDs were first commercialized in 1996 with a luminous efficacy of 5 lm/W. Nowadays the luminous efficacy of white LED easily exceeds 100 lm/W. The highest announced efficacy has been measured for a pure green light LED emitting at 555 nm, reaching 683 lm/W [109]. Haitz's law formulates, that every 10 years the amount of light generated by an LED increases by a factor 20 at least and the cost per lumen decreases by a factor 10 [110].

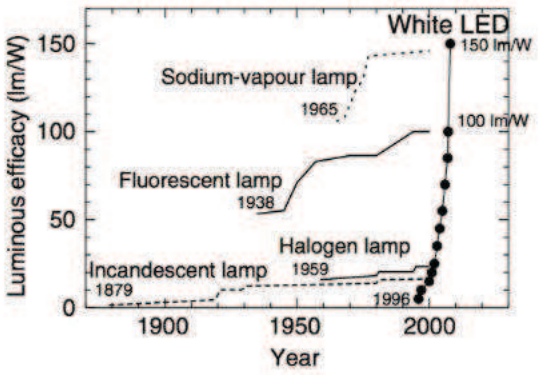

Figure 6.1: Luminous efficacy improvement of light sources.

Figure 6.2 shows the cross section of the considered LED. The starting chip is a sapphire substrate. On this chip AlGaN/GaN hetero-structures are grown by hybrid vapor phase epitaxy (HPVE) [111]. (i) In the first step 1.5 μm mesas are created by a Cl_2/Ar inductively coupled plasma etching using a KMPR® photoresist mask. (ii) After cleaning the chip a recrystallization annealing is operated at 600°C during 20 min in order to reduce the defects caused by the previous etching. (iii) In the third step, the current-spreading layer, the n-pad and the p-pad are deposited by metal evaporations and lift-offs. The current spreading layer is required to increase the poor electric performance of the p-GaN, by distributing the charges homogeneously over the film. After each lift-off, several thermal annealing (of 1 min each) are performed, which ensures low-resistance ohmic contacts. (iv) At last, the spreading layer is annealed under air atmosphere, instead of N_2 atmosphere, to oxidize the nickel layer. Those specific conditions for the annealing process offer a good compromise between the electrical conductivity and the optical transmittance, considering that the light produced in the GaN chip has to pass the current spreading layer. The annealing temperatures are respectively 580°C, 550°C and 500°C.

In the following, the model of the above presented LED considered for light propagation simulation is described. The **active material** is gallium nitride (GaN). The light emission peaks at 425 nm (see Fig. 6.3). The pemittivity of GaN at a wavelength of 425 nm is $\varepsilon_{(GaN,\lambda=425nm)}$=6.36. The calculation is carried out at a fixed wavelength of 425 nm. In chapter 4, the light extraction for the considered structure as a function of the wavelength

	p-GaN	p-AlGaN	active GaN	n-AlGaN	n-GaN
Thickness	650 nm	150 nm	100 nm	250 nm	7 μm
	Sapphire	**Ni/Au (p-pad)**	**Ti/Al (n-pad)**	**Ni/Au* (spread.)**	
Thickness	430 μm	20 nm/500 nm	20 nm/500 nm	5 nm/5 nm	

Table 6.1: LED layers thicknesses. (**before annealing*)

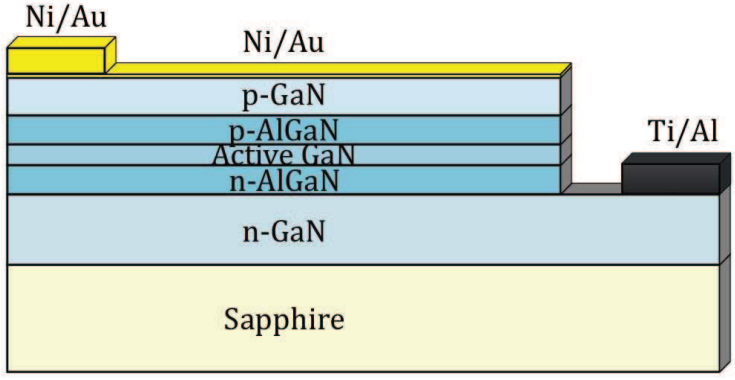

Figure 6.2: AlGaN/GaN LED heterostructure cross-section

has been studied. The difference in light extraction was shown to be very low. The result is not surprising, as the considered structures are much larger than the wavelengths. The light emission of the GaN-based LED ranges from 380 nm to 550 nm (Fig. 6.3). The full width at half maximum (FWHM) is 63 nm and ranges from 404 nm to 467 nm, where the values of the dielectric constant of GaN are respectively $\varepsilon_{(GaN,\lambda=404nm)}$=6.52 and $\varepsilon_{(GaN,\lambda=467nm)}$=6.10. The dispersion of the dielectric constant for the FWHM of the LED emission is lower than 0.5 (see inset Fig. 6.3) and will therefore be neglected in this calculation. Over the active material, a **current-spreading layer** is required to increase the electric performance. For this layer 5 nm of nickel and 5 nm of gold are deposited. The permittivities of nickel and gold at 425 nm are respectively $\varepsilon_{(Ni,\lambda=425nm)} = -3.66 + i8.11$ and $\varepsilon_{(Au,\lambda=425nm)} = -1.55 + i6.30$ [112]. These values have been taken to calculate the light extraction of the plane model. The values taken for the current spreading layer may seem as a harsh simplification, as the layer is oxidized. Ho *et al.* analyzed the oxidized Ni/Au layer after being heat treated under TEM (transmission electronic microscope) and showed that the film is constituted of crystalline NiO, Au and amorphous Ni-Ga-O phases [113]. The deposited Au film was not continuous after the annealing and showed islands on top of the *p*-GaN. The NiO formed a continuous film, covering the Au islands and the amorphous Ni-Ga-O phase. According to Smalc-Koziorowska *et al.*, the annealed contact layer consists of three different features: Ni, Au and NiO [114]. Nickel is even observed in its metallic state in the deepest part of the contact but the deposition thickness are higher than in our case (20 nm and 5 nm respectively). These observations justify without doubt the dielectric constant for gold taken from the *Handbook of Optical Constants of Solids* [112]. For the NiO layer, the choice is somewhat more tricky: the nature of the layer containing oxygen after annealing is

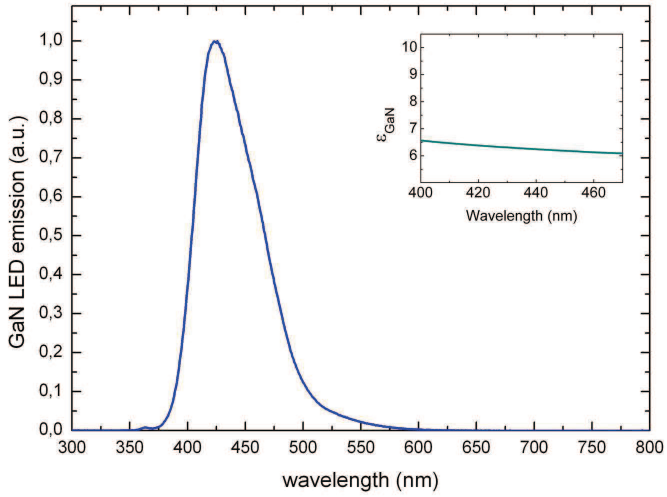

Figure 6.3: Emission spectra of the GaN-based LED.

still not completely understood. In this specific case, we will keep the value of nickel given by the *Handbook of Optical Constants of Solids* [112]. First, the deposited layers are very small in comparison to the emission wavelength (5 nm each, 1/80 λ_{GaN}) and should therefore not have be a determining factor. Moreover, the reference, plane interface and the jagged-scale interface are both simulated with exactly the same permittivities. The main interest of this work is to determine the exact effect of the jagged-scale structure. Taking the permittivity value of nickel instead of nickel oxide is therefore acceptable in our case.

The specific factory-roof shaped structures were created in *Clariant AZ* 9245® **photoresist**. The dielectric constant of this resin is $\varepsilon_{(resist,\lambda=425nm)} = 2.76$[1].

The calculation of the light extraction efficiency for a plane surface shows that only 3.7% of the light can be extracted, due to the limited extraction cone. This result is even lower as the values announced in chapter 1, i.e. 6%, because of the current-spreading layer, which absorbs a certain amount of light, due to the presence of nickel and gold.

6.2 Search for the maximal-LEE geometry

This calculation is carried out under the same conditions, regarding the symmetry and the number of plane waves, as the one for the firefly described in chapter 4. We simulate as well non-polarized light by taking the intensity average over the TE and TM mode. The simulations are carried out at a wavelength of 425 nm (see previous section). A schematic representation of the model is shown on Fig. 6.4.

The period (p) and the height (h) vary from 1 to 15 μm with a step of 1 μm. In addition, the region below the micrometer was also considered (see Fig. 6.5). As in the case of the firefly,

[1]The imaginary part of the refractive index given by the manufacturer is $k = 0.0002$ which will be neglected for these calculations.

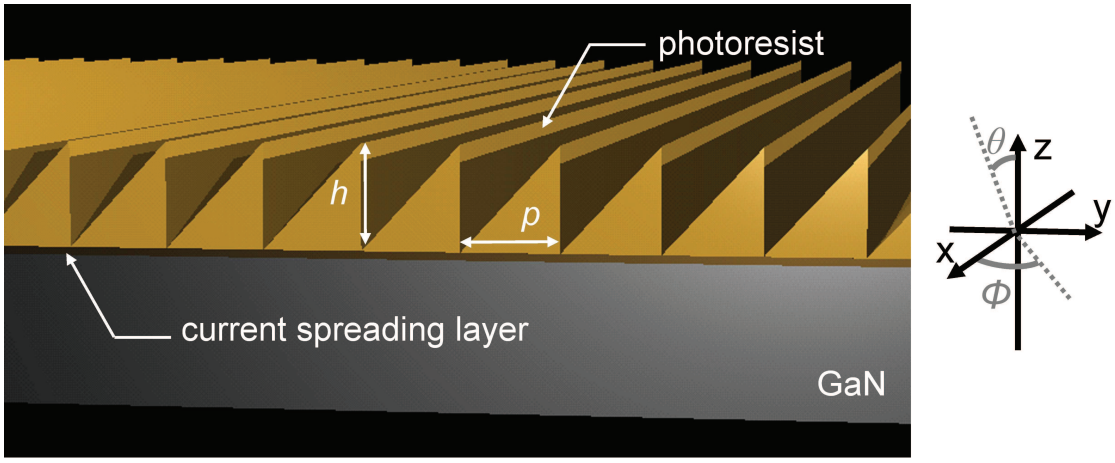

Figure 6.4: Schematic view of the model used for the simulations described in this section.

there is clearly a configuration with a high LEE for the prism geometry. The highest extraction is achieved for a period of 5 μm and a height of 6 μm. The extraction gain reaches $\Delta\zeta$=55%. For smaller geometric values such that $1 \leq p, h \leq 2$ μm the light extraction improvement is only $\Delta\zeta$=30% (see detail on submicron geometry in Fig. 6.5). This analysis in the submicron range shows clearly that, to solve the problem of low light extraction efficiency, physisicts and engineers should not only concentrate on geometries with sizes close to the wavelength. This knowledge has been constructed by closely observing nature.

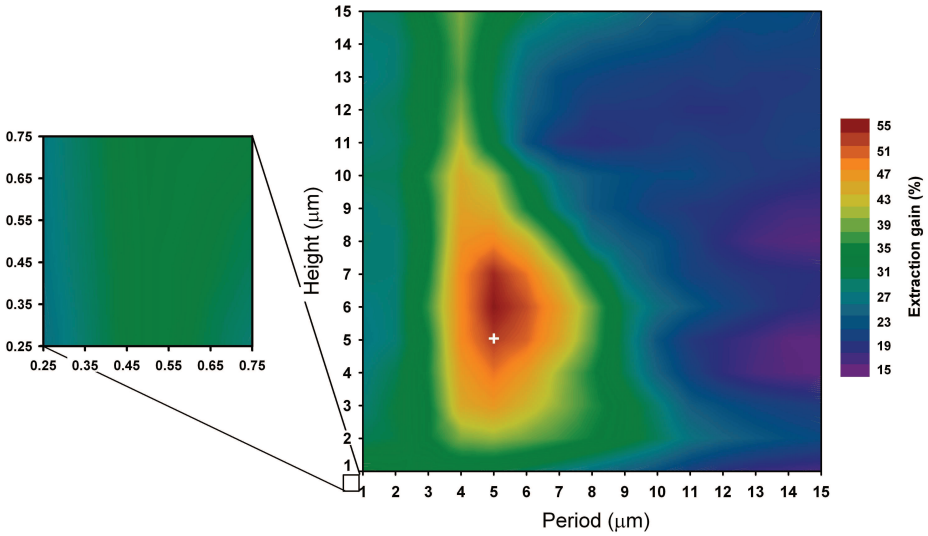

Figure 6.5: Light extraction intensity as a function of the geometrical parameters period and height of the prisms. The highest gain in LEE is shown for geometrical parameters of p=5 μm and h=6 μm. Geometrics in the submicron range do not show a particular interesting gain in LEE.

6.3 Light extraction map

As seen in the first chapter, the critical angle for the GaN-based LED is $\theta_{crit} = 23°$. Figure 6.6(a) shows the integrated light extraction intensity as a function of the incident polar angle θ and the incident azimuthal angle ϕ. One can easily see that for the plane surface, no light can be extracted over the critical angle $\theta_{crit} = 23°$. This low extraction cone leads to an extraction efficiency of $\zeta_{plane} = 3.7\%$ only. When the high-LEE geometry for the factory-roof case made of photoresist is considered, the light extraction efficiency is enhanced up to $\zeta_{struct} = 5.7\%$. In comparison to a plane surface 54% ($\Delta\zeta$) more light are extracted. In conclusion, the use of a factory-roof pattern on an add-on photoresist overlayer is theoretically even more efficient for an artificial LED than for the case of the firefly. This better improvement could be achieved by the intermediate dielectric constant of the photoresist. Table 6.2 shows that, by simply adding a 5 μm thick layer with an intermediate dielectric constant, the light extraction is already enhanced up to 16%.

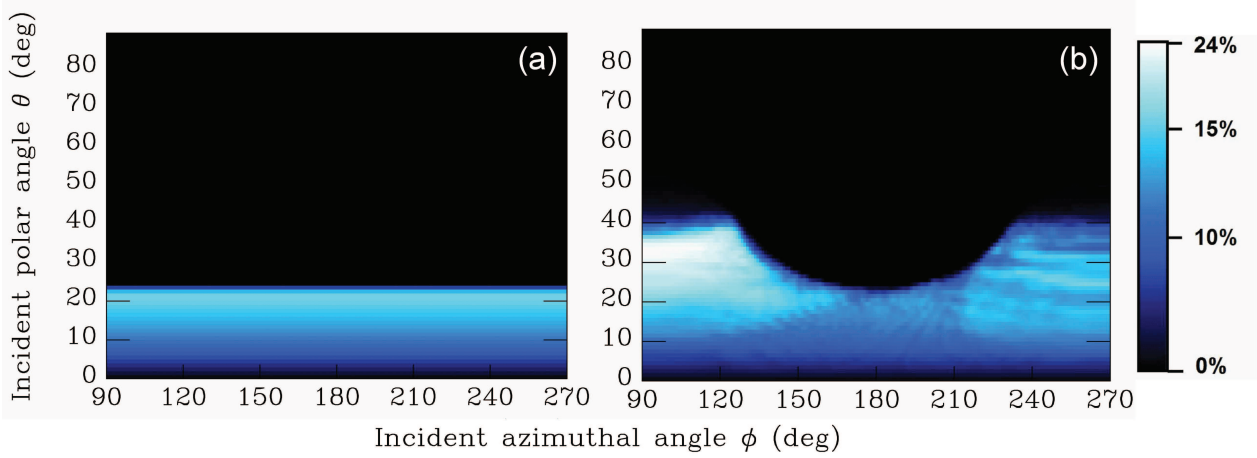

Figure 6.6: Light extraction maps, logarithmic scale. (a) Plane surface (b) Factory-roof shape.

	$\Delta\zeta$
coated patterned LED vs. bare LED	+ 54%
coated patterned LED vs. coated LED	+ 33%
coated LED vs. bare LED	+ 16%

Table 6.2: Summary of extraction gains ($\Delta\zeta$). A "bare LED" is defined as a non-treated LED. A "coated LED" is defined as a "bare LED" with a 5 μm thick photoresist layer. A "coated patterned LED" is defined as a "coated LED" where the photoresist is patterned with the specific factory-roof structure.

6.4 Direct-writing laser patterning

The factory-roof pattern with a period of 5 μm and a height of 5 μm has been fabricated on the LED described in section 6.1 with the writing strategy of the *DWL* 66 *Heidelberg* photoplotter (Fig. 6.7) by Dr. Nicolas André, on the occasion of a postdoctoral training at the University of Sherbrooke under the direction of Dr. Vincent Aimez. The manufacturing process takes five steps: (i) layout design with specific computer programs, (ii) spincoating and softbaking of the 5 μm thick overlayer made of photoresist *AZ* 9245®, (iii) sample alignment, (iv) exposure by power-modulated light and (v) photoresist development. The light source is a He-Cd laser emitting at 365 nm and is modulated into a maximum of 32 power levels by an acousto-optic modulator (AOM). Filters can be used to additionally decrease the power. At the end of the optical path an interchangeable z-movable lens focuses the beam on the resist-coated sample. In this experiment, the 10 mm writing head unit were used that gives a field depth of 10μm. The fabrication procedure was calibrated to a height of 5.2 μm for the photoresist layer from earlier tryouts. This height was then conserved for this fabrication on the GaN LED as the LEE gain only varies by 1% in comparison to a height of 6 μm. The period was fixed to 5 μm, as it gave good LEE efficiencies.

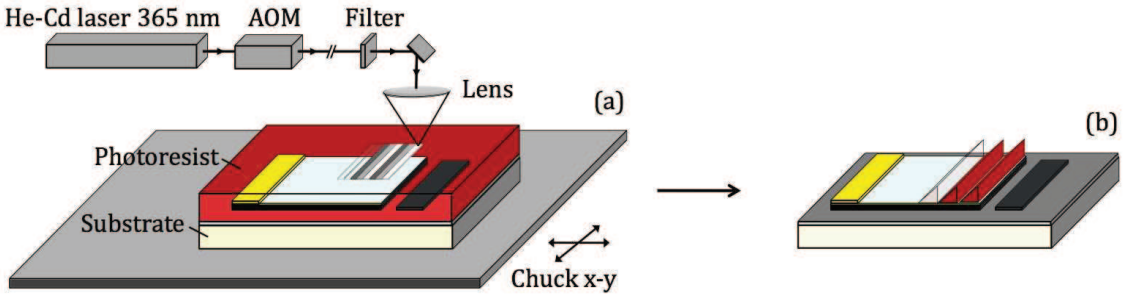

Figure 6.7: Schematic view of the *DWL* 66 *Heidelberg* photoplotter used for the direct-writing laser technique.

This technique gives a fast and easy way to verify the validity of the simulated designs on the LEE. The time-consuming laser scanning can be replaced by High Energy Beam Sensitive (HEBS) masks or resist micro-imprinting techniques, once the exposure dose and concept determined. Figure 6.8 shows the LEDs fabricated by Nicolas André at the University of Sherbrooke, Canada. Figure 6.9 (a) shows a detail of the factory-roof structure created by this technique. The tilted slope and the sharp edge are clearly visible. Figure 6.9 (b) shows the LED pad covered completely with this specific structure.

When comparing the simulated gain in LEE as a function of the height and the periods, some restrictions have to be taken into account: the period can be as long as desired, but the maximal possible height will be a function of the chosen period. The difficulty in this geometry is to obtain a neat and well defined slope in the lower area, when the period is short or the maximal height too high. The simulations have been carried out for a wider range than accessible with

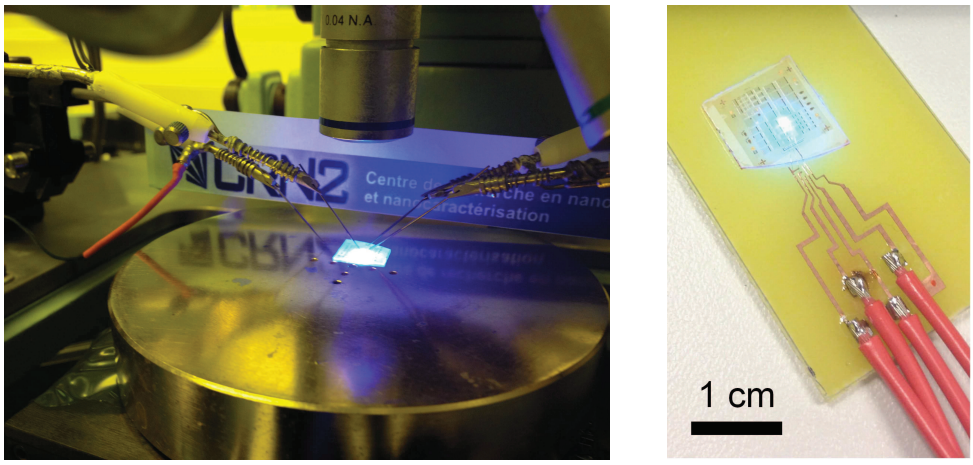

(a) (b)

Figure 6.8: Patterned LED created at the University of Sherbrooke by Nicolas André

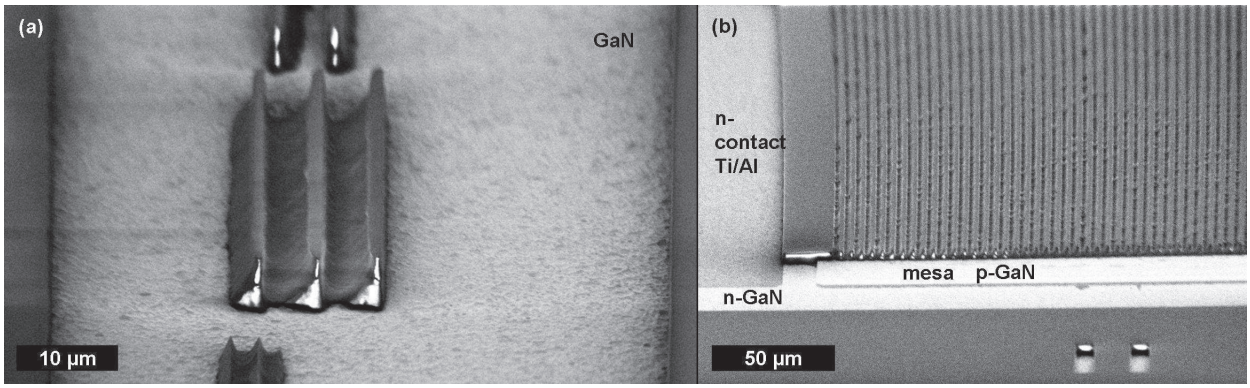

Figure 6.9: Artificial factory roof pattern on the LED. (a) Detail. (b) Whole p-GaN pad covered with the factory-roof shape.

this fabrication technique. Large aspect ratios cannot be realized and profiles higher than 15 μm can only be considered for structures with very large structures.

6.5 Optical measurements

A direct measurement of two diodes of the same type was carried out. The two diodes were fabricated on the same chip, applying a common procedure. The whole chip has been covered afterwards with photoresist. One diode -diode (A)- was laser patterned by the above described procedure (see section 6.4), whereas the other diode -diode (B)- was left flat and serves as reference. The measurement of the absolute radiance $R(\theta, \phi, \lambda)$ (Watt/m^2/sr/nm) has been carried out with the *ELDIM EZContrast XL*80*MS* scatterometer. This measurement takes into account light emitted for all polar angles θ ranging from 0° to 80° and azimuthal angles ϕ from 0° to 360°. The power supply for the diodes was set to a constant current input of 1mA. The

power density emitted by the LEDs as a function of the wavelength λ was calculated from this detailed data by integrating the radiance over a 2π solid angle using Equ. (6.1).

$$P(\lambda) = \int_0^{2\pi} d\phi \int_0^{\theta_{\max}} \sin\theta \; d\theta \; R(\theta, \phi, \lambda) \tag{6.1}$$

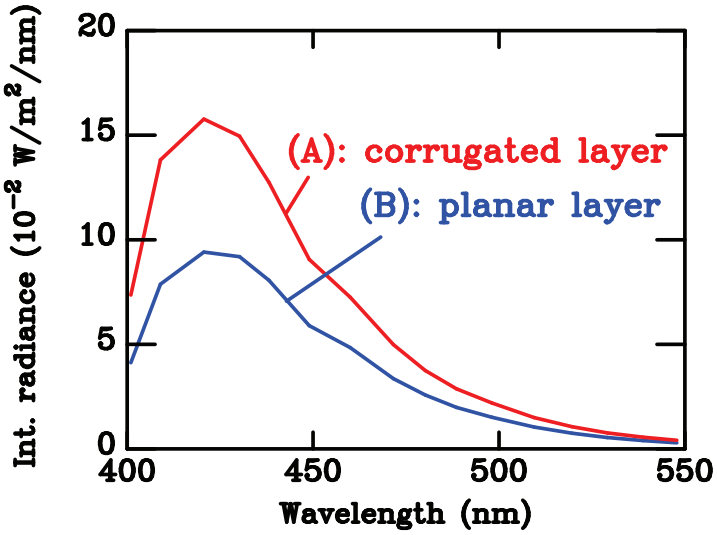

Figure 6.10: Measured radiance integrated over the hemispherical solid angle for (A) a coated and patterned LED and (B) a coated flat LED.

The radiance delivered by both diodes was measured independently. Figure 6.10 shows the integrated intensity as a function of the incident wavelength. The emission peak of both diodes is found at a wavelength close to 425 nm. The maximum emission power reaches 15.8×10^{-2}W/m^2/nm for the corrugated surface and 9.4×10^{-2}W/m^2/nm for the flat coated, reference surface. This corresponds to an increase in the light extraction enhancement of $\Delta\zeta_{meas}$=68%. This value can not be compared immediately to the simulations of section 6.2, where an increase of $\Delta\zeta_{sim}$=54% was announced. The 54% enhancement was the simulated amount of LEE for the corrugated LED in comparison to a bare (not-coated) LED. Here an LEE of 68% is achieved between a patterned LED and a uniformly coated LED. The simulated LEE between a patterned LED and a coated LED reached only $\Delta\zeta_{sim}$=33% (see Table 6.1). This discrepancy between the simulations and the mesurements should be studied more precisely and a greater number of measurements should be carried out on several LEDs to have a significant statistical dataset. Provisionally, we can try understanding the differences between these results as a fabrication artefact: the LEDs have been created on the same support under exactly the same conditions. However, the optoelectronic characteristics of the actual diodes, and the emitted light power could be slightly different. These first measurements support tendencies and confirm already the conclusions of the simulations carried out. This work will not be enough to garantee the production of new, improved diodes on an industrial ground, but simply open a new oppurtunity to engineer efficient LEDs.

6.6 Discussion

In this chapter, we saw that the light-extraction efficiency of a diode can be increased with an adapted structure inspired by the structures found on the lantern of the *Photuris* firefly. The theoretical enhancement is even higher than in the case of the firefly, as the structure is fabricated in a photoresist with an intermediate dielectric constant and specifically structured. The enhancement predicted by the simulations reaches $\Delta\zeta_{sim}$=54%. The measurements show an even better enhancement up to $\Delta\zeta_{meas}$=68%.

This result can most probably be improved even further. The current spreading layer narrows down the light extraction, as it absorbs several percents of the light before it can reach the surface. Nickel and Gold have quite high absorption coefficients which limit the light transmission. Other materials can be used in the current spreading layer to minimize losses due to absorption. Chong and Lau [115] show that the optical transmittance for an Ag(0.5nm)/ITO(100nm)[2] or a Ag(0.5nm)/ITO(5nm)/ATO(150nm)[3] current spreading layer are better than for the one based on Ni(5nm)/Au(5nm).

[2]ITO= Tin-doped Indium Oxide
[3]ATO=Antinomy-doped Tin Oxide

Conclusion

The focus of the present doctoral dissertation is the efficiency of the light extraction from an optically dense material into air. The light extraction in such a case is limited, because of the existence of a critical angle which narrows down the range of useful emission directions significantly. In the case of moderate refractive indexes such as those of organic materials, like chitin, only 20% of the light which are produced in the material are extracted through a planar surface. This limiting effect is even increased in the case of solid-state light-emitting diodes (LED), when the incident material is a semiconductor of high refractive index. Nature provides a good model for such devices, in the form of the lantern of bioluminescent terrestrial living organisms, which have to deal with the same problem and have been given at least a hundred million years to evolve efficient devices. Our approach here starts with a careful observation of the lantern structure from Central American firefly and continues with the biomimetic proposal of a new overlayer designed to improve the light extraction in a blue GaN LED.

Many examples of bioluminescent organisms are available for study and physical appreciation in terrestrial and marine environment. The terrestrial living organisms deal with just the same light-extracting limitation, as light is produced in a dense active material and in all cases needs to escape into air. It can be observed in some fireflies, for instance, that the light crosses a complex inhomogeneous material before reaching the insect's cuticle surface. Our approach to find solutions to improve the light extraction efficiency was to take a look at Lampyrids. Fireflies are known to use light for intra- and inter-specific communication. An increase in the lantern complexity can be observed, which gives a strong indication about the importance of this function for the fireflies. it is then reasonable to assume that they have benefited of millions years of evolution to optimize the light extraction from their lantern for saving energy. The important question is: what can we learn from them?

This approach, where nature is carefully observed, is slowly establishing a general and useful methodology for dealing with the most difficult part of an engineering development: the inspiration phase, at the very beginning of a useful artificial design. The injection of biological observation in an engineering endeavor is met in the present work at two distinct levels: function and mechanism. Different approaches can be made: (i) Mimicking only the function is a step which has long been known as "bionics", important for instance when dealing with the recuperation of lost biological human functions, such as vision or motivity, by artificial prosthesis using mechanisms provided by well-established technology. (ii) Recognizing a useful physical mechanism on the structure of some living organism and adding it to the list of available

technologies, with no regard of the original biological function, is usually referred to as "bio-inspiration". (iii) When the original function and the physical mechanism are both translated into some useful engineering work, this is the field of "biomimetics". Our approach in this thesis is clearly biomimetic: the lantern of the firefly is analyzed to learn about structures that enhances the light extraction efficiency (LEE) in the firefly and these structures are then applied to an LED to improve in turn its LEE.

Why should biology provide a meaningful answer to an engineering question? Evolution and natural selection, in the framework of biomimicry, can be viewed as a powerful optimization algorithm: living organisms reproduce with changes induced by random mutations in the genome of some individuals. These changes can be beneficial if they favor, for instance, the rate of reproduction or the protection against predators. In that case, the population issued from the modified species increases, sometimes much more than the unmodified offspring, that may be bound to extinction. If a function such as producing light is very important for the species dominance, any "technological" improvement may be positively selected and it is not surprising that – after several 10s or hundreds million years of biological evolution – the light-emitting device has reached a significant optimization state, worth being examined for biomimetic uses. Some warnings should however be underlined: First, a given structure usually has several functions. A butterfly scale, for example, is primarily designed as a part of the locomotion organ and has an influence on the insect's ability to fly. Also, it can be useful for escaping spider's webs, protecting against parasites, absorbing light for heat generation, repelling water and dust, and so on, before being used to reflect or scatter light for coloration and inter-/intraspecific communication. The biological optimization process is more global, with all these perfectible targets in view, weighted by the importance of the functions for sustaining a species population. A biomimetic development does not only require a good understanding of the physical mechanism revealed, but also a good understanding of its biological function and its dominant influence on the species population growth. Second, the natural device, when adapting better to their environment, can grow in complexity, to the point where the artificial fabrication of a faithful biomimetic copy becomes impossible. This is when the practice of a "theoretical" physicists can be useful: understanding the various substructures and their contribution to the global objectives may help identifying the most efficient one and consider its re-optimization. This was done in the present thesis for one substructure of the firefly's lantern: the jagged scales surfaces, which was selected as a starting point to our biomimetic work.

The light propagation through the different optical substructures that separates the photocytes from the air of the bioluminescent organ from a Panamanian firefly has been analyzed. A throughout analysis by optical microscopy, electronic microscopy and X-ray nanotomography of the bioluminescent organ was carried out. The scales on the cuticle of the firefly are jagged so that they form a prism shaped structure referred to as a "factory roof" in this work. The period of this structure was measured to be 10 μm with a height at the sharp edge of 3 μm. The simulation show that, due to this roughness the light extraction is enhanced from 20% for a plane interface to 29% for this specific jagged scale interface. The LEE enhancement is 45%. The light is scattered on the sharp edges and new paths open up due to the tilted slope geometry in

comparison to a plane surface. A study on the geometrical parameters of the factory-roof shape was carried out to figure out the optimal structure of the pattern. The structure found on the firefly abdomen was close to the optimal parameters. As mentioned above, nature has to deal with multioptimization instead on concentrating on one single property, e.g. light extraction. Another difficulty is that the firefly bends its abdomen, when flashing, and this could slightly change the geometry of the rather large prisms, optimizing the structure seen on the dried, dead specimens.

The computational analysis of a two-dimensional, symmetric triangular structure was also carried out. It showed a lower extraction efficiency than the asymmetric firefly shape. The wedge of the triangular structure is less sharp than in the firefly case, where scattering is probably smaller. Moreover the symmetric arrangement of the tilted slopes gives less possibilities for the light rays to escape from the incident material, from a basic optical geometry point of view, in comparison to the asymmetric factory-roof shape found on the firefly. The three-dimensional pyramid structure gives similar light extraction efficiencies as the firefly shape, for the optimal geometries. However, the optimal structure is much smaller than in the firefly case (p=3 μm - h=2 μm and p=8 μm - h=7 μm, respectively). Moreover the range of high LEE values is smaller than in the two-dimensional cases and decays much more rapidly to uninteresting values close to the LEE of a plane interface. This gives a lesser flexibility for fabrication than in the two-dimensional cases. Moreover the patterning technique used in this work, i.e. laser patterning, is well adapted to two-dimensional shapes, but more complicated in three dimensions. Therefore, the structure that was considered for fabrication on an LED was chosen to be the asymmetric factory-roof shape inspired by the firefly.

The LED's active material is GaN with a higher refractive index than chitin. The current spreading layer over the GaN LED is constituted of nickel and gold and the structure has been patterned in photoresist. With these new refractive indexes, the model has to be adapted to simulate the optimal geometry to be applied on the LED. The light extraction efficiency as a function of the period and the height has been studied and one structure has been chosen to fit both, high LEE and feasibility in fabrication. The period and the height were fixed both to 5μm. The light extraction efficiency with this geometry is enhanced and the gain reaches 54%. The fabrication of this structure has been carried out by Dr. Nicolas André, then postdoctoral researcher at the Univeristy of Sherbrooke, Canada and now researcher at the University of Louvain-la-Neuve. The measurement showed an even higher increase in the LEE than expected, which confirmed that the specific structure helps the light to escape the active material of the LED.

The light extraction here is somewhat smaller than compared to some techniques described in the first chapter. Yablonovitch described already in 1993 a 50% increase [48], but only for a very high material quality. By adding a microlens-array on a glass substrate Park *et al.* described an LEE increase of 121%. In this technique the LED is not directly patterned itself, as a glass lens is added. More material includes higher costs. Lysak *et al.* announce an increase of 54% by embedding a 3D air-conical structure in the active material [56]. The increase is considerable but the fabrication process of the LED needs to be changed. Wu *et al.* increased

the LEE by 91% [57] using surface nanostrucuring by focus ion beam. This fabrication technique is very slow and can therefore only be applied to small areas. Zuo *et al.* describe an 83.5% LEE increase for large-scale elliptical stripes [59]. The enhancement is high for this large-scale pattern, but shows a strong angular dependence.

In comparison to these values, the LEE enhancement of the structure described in the present work seems to be somewhat low, but the overall design show several advantages: (i) Once the exposure dose and the concept determined, the time-consuming laser scanning can be replaced by high energy beam sensitive masks. By that mean, the fabrication of the structure can be applied to large scale processes. (ii) The described structure has been fabricated in a photoresist layer which can be added on any existing LED. This gives a good flexibility for the fabrication process. (iii) The large-scale, two-dimensional pattern is easier to fabricate and does not need a very high precision. The measurement performed on the LED's showed even better results than the theoretical predictions due probably to additional roughness in the resist. This latter advantage seems to be the most important and the most interesting. Nature taught us to consider a micrometric, two-dimensional and asymmetric structure, rather than a complex and smaller three-dimensional photonic crystal or random corrugation as considered by several works described in the first chapter (section 1.2).

The proposed design of the patterned LED can be optimized even more. The current-spreading layer made of nickel and gold absorbs a high percentage of the passing light. To improve the LEE, another, less absorbing material could be used, such as Ag/ITO .

The use of LEDs for lighting and displays is clearly an important objective, in a context that calls for the moderation of the global energy consumption. Furthermore, LED illumination provides many benefits not related to energy saving: an extremely long life (provided obsolescence is not programmed) which leads to less maintenance work and costs; no use of materials, toxic or harmful to the environment; high resistance to vibration, shock and rough climatic conditions; zero ultraviolet emission; high flexibility for controlled illumination intensity, color and direction; high reliability even in low temperature conditions; very fast on and off switching; operation from low voltage... All these reasons justify phasing out traditional light sources and replace them by electroluminescent devices in most applications. In this favorable context, every external efficiency improvement – even modest – is extremely important.

Materials and Methods

A. Collection of samples and taxonomic determination

Photuris sp.

The *Photuris* sp. fireflies were collected in the Darien forest at the Cana field station, close to the Columbian border, in the Republic of Panama. The collection started at 9pm on a clear moonless night in early May 2009 and the fireflies were found on a grassy open space and on the bordering trees. The specimens were collected by the following procedure: First, locate a firefly signaling in the grass. Then wait until the firefly flashes a second, third time at the exact same spot. Light up the intended spot and catch the firefly by hand.

Figure I: *Photuris* firefly collected in Panama.

The taxonomic determination was attempted by comparing the collected specimens with those kept in museum collections. The subfamily Photurinae and the genus *Photuris* (LeConte, 1981) could be determined by examining the section of Lampyridae from the Royal Belgian Institute of Natural Sciences and the National Natural History Museum of the Smithsonian Institution (Washington D.C.).

Aspisoma ignitum

This species was collected on Guadeloupe, an island of the Lesser Antilles. About 20 specimens were collected in one spot called "Le Moule" on a meadow close to the sea in January 2011. The fireflies were safely brought to Belgium and could be kept alive for several weeks in the laboratory. The collection procedure was the same as described for the *Photuris* case. A well-

known local entomologist, Fortuné Chalumeau, gave helpful indications for the identification of this firefly species.

Figure II: *Aspisoma ignitum* firefly collected in the Lesser Antilles.

Lamprohiza splendidula

The specimens of this species were collected at several spots in Belgium during warm summer evenings in 2012. At "l'Abbaye de Maredret" close to Dinant they were particularly abundant and about 15 specimens could be collected in one hour. The collection procedure was the same as described for the *Photuris* case. The taxonomic identification of these fireflies was carried out by examining the section of Lampyridae from the Royal Museum of Natural History in Brussels and the help of local entomologists. These specimens were, as well, kept alive in the laboratory, but only survived for a few days.

Figure III: *Lamprohiza splendidula* firefly. (Credit: Ondrej Zicha, BioLib.cz.)

Taxonomy and phylogenic relationships

All the species included in the Lampyridae family does, at some stage in their life cycle, emit light. All known larvaes of this family produce a faint glow in their bioluminescent organ located on the eight segment. The bioluminescence in the larvae stade of the Lampyrids seems to originate from an early cantharoid ancestor.

The three species of fireflies described above all belong to the LAMPYRIDAE family. The *Aspisoma* and *Lamprohiza* genus has been included in the Lampyrinae subfamily, whereas the *Photuris* genus has been included in the Photurinae subfamily.

The phylogenic relationships[4] (Fig. IV) show that the studied fireflies are not closely related to each other. The genus closest to *Photuris* is *Bicenollycha* and it would be interesting to see if this species has morphological structures similar to those found on *Photuris*. Morphological differences on and in the bioluminescent organ of these three genus have been found. No direct conclusions can be drawn from these observations and from the position in this phylogenetic tree. The phylogenetic relationships indicate that geography is not a good predictor of phylogeny [116], which means, that even these three species from very diverse locations could be more closely related than expected.

It should be noted, that the bioluminescence in the larval state is only a faint glow. By contrast, the bioluminescence in the adult vary greatly by its absence, presence, location, shape and use [117].

[4]Based on a likelihood analysis and a Bayesian analysis on two data sets (collected North American fireflies and worldwide dataset).

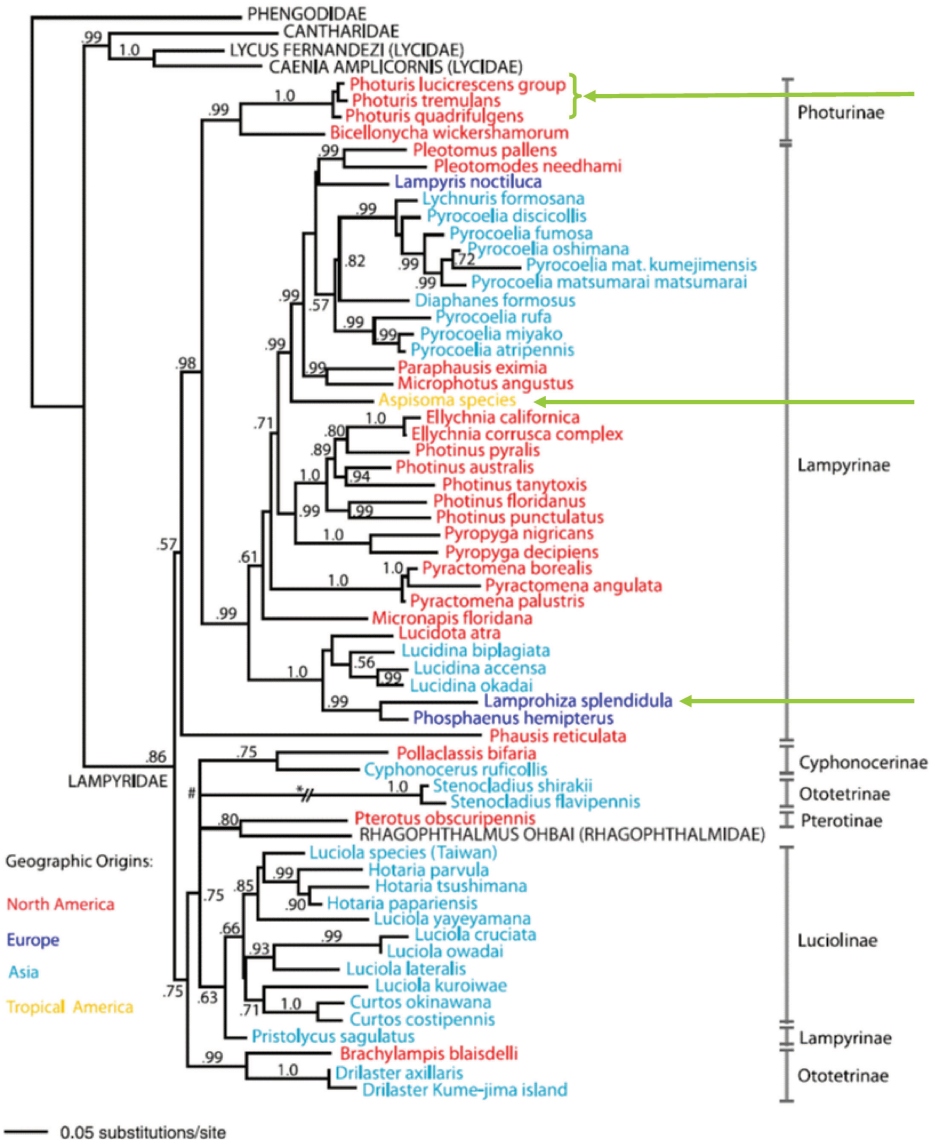

Figure IV: Phylogenic relationships of North American, tropical American, European and Asian firefly species. (Credit Stanger-Hall *et al.* [116]). The green arrows indicate the species cited in this work.

B. *Avantes Avaspec* 2048 spectrometer

The emission spectra were measured with an *Avantes Avaspec* 2048 optics fiber spectrometer. The detector is a 2048 pixels CCD array. The spectrometer is composed of a collimating and focusing mirror and a diffractional grating (Czerny-Turner monochromator). It is especially suitable for low light level and high resolution applications. The spectral range covers wavelengths from 200 nm to 1100 nm and is therefore perfectly adapted to locate the emission peak of the firefly bioluminescence.

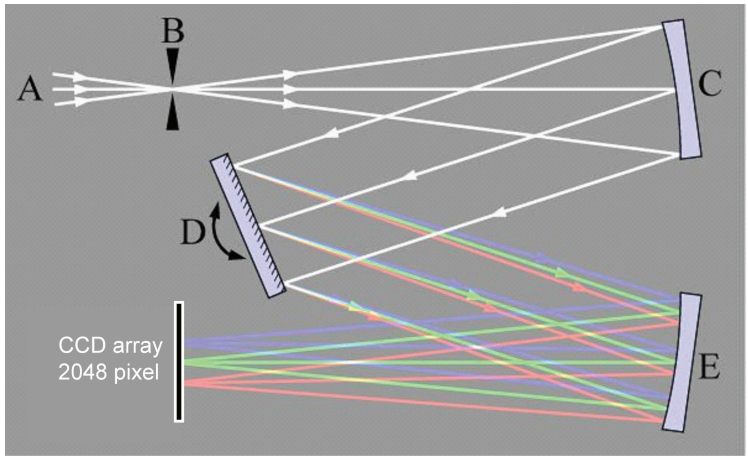

Figure V: Diagram of the Czerny-Turner monochromator.

For the measurement we used the optical fibers with a probe head. The diameter of these optical fibers is 200 μm. Some fireflies were stabilized with double-faced adhesive tape on their back. Several specimens stopped to emit bioluminescence when put in this unusual position. Another technique to measure the light emission of the fireflies was to confine them in a net, put the probe head of the spectrometer optical fiber through the net and follow the fireflies in their walking movement. This second technique gave good spectra which helped to determine the spectral distribution of the emission of two firefly species.

C. Scanning Electron Microscope (SEM)

Different samples were analyzed: (i) the whole insect was put under the beam to analyze the surface of the segments above the bioluminescent organs (Fig VI). (ii) The specimens were cut open in different ways to analyze the interior of the bioluminescent organ. To avoid destroying, quenching or displacement of the interesting structures, the samples were put for 1 min. in liquid nitrogen, as well as the knives and the squeezers, before cutting the bioluminescent segments.

Most of the samples were coated with a layer of gold to ease charge elimination. This gold layer was achieved by gold sputtering with argon ions. The mean thickness was close to 25 nm.

Two scanning electron microscopes were used: a low-resolution Philips XL20 and a high resolution field effect SEM JEOL 7500F. The observation conditions varied strongly with the nature of the sample (coated or not, whole insect or piece,...). The voltage was selected from 1 kV, in the "gentle beam" mode to 20 kV under normal observation conditions. The current was set to 20 mA. In the "gentle beam" mode – a high bias voltage is applied to the specimen stage – the electrons are decelerating before touching the samples surface, which enables high-resolution observations at low voltages. Low voltages enables the observation of low conducting samples by reducing the beam penetration and charge buildup.

The resolution announced by the technical data sheet of the JEOL 7500F is 1.0 nm at 15 kV, 1.4 nm at 1 kV (Gentle beam mode) and 2.0 nm a 1 kV (SEM mode). This resolution can be achieved under ideal observation conditions, which means an ultra high vacuum, a perfectly conductive sample, stable emission by the filament and a perfectly aligned beam.

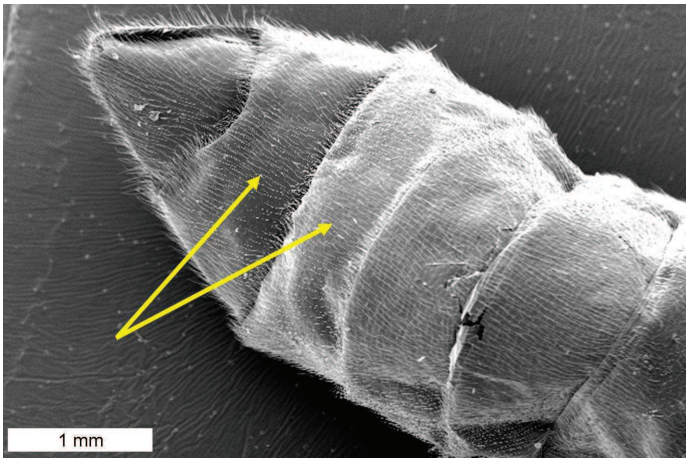

Figure VI: SEM image of the *Photuris* firefly abdomen. Ventral side. The two bioluminescent organs are located in the 5th and 6th segment.

D. Hard X-ray Nanotomography at the European Synchrotron Radiation facility (ESRF)

The experiment was carried out at the Nano-imaging beamline (*ID22NI*) in collaboration with Dr. Peter Cloetens, Scientist in charge on *ID22NI*, and Dr. Heikki Suhonen, Junior scientist at *ID22NI*.

Sample preparation

The aim of this experiment was to analyze the spheres arrangement in the fireflies bioluminescent organ. The bioluminescent organ was scanned in three-dimensions and it was not needed to open the organ to be able to analyze the interior, which represents a huge advantage in comparison to the electron microscope. However, to enhance the resolution as much as possible non-necessary organic material was eliminated. The dorsal side of the abdomen was cut off and the interior was carefully cleared.

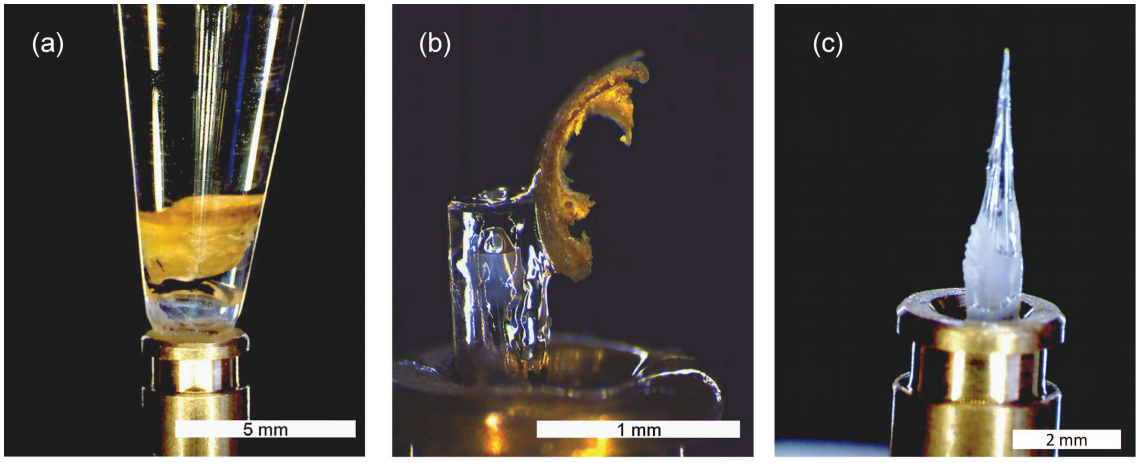

Figure VII: Samples prepared for the experiment at the ESRF. (a) Abdomen of the firefly enclosed in resist. (b) Cleared bioluminescent segment fixed to the sample holder with glue. (c) A capillary tube used as sample holder for the photocyte cells.

Several samples were put beforehand in polyepoxide resist (epoxy), commonly used in electron microscopy, to stabilize the sample spatially and to reduce the refractive index contrast in the analyzed zone (Fig. VII(a)). The epoxy resist has a high penetration and can eliminate residual air in the bioluminescent organ of the firefly. The refractive index of this resist is close to chitin. Strong refractive index contrasts in the analyzed region can diminish the resolution of the three-dimensional reconstruction. Other samples were slightly prepared by clearing out uninteresting organic material and simply fixed to the sample holder using commercial available instant adhesive (Fig. VII(b)). The sample shown on Fig. VII(c) represents a capillary tube where several photocyte cells were glued on.

Holotomography or quantitative phase tomography

X-ray wavefronts are sensitive to variations in electron density when passing through a volume. For X-rays, the real part of the refractive index is very close to 1 (the deviation is less than 10^{-5}). In the so-called propagation mode, images are acquired at different sample-detector distances D. The images taken at small sample-detector D ($\sim$1 cm) distances are dominated by absorption contrast, while the images taken at large D ($\sim$1 m) are dominated by phase contrast [118].

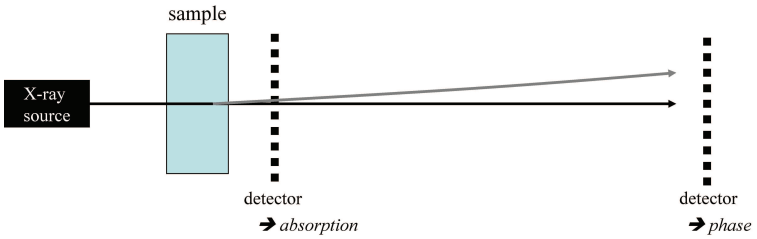

Figure VIII: Holotomographic X-ray nanotomography. Schematic representation.

The optical phase of an X-ray beam is affected when transmitted through an object. For a spatially coherent beam, Fresnel diffraction provides phase images for the analyzed object. The acquisition is made at different sample-detector distances D to avoid the Talbot effect: a periodic phase object with a period b produces no contrast at sample-detector distance

$$D = p\frac{a^2}{\lambda}$$

λ being the wavelength, p an integer.

Fresnel imaging at one single distance can therefore not detect all spatial frequencies in the phase distribution. Dr. Peter Cloetens and his team developed a holographic reconstruction procedure to extricate the phase maps from such images taken at several distances [119]. The beam is a coherent hard X-ray beam at of 28.9 keV ($\lambda \approx 0.4$ Å). The very small variations in the propagation direction of the beam create visible intensity variations for a propagation after the sample of the order of 1 m. The transmission function F that characterizes the object is described as follows:

$$u(x, y) = F(x, y)u_0(x, y)$$

u and u_0 being the field just downstream and upstream of the object, respectively, at the point (x,y) of the object plane. F contains the real and imaginary part of the refraction index.

$$F(\overrightarrow{x}) = \mathrm{e}^{i\varphi(\overrightarrow{x})}$$

$$F(x, y) = M(x, y)\ \mathrm{e}^{i\varphi(x,y)}$$

The absorption M and the phase modulation φ are expressed as

$$M(x,y) = \exp\left(-\frac{1}{2}\int \mu(x,y,z)\,\mathrm{d}z\right)$$

$$\varphi(x,y) = \frac{2\pi}{\lambda}\int (n(x,y,z)-1)\,\mathrm{d}z$$

The integrals represent the absorption M and the phase modulation φ along the propagation direction (z axis). μ being the linear absorption coefficient and n being the real part of the refractive index. The Fourier transform of the intensity $I(x)$ from a non-absorbing sample, which is supposed to be the case for the firefly, is expressed for one dimension as:

$$\tilde{I}_m(f) = \delta(f) + 2\sin(\pi\lambda D f^2)\tilde{\varphi}(f)$$

if

$$|\varphi(x) - \varphi(x-\lambda D f)| \ll 1$$

$\tilde{I}(f)$ and $\tilde{\varphi}(f)$ being the Fourier transform of the intensity $I(x)$ and the phase modulation $\varphi(f)$ for a spatial frequency f, respectively [120].

The Fourier transform of the intensity distribution at the distance D_m (m=1-4) is expressed as follows in the three-dimensional case [119]:

$$\tilde{I}_m(\mathbf{f}) = \delta_D(\mathbf{f}) + \tilde{R}_m(\mathbf{f})\ 2\ \sin(\pi\lambda D_m(\mathbf{f})^2)\ \tilde{\varphi}(\mathbf{f})$$

if

$$|\varphi(\mathbf{s}+\lambda D_m\mathbf{f}) - \varphi(\mathbf{s}))| \ll 1$$

$\delta_D(\mathbf{f})$ is the Dirac distribution and corresponds to the unit mean intensity. The multiplicative factor $\tilde{R}_m(\mathbf{f})$ includes the detector transfer function and the degree of spatial coherence in the object plane.

The images at several distances are then combined and a least-square approach leads to a unique initial estimate:

$$H(\mathbf{f})\tilde{\varphi}(\mathbf{f}) = \frac{1}{4}\sum_{m=1}^{4} H_m(\mathbf{f})\tilde{I}_m^{exp}(\mathbf{f})$$

where

$$H_m(\mathbf{f}) = \tilde{R}_m(\mathbf{f})\ \sin(\pi\lambda D_m\mathbf{f}^2)$$

and

$$H(\mathbf{f}) = \frac{1}{4}\sum_{m=1}^{4} \tilde{R}_m^2(\mathbf{f})2\ \sin^2(\pi\lambda D_m\mathbf{f}^2)$$

This estimate has then to be optimized based on the Fresnel diffraction approximation, efficiently implemented at the ESRF using fast Fourier transforms. When these phase maps are obtained, all the maps corresponding to different orientations of the sample are brought together to form a tomographic reconstruction.

These maps were measured considering four distances. At each distance, 1500 orientations of the sample were measured. This technique is quite time-consuming and a full scan analyzing three different resolutions took about six hours.

The tomographic reconstruction from the phase maps is done with the PyHST software based on the filtered backprojection algorithm [121].

Experiment

The sample was put in the X-ray beam and the resulting signal is recorded behind the sample by a CCD detector containing 2048×2048 pixels. This recording is repeated for 1500 angular position over the whole 360° range. Four distances for each desired resolution were acquired.

All the analyzed samples appeared to be stable in the X-ray beam during the acquisition time and no damage was visible. The analysis was carried out at several resolutions for each sample. Table 6.6 shows the available resolutions and the average corresponding size of the scanned region. The smallest resolution, i.e. the largest scanned region, is important to be able to locate correctly the interesting zone. The scans at higher resolutions were well adapted to analyze the distribution of the spheres in the bioluminescent organ.

Pixel size	Scanned region
30nm	$60\times60\times60\mu\text{m}^3$
50nm	$100\times100\times100\mu\text{m}^3$
100nm	$200\times200\times200\mu\text{m}^3$
300nm	$600\times600\times600\mu\text{m}^3$

Visualization

The visualization and analyze of the images was not convenient, as the files are very heavy. One full reconstruction (2048×2048×2048 pixels) consists of 8GB which is divided in 8 slices of 1 GB (2048×2048×256 pixels). *Image J* is an user-friendly tool to make the first analyze of the slices. For a more precise study the three-dimensional visualization and analysis program *VGStudio MAX 2.1* was used.

E. Calculation of the optical reflectance and the optical transmittance using the scattering matrix algorithm

In this section we describe the transmission of electromagnetic energy through a inhomogeneous layer, based on the paper published by Bay et Vigneron [122]. The reflectance and transmittance calculation of an inhomogeneous dielectric layer is simple in the case, where the refractive index varies only in the direction of the layer thickness and is invariant in the direction parallel of the layer interfaces. When the refractive index varies also in the plane parallel to the layer interfaces, diffraction can take place. An incident light ray could be split in a large number of diffracted directions; which, in turn, can be multiplied by the diffraction of the inhomogeneous film. The main difficulty of the diffraction description by a inhomogeneous layer is this multiplication of propagations directions.

One simplification can be made when the lateral inhomogeneity is periodic, i.e. when the lateral inhomogeneity stays invariant in terms of a `Bravais lattice`. The periodicity simplifies the form of the lateral electromagnetic wave, using the `Bloch's theorem`, and introduces the concept of diffraction orders. The diffraction orders allow for a naming of the beams and their directions. This approach was introduced by Sir John B. Pendry in 1974 to evaluate the intensity of electron beams diffracted by a crystalline surface [123]. Later on, Pendry noticed, that this reasoning could be extended to electromagnetism. He provided a method to calculate the reflectance of photonic crystal surfaces in the direct lattice [124].

The approach described here is developed in the reciprocal lattice, which is better adapted to the definition of `plane waves`. In literature, the three-dimensional case has already been object of a publication [93]. Therefore, this section describes the two-dimensional case, used in the present work for simulations.

Symmetry of the diffracting system

Let's consider a system with a total translational invariance along the x-axis, a periodicity b along the y-axis and no symmetrical restraint along the z-axis (see Fig. IX).
The electromagnetic waves in this medium can be described as:

$$\overrightarrow{E}\left(\overrightarrow{r},t\right)=\sum_{m=-\infty}^{+\infty}\left\{E_{x,m}\left(z\right)\overrightarrow{e_x}+E_{y,m}\left(z\right)\overrightarrow{e_y}+E_{z,m}\left(z\right)\overrightarrow{e_z}\right\}e^{i\left(k_y+m\frac{2\pi}{b}\right)y}e^{i(k_x x-\omega t)} \tag{6.2}$$

$$\overrightarrow{H}\left(\overrightarrow{r},t\right)=\sum_{m=-\infty}^{+\infty}\left\{H_{x,m}\left(z\right)\overrightarrow{e_x}+H_{y,m}\left(z\right)\overrightarrow{e_y}+H_{z,m}\left(z\right)\overrightarrow{e_z}\right\}e^{i\left(k_y+m\frac{2\pi}{b}\right)y}e^{i(k_x x-\omega t)} \tag{6.3}$$

ω being the frequency. A free wave is propagated in the x-direction and a `Bloch wave` in the y-direction.

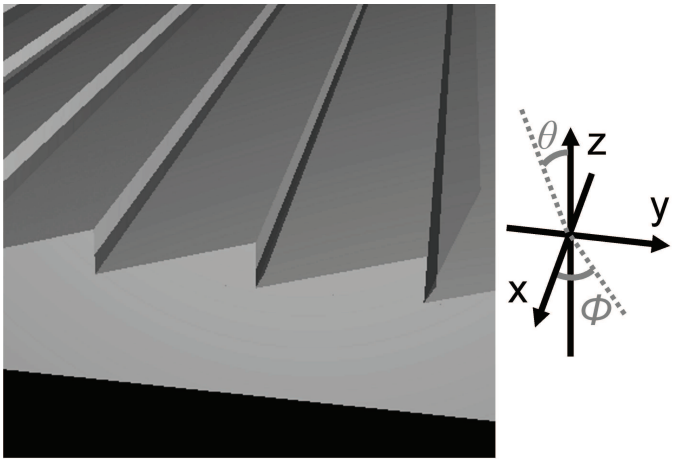

Figure IX: Two-dimensional photonic structure. This structure has a total invariance along the x-axis, a periodicity (b) along the y-axis.

The periodic part of the Bloch waves is developed in Fourier series using the Cartesian coordinate system. k_x and k_y being the lateral component, i.e. parallel to the layer, of the incident wave vector and are expressed as:

$$k_x = \varepsilon_i \frac{\omega}{c} \sin\theta \cos\phi$$

$$k_y = \varepsilon_i \frac{\omega}{c} \sin\theta \sin\phi$$

θ being the incident polar angle and ϕ being the incident azimuthal angle (see Fig IX).

The component k_y is maintained in a Bloch wave and belongs to the first `Brillouin zone`. However, k_y is associated to the y component of the incident wave vector and therefore conserved except for a reciprocal lattice vector

$$g = m\frac{2\pi}{b}$$

The dielectric constant does not vary with the x-coordinate (see Fig. IX):

$$\varepsilon = \varepsilon(y, z)$$

To make the dielectric constant ε independent of the z-axis, the system is sliced in thin films, where ε can be considered as independent of z (see Fig. X).

$$\varepsilon = \varepsilon(y)$$

The dielectric constant ε has a periodicity b in the y-axis and can be expressed as a Fourier series:

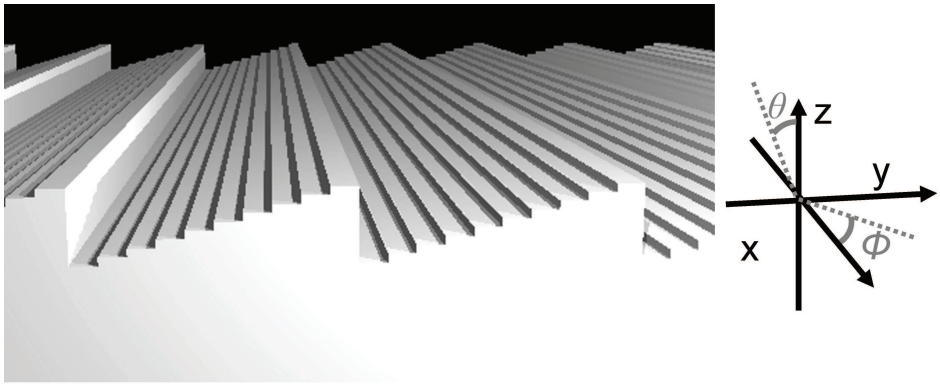

Figure X: Approximation of the dielectric constant using sublayers with fixed dielectric constant ε.

$$\varepsilon(y) = \sum_{m=-\infty}^{+\infty} \varepsilon_m e^{i\left(m\frac{2\pi}{b}\right)y}$$

The inverse of the dielectric constant is expressed as a Fourier series as well:

$$\frac{1}{\varepsilon(y)} = \sum_{m=-\infty}^{+\infty} \left(\frac{1}{\varepsilon}\right)_m e^{im\frac{2\pi}{b}y}$$

Equ. (6.2) and (6.3) narrow down the information which needs to be calculated to six series of coefficients, function only of the normal coordinate z:

$$E_{x,m}(z),\ E_{y,m}(z),\ E_{z,m}(z),\ H_{x,m}(z),\ H_{y,m}(z),\ H_{z,m}(z)$$

Integration of Maxwell's equation

Maxwell's equation can be written as a first order system of ordinary differential equations with constant coefficients using Maxwell-Faraday's equation and Ampere's circuital law ("rotational laws") and expressing the electric field $\overrightarrow{E}$ and the magnetic field $\overrightarrow{H}$ by Equ. (6.2) and (6.3). Gauss's law and Gauss's law for magnetism ("divergence laws") are redundant.

$$\frac{dE_{x,m}}{dz} = ik_x E_{z,m} + i\mu_0\omega H_{y,m} \tag{6.4}$$

$$\frac{dE_{y,m}}{dz} = i\left(k_y + m\frac{2\pi}{b}\right)E_{z,m} - i\mu_0\omega H_{x,m} \tag{6.5}$$

$$H_{z,m} = \frac{1}{\mu_0\omega}\left[k_x E_{y,m} - (k_y + g_y)E_{x,m}\right] \tag{6.6}$$

$$\frac{dH_{x,m}}{dz} = ik_x H_{z,m} - i\varepsilon_0\omega\sum_{m'}\varepsilon_{m-m'}E_{y,m'} \tag{6.7}$$

$$\frac{dH_{y,m}}{dz} = i\left(k_y + m\frac{2\pi}{b}\right)H_{z,m} + i\varepsilon_0\omega\sum_{m'}\varepsilon_{m-m'}E_{x,m'} \tag{6.8}$$

$$E_{z,m} = \frac{1}{\varepsilon_0\omega}\sum_{m'}\left(\frac{1}{\varepsilon}\right)_{m-m'}\left[\left(k_y + m'\frac{2\pi}{b}\right)H_{x,m'} - k_x H_{y,m'}\right] \tag{6.9}$$

Using Equ. (6.6) and (6.9) the longitudinal components of the fields $H_{z,m}$ and $E_{z,m}$ can be removed by expressing them as a function of the other components. The differential system is reduced to four series of equations and the transverse components of the field $E_{x,m}(z)$, $E_{y,m}(z)$, $H_{x,m}(z)$, $H_{y,m}(z)$ can be calculated. These components are grouped in a vector, such that:

$$\bar{F}_m(z) = \begin{pmatrix} E_{x,m}(z) \\ E_{y,m}(z) \\ H_{x,m}(z) \\ H_{y,m}(z) \end{pmatrix} \tag{6.10}$$

and Maxwells equations are expressed as

$$\frac{d\bar{F}_m(z)}{dz} = \sum_{m'=-\infty}^{+\infty} G_{m,m'}\bar{F}_{m'}(z)$$

$G_{m,m'}$ being 4-by-4 matrices having an effect on the above defined "four-vector" $\bar{F_m}(z)$.

$$G_{m,m'} = \begin{pmatrix} 0 & 0 & [A_{xx}]_{m,m'} & [A_{xy}]_{m,m'} \\ 0 & 0 & [A_{yx}]_{m,m'} & [A_{yy}]_{m,m'} \\ [B_{xx}]_{m,m'} & [B_{xy}]_{m,m'} & 0 & 0 \\ [B_{yx}]_{m,m'} & [B_{yy}]_{m,m'} & 0 & 0 \end{pmatrix}$$

The non-zero elements of this matrix can be expressed as

$$[A_{xx}]_{m,m'} = \frac{i}{\varepsilon_0\omega}k_x\left(\frac{1}{\varepsilon}\right)_{m-m'}\left(k_y + m'\frac{2\pi}{b}\right)$$

$$[A_{yx}]_{m,m'} = i\mu_0\omega\delta_{m,m'} - \frac{i}{\varepsilon_0\omega}k_x\left(\frac{1}{\varepsilon}\right)_{m-m'}k_x$$

$$[A_{xy}]_{m,m'} = -i\mu_0\omega\delta_{m,m'} + \frac{i}{\varepsilon_0\omega}\left(k_y + m\frac{2\pi}{b}\right)\left(\frac{1}{\varepsilon}\right)_{m-m'}\left(k_y + m'\frac{2\pi}{b}\right)$$

$$[A_{yy}]_{m,m'} = -\frac{i}{\varepsilon_0\omega}\left(k_y + m\frac{2\pi}{b}\right)\left(\frac{1}{\varepsilon}\right)_{m-m'}k_x$$

$$[B_{xx}]_{m,m'} = -\frac{i}{\mu_0\omega}k_x\delta_{m,m'}\left(k_y + m'\frac{2\pi}{b}\right)$$

$$[B_{yx}]_{m,m'} = -\frac{i}{\mu_0\omega}\left(k_y + m\frac{2\pi}{b}\right)\delta_{m,m'}\left(k_y + m'\frac{2\pi}{b}\right) + i\varepsilon_0\omega\varepsilon_{m-m'}$$

$$[B_{xy}]_{m,m'} = \frac{i}{\mu_0\omega}k_x\delta_{m,m'}k_x - i\varepsilon_0\omega\varepsilon_{m-m'}$$

$$[B_{yy}]_{m,m'} = \frac{i}{\mu_0\omega}\left(k_y + m\frac{2\pi}{b}\right)\delta_{m,m'}k_x$$

On the basis of these expressions, we can define a "supervector" $\bar{\bar{F}}(z)$ which contains all the diffraction orders and the matrix G, such that the elements of G are the 4-by-4 matrices $G_{m,m'}$ respectively.

$$\bar{\bar{F}}(z) = \begin{pmatrix} \cdots \\ \bar{F}_{-1}(z) \\ \bar{F}_0(z) \\ \bar{F}_1(z) \\ \cdots \end{pmatrix} \tag{6.11}$$

Maxwell's equations can then be written as:

$$\frac{d\bar{\bar{F}}(z)}{dz} = G\bar{\bar{F}}(z) \tag{6.12}$$

G being an infinite matrix of 4-by-4 blocs, that contain constant elements, i.e. independent of z. The equation system (6.11) can be integrated analytically using the exponential function of a matrix. If we admit the solution of $\bar{\bar{F}}(z_1)$ is known in $z = z_1$, we can obtain the solution at another point $z = z_2$, considering:

$$\bar{\bar{F}}(z_2) = e^{G(z_2-z_1)}\bar{\bar{F}}(z_1) \tag{6.13}$$

The "propagating coefficient" from z_1 to z_2 is the exponential of a matrix, defined by the following expansion:

$$e^{G(z_2-z_1)} = \sum_{p=0}^{\infty}\frac{(z_2-z_1)^p}{p!}G^p \tag{6.14}$$

The numerical analysis of this exponential is possible for a matrix G with a finite dimension. This implies, that we need to consider a finite number of diffraction orders, which means that the values m of the expansion are limited by two integers:

$$-M \leq m \leq M$$

The dimension of the matrix G is therefore limited to 4(2M+1) and the exponential function of the matrix can be calculated. To solve Equ. (6.14), a Padé approximant method, i.e. approximation by a rational function, is used. This technique, written in Fortran, can be easily

found on specific libraries [125].

Homogeneous zones

The diffractive layer is surrounded by the incident and emergent medium characterized by a constant refractive index. Between each film, we will consider artificially a homogeneous region characterized by the same refractive index as the incident region. The thickness of this region tends to zero, but the fields can be expressed as a linear combination of a homogeneous environment.

A homogeneous region is characterized by a dielectric constant which is completely independent of any space coordinate. The Fourier expansion is reduced therefore to a constant:

$$\varepsilon(y) = \varepsilon$$

ε being ε_i (dielectric constant of the incident medium) in the incident region and the artificial junction between the films and ε_t (dielectric constant of the emergent medium) in the emergent region. The Fourier coefficients necessary to describe Maxwell's equations are brought to

$$\varepsilon_m = \varepsilon\delta_{m,0}$$

This leads to a remarkable simplification for the field component equations which need to be solved (Eqs. (6.4), (6.5), (6.7), (6.8)). These equations can be uncoupled from the others to form Helmholtz equations.

$$\frac{d^2E_{x,m}}{dz^2} = -k_{z,m}^2 E_{x,m}$$

$$\frac{d^2E_{y,m}}{dz^2} = -k_{z,m}^2 E_{y,m}$$

$$\frac{d^2H_{x,m}}{dz^2} = -k_{z,m}^2 H_{x,m}$$

$$\frac{d^2H_{y,m}}{dz^2} = -k_{z,m}^2 H_{y,m}$$

$k_{z,m}$ being expressed as

$$k_{z,m} = \sqrt{\varepsilon\frac{\omega^2}{c^2} - k_x^2 - \left(k_y + m\frac{2\pi}{b}\right)^2}$$

This quantity can be a real or an imaginary quantity. As a convention, we will take the positive value of the root, if $k_{z,m}$ is real and the positive value of its imaginary part, if $k_{z,m}$ is imaginary.

Each incident plane wave is a transversal wave where the directions of the field amplitudes are perpendicular to the propagation direction. The polarization direction contains two polar-

izations fixed to the transverse electric (TE) and transverse magnetic (TM) mode. However, we do not necessary find an effective separation of these two modes, as they are mixed through the corrugations.

The propagation direction of the m^{th} beam is given by the following vector:

$$\overrightarrow{q_m} = k_x \overrightarrow{e_x} + \left(k_y + m\frac{2\pi}{b} \right) \overrightarrow{e_y}$$

This beam propagates in the plane defined by the vector $\overrightarrow{q_m}$ and the normal vector $\overrightarrow{e_z}$.

$$\vec{\eta}_m = \frac{\overrightarrow{q_m}}{|\overrightarrow{q_m}|} \times \overrightarrow{e_z}$$

$\vec{\eta}_m$ being a unitary vector defined perpendicular to the plane of propagation. $\vec{\eta}_m$ is used as the direction for the TE mode. The unitary vector that indicates the direction of the TM polarization is defined by the vector $\vec{\chi}_m^{\pm}$, which is orthogonal to $\vec{\eta}_m$ and the wave propagation direction.

$$\vec{\chi}_m^{\pm} = \mp \frac{k_{z,m} c}{\omega\sqrt{\varepsilon}} \frac{\overrightarrow{q_m}}{|\overrightarrow{q_m}|} + \frac{|\overrightarrow{q_m}|\, c}{\omega\sqrt{\varepsilon}} \overrightarrow{e_z}$$

$\vec{\chi}_m^{+}$ is defined for the waves that propagates in the direction of positive z and $\vec{\chi}_m^{-}$ is defined for the waves propagating in the direction of the negative z. A general electric field can then be written considering these four contributions:

$$\begin{aligned}
\overrightarrow{E}(\vec{r}, t) = & \sum_m N_m^+ \vec{\eta}_m e^{ik_{z,m}(z-z_0)} e^{i(\vec{q}_m \cdot \vec{\rho} - \omega t)} \\
& + \sum_m N_m^- \vec{\eta}_m e^{-ik_{z,m}(z-z_0)} e^{i(\vec{q}_m \cdot \vec{\rho} - \omega t)} \\
& + \sum_m X_m^+ \chi_m^+ e^{ik_{z,m}(z-z_0)} e^{i(\vec{q}_m \cdot \vec{\rho} - \omega t)} \\
& + \sum_m X_m^- \chi_m^- e^{-ik_{z,m}(z-z_0)} e^{i(\vec{q}_m \cdot \vec{\rho} - \omega t)}
\end{aligned}$$

The amplitudes N_m^+ and N_m^- represent the contribution of the TE polarization for waves that propagates in the direction of increasing and decreasing z, respectively. The amplitudes X_m^+ and X_m^- represent the contribution of the TM polarization for both propagation directions.

The magnetic field can be expressed in a similar manner, using the equation that relates $\overrightarrow{H}$ to $\overrightarrow{E}$.

$$\overrightarrow{H} = \frac{1}{i\omega\mu_0} \overrightarrow{\nabla} \times \overrightarrow{E}$$

and

$$\begin{aligned}\vec{H}(\vec{r},t) = &-\frac{\sqrt{\varepsilon}}{c\mu_0}\sum_m N_m^+\vec{\chi}_m^+ e^{ik_{z,m}(z-z_0)}e^{i(\vec{q}_m\cdot\vec{\rho}-\omega t)}\\ &-\frac{\sqrt{\varepsilon}}{c\mu_0}\sum_m N_m^-\vec{\chi}_m^- e^{-ik_{z,m}(z-z_0)}e^{i(\vec{q}_m\cdot\vec{\rho}-\omega t)}\\ &+\frac{\sqrt{\varepsilon}}{c\mu_0}\sum_m X_m^+\vec{\eta}_m e^{ik_{z,m}(z-z_0)}e^{i(\vec{q}_m\cdot\vec{\rho}-\omega t)}\\ &+\frac{\sqrt{\varepsilon}}{c\mu_0}\sum_m X_m^-\vec{\eta}_m e^{-ik_{z,m}(z-z_0)}e^{i(\vec{q}_m\cdot\vec{\rho}-\omega t)}\end{aligned}$$

The abscissa z_0 is arbitrary, but necessary to fix the wave's phase and it influences the definition of the fields complex amplitudes. In each homogeneous region, z_0 will be defined at a recognizable abscissa of the specific region, i.e.: for the incident and emergent medium, z_0 will be defined at the coordinate z on the contact surfaces of the films; for the artificial junction films, z_0 will be defined as the coordinate z at the junctions.

In the expression of the fields, only the two Cartesian components x and y are used. The TE polarization vector is in the $x-y$ plane, by definition, but the TM polarization has a component in the z-direction. This information is not relevant at the moment. The electric field can then be described by the information included in the following equations, at all diffraction orders m:

$$\begin{aligned}\overrightarrow{E}_{//,m}(z) = &N_m^+\vec{\eta}_m e^{ik_{z,m}(z-z_0)} + N_m^-\vec{\eta}_m e^{-ik_{z,m}(z-z_0)}\\ &-X_m^+\vec{\mu}_m e^{ik_m(z-z_0)} + X_m^-\vec{\mu}_m e^{-ik_m(z-z_0)}\end{aligned} \tag{6.15}$$

$\vec{\mu}_m$ being the component of the TM polarization parallel to the scattering film in the $x-y$ plane .

$$\vec{\mu}_m = \frac{k_{z,m}c}{\omega\sqrt{\varepsilon}}\frac{\vec{q}_m}{|\vec{q}_m|}$$

The significant components for the magnetic field are expressed by:

$$\begin{aligned}\vec{H}_{//,m}(z) = \frac{\sqrt{\varepsilon}}{c\mu_0}\big[&N_m^+\vec{\mu}_m e^{ik_{z,m}(z-z_0)} - N_m^-\vec{\mu}_m e^{-ik_{z,m}(z-z_0)}\\ &+ X_m^+\vec{\eta}_m e^{ik_{z,m}(z-z_0)} + X_m^-\vec{\eta}_m e^{-ik_{z,m}(z-z_0)}\big]\end{aligned} \tag{6.16}$$

The information about the fields is distributed in all the diffraction orders - both propagative with $k_{z,m}$ real and evanescent with $k_{z,m}$ imaginary - and - for each diffraction order - on the four amplitudes of the waves propagating along the two directions of the z-axis, with the TE and TM polarizations. Equs. (6.15) and (6.16) can be understood as a change in the representation of the fields. As a initial condition for the ordinary differential equations, we use the relation between the value of the fields at the point z_0 and the amplitudes of scattered waves.

$$\begin{bmatrix} E_{x,m}(z_0)\\ E_{y,m}(z_0)\\ \frac{c\mu_0}{\sqrt{\varepsilon}}H_{x,m}(z_0)\\ \frac{c\mu_0}{\sqrt{\varepsilon}}H_{y,m}(z_0)\end{bmatrix} = \begin{bmatrix} \eta_{xm} & -\mu_{xm} & \eta_{xm} & \mu_{xm}\\ \eta_{ym} & -\mu_{ym} & \eta_{ym} & \mu_{ym}\\ \mu_{xm} & \eta_{xm} & -\mu_{xm} & \eta_{xm}\\ \mu_{ym} & \eta_{ym} & -\mu_{ym} & \eta_{ym}\end{bmatrix}\begin{bmatrix} N_m^+\\ X_m^+\\ N_m^-\\ X_m^-\end{bmatrix} \tag{6.17}$$

By inverting the above equation, we obtain:

$$\begin{bmatrix} N_m^+ \\ X_m^+ \\ N_m^- \\ X_m^- \end{bmatrix} = \frac{1}{\Delta} \begin{bmatrix} \mu_{ym} & -\mu_{xm} & -\eta_{ym} & \eta_{xm} \\ \eta_{ym} & -\eta_{xm} & \mu_{ym} & -\mu_{xm} \\ \mu_{ym} & -\mu_{xm} & \eta_{ym} & -\eta_{xm} \\ -\eta_m & \eta_{xm} & \mu_{ym} & -\mu_{xm} \end{bmatrix} \begin{bmatrix} E_{x,m}(z_0) \\ E_{y,m}(z_0) \\ \frac{c\mu_0}{\sqrt{\varepsilon}} H_{x,m}(z_0) \\ \frac{c\mu_0}{\sqrt{\varepsilon}} H_{y,m}(z_0) \end{bmatrix} \tag{6.18}$$

with $\Delta = 2\left(\eta_{xm}\mu_{ym} - \eta_{ym}\mu_{x\mathrm{Im}}\right)$. The values of the transversal fields in the plane $z = z_0$, which can always be considered as a homogeneous, infinite thin region, and the amplitudes of the waves propagating in this homogeneous region are related in an univocal way. The coefficients X and N for all the diffraction orders form a representation of the fields. The transformations (6.17) and (6.18) describe a given diffraction order m and no coupling of the diffracted waves appear in these equations. The transformation, referred to as U, that leads the wave amplitudes, expressed by N and X, to the wave amplitudes expressed in the plane $z = z_0$ is a direct product of $2M + 1$ 4-by-4 matrices. The transformation from one representation to another is thereby significantly simplified and the numerical implementation is accelerated.

Transfert matrices T

For each diffraction order m, two representations of the field values in the plane z_0 can be written: the first one is the four-vector $\bar{F}(z_0)$, given by Equ. (6.10); the other representation is the four-vector $\bar{P}_m(z_0)$.

$$\bar{P}_m(z_0) = \begin{bmatrix} N_m^+ \\ X_m^+ \\ N_m^- \\ X_m^- \end{bmatrix} \tag{6.19}$$

It forms, such as $\bar{\bar{F}}(z_0)$, a supervector expressed as

$$\bar{\bar{P}}\left(z_0\right) = \begin{bmatrix} \ldots \\ \bar{P}_{-1} \\ \bar{P}_0 \\ \bar{P}_1 \\ \ldots \end{bmatrix} \tag{6.20}$$

The four-vector is rearranged in another form, where the elements are grouped primary as a function of their different diffraction orders and then as a function of the propagation directions and the polarizations.

$$\bar{N}^+ = \begin{bmatrix} \cdots \\ N_{-1}^+ \\ N_0^+ \\ N_1^+ \\ \cdots \end{bmatrix} \quad \bar{X}^+ = \begin{bmatrix} \cdots \\ X_{-1}^+ \\ X_0^+ \\ X_1^+ \\ \cdots \end{bmatrix} \quad \bar{N}^- = \begin{bmatrix} \cdots \\ N_{-1}^- \\ N_0^- \\ N_1^- \\ \cdots \end{bmatrix} \quad \bar{X}^- = \begin{bmatrix} \cdots \\ X_{-1}^- \\ X_0^- \\ X_1^- \\ \cdots \end{bmatrix}$$

The amplitudes supervector can then be expressed as

$$\tilde{P}(z_0) = \begin{bmatrix} \bar{N}^+ \\ \bar{X}^+ \\ \bar{N}^- \\ \bar{X}^- \end{bmatrix} \tag{6.21}$$

These two forms of the supervector (Eqs. (6.20) and (6.20)) differ only by a permutation of their elements, represented by a constant matrix V.

$$\bar{\bar{P}}(z_0) = V\,\tilde{P}(z_0) \tag{6.22}$$

The three defined supervectors ($\bar{\bar{F}}, \bar{\bar{P}}$ and $\tilde{P}$) include exactly the same information about the electric fields. The transformation from $\bar{\bar{P}}(z_0)$ to $\bar{\bar{F}}(z_0)$ is defined by the Eqs. (6.17), (6.18) and (6.22).

$$\bar{\bar{F}}(z_0) = UV\tilde{P}(z_0) \tag{6.23}$$

Two "transfer matrices" allow the propagation of the field information from the abscissa z_1 to the abscissa z_2. The first one connects the supervector $\bar{\bar{F}}(z_2)$ to $\bar{\bar{F}}(z_1)$ (see Equ. (6.13)):

$$A = e^{G(z_2 - z_1)}$$

The second one connects the amplitude supervectors $\tilde{P}(z_2)$ and $\tilde{P}(z_1)$.

$$\tilde{P}(z_2) = T\tilde{P}(z_1) \tag{6.24}$$

The relation between T and A can be found when combining Eqs. (6.13), (6.23) and (6.24)

$$\tilde{P}(z_2) = V^{-1}U^{-1}\bar{\bar{F}}(z_2) = V^{-1}U^{-1}A\bar{\bar{F}}(z_1) = V^{-1}U^{-1}AU\bar{\bar{P}}(z_1)$$

$$= (UV)^{-1}A(UV)\tilde{P}(z_1)$$

The transfer matrix can then be expressed as

$$T = (UV)^{-1}A(UV)$$

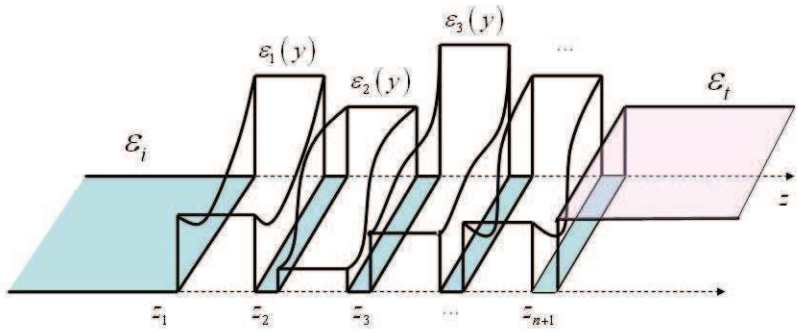

Figure XI: Homogeneous regions, where the field development as progressive waves is possible, are represented in colors. The concerned regions are the incident and emergent medium and the infinite thin junctions between the films.

In this system, the homogeneous regions are distributed as shown in Fig XI. The photonic structure layer extends from z_1 to z_{n+1} and is divided in n sublayers. At each junction (z=z_i) we make the hypothesis of a homogeneous, infinite thin region. The initial conditions are defined as z_0=z_1 in the incident region, z_0=z_i in the junctions of the i^{th} layer. The associated transfer matrix T_i propagates the fields from z_i to z_{i+1}. The assembly of the T matrices from successive sublayers is done by multiplying them:

$$\bar{\bar{P}}(z_1) = T_1\bar{\bar{P}}(z_2) = T_1T_2\bar{\bar{P}}(z_3) = ... = T_1T_2T_3...T_n\bar{P}(z_{n+1})$$

and

$$T = T_1T_2T_3...T_n$$

This matrix connects the incident and diffracted beam amplitudes in the incident region to the ones in the emergent regions. However, this does not solve the scattering problem of the considered photonic layer. In a scattering problem, the incident wave is given and the reflectance and transmittance amplitudes of the diffracted beams should be deducted. In the scattering theory, it is the S matrix that connects the amplitudes of the outgoing waves to the amplitudes of the ingoing waves. This S matrix can be deduced from the T matrix, but at two and three dimensions, this operation is complicated due to the presence of evanescent diffracted waves. These evanescent diffracted waves induce rapid variations over several order of magnitudes and lead to a large numerical instability.

We do therefore not assemble the T matrices of the successive sublayers, but the S matrices, which can be calculated form the T matrices. The transformation from T matrix to S matrix is stable if the thickness of the film is small (i.e. about 1% of the considered wavelength). The assembly of the S matrices is not just a simple multiplication, such as in the T matrix case, but the assembly relations are known and perfectly stable.

Construction and assembly of the S matrices

To build and assemble the S matrices, connecting the outgoing waves to the ingoing waves, it is necessary to define the ways propagating in the direction of $z \to +\infty$ and the waves propagating in the opposite direction.

$$i^+ = \begin{pmatrix} N^+(z_1) \\ X^+(z_1) \end{pmatrix}, \quad r^- = \begin{pmatrix} N^-(z_1) \\ X^-(z_1) \end{pmatrix}$$

$$t^+ = \begin{pmatrix} N^+(z_2) \\ X^+(z_2) \end{pmatrix}, \quad i^- = \begin{pmatrix} N^-(z_2) \\ X^-(z_2) \end{pmatrix}$$

The i^+ state names the TE and TM waves propagating in the incident medium towards the film. These waves originate from distant sources, $z \to -\infty$. The i^- state names the TE and TM waves propagating in the emergent medium towards the layer, originating also from distant sources, but in the $z \to +\infty$ direction. These waves are called "ingoing" waves. In our case $i^- = 0$, as there is only one single ingoing beam, originating from $z \to -\infty$.

The r^- state names the TE and TM waves in the incident medium propagating away from the layer. These waves are backscattered waves by diffraction, referred to as reflected waves. The t^+ state names the TE and TM waves that, after being transmitted through the layer into the emergent medium, propagates also away from the layer. The amplitudes of these "outgoing" waves will be calculated by the scattering matrix technique.
The T matrix is defined by

$$\begin{bmatrix} i^+ \\ r^- \end{bmatrix} = \begin{bmatrix} T^{++} & T^{+-} \\ T^{-+} & T^{--} \end{bmatrix} \begin{bmatrix} t^+ \\ i^- \end{bmatrix} \tag{6.25}$$

$T^{\pm\pm}$ being square matrices of order 2(2M+1). The S matrix that gives the amplitudes of the outgoing waves as a function of the amplitudes of the ingoing waves is described by

$$\begin{bmatrix} t^+ \\ r^- \end{bmatrix} = \begin{bmatrix} S^{++} & S^{+-} \\ S^{-+} & S^{--} \end{bmatrix} \begin{bmatrix} i^+ \\ i^- \end{bmatrix} \tag{6.26}$$

By comparing and reorganizing Eqs. (6.25) and (6.26) the relations between the elements of the S atrix and the T matrix can be established.

$$\begin{aligned} S^{++} &= [T^{++}]^{-1} \\ S^{+-} &= -[T^{++}]^{-1} T^{+-} \\ S^{-+} &= T^{-+} [T^{++}]^{-1} \\ S^{--} &= T^{--} - T^{-+} [T^{++}]^{-1} T^{+-} \end{aligned} \tag{6.27}$$

We can express the S matrix associated to a sublayer using Eqs. (6.27). The condition of the T^{++} matrix, that will be inverted, needs to be controlled by fixing the thickness of the sublayer. The condition of a matrix is a calculated value that indicates the order of magnitude of lost significant figures during the inversion. If this loss value is high, layer needs to be divided in

thinner sublayers.

The S matrix of the whole layer is obtained by combining the S matrices of each individual sublayer. The combination of two S matrices from two successive layers S_1 and S_2 is defined by the following algebraic transformations.

$$\begin{aligned} S^{++} &= S_2^{++}\left(1 - S_1^{+-}S_2^{-+}\right)^{-1} S_1^{++} \\ S^{+-} &= S_2^{+-} + S_2^{++}\left(1 - S_1^{+-}S_2^{-+}\right)^{-1} S_1^{+-}S_2^{--} \\ S^{-+} &= S_1^{-+} + S_1^{--}S_2^{-+}\left(1 - S_1^{+-}S_2^{-+}\right)^{-1} S_1^{++} \\ S^{--} &= S_1^{--}\left[1 + S_2^{-+}\left(1 - S_1^{+-}S_2^{-+}\right)^{-1} S_1^{+-}\right] S_2^{--} \end{aligned} \tag{6.28}$$

These equations are numerically stable, which means that if two scattering matrices S are known, even for thick films, the global S matrix does not suffer from an amplified error. In the case of an identical sublayers stacking, represented by repeated transfer matrices, the assembly of the matrices can be done in a particularly economic way: if the numbers of layers is a power of two, we can primary assembly the first two identical sublayers, then assemble this result with itself and continue this doubling with each iteration until obtaining the full layer S-matrix expression.

Exit from the film

The dielectric constant changes from ε_i to ε_t at the exit of the film and a refraction takes place. This variation in the direction of the diffracted beams needs a new definition of the $k_{z,m}$ component and, as well, of the polarization vectors. In the expression of the T matrix, these appear essentially in the U matrix transformation, that connects the amplitude supervector $\tilde{P}(z_0)$ with the field supervector $\bar{\bar{F}}(z_0)$ (Equ. (6.23)). The junction between the artificial region $\varepsilon = \varepsilon_i$ and the emergent region $\varepsilon = \varepsilon_t$ is abrupt and the propagation is reduced to a distance equal to zero ($\Delta z = 0$). The transfer matrix A becomes

$$A = e^{iG\Delta z} = 1$$

The T matrix corresponding to this abrupt transition of dielectric constants is

$$T = (U|_{\varepsilon=\varepsilon_i} V)^{-1}(U|_{\varepsilon=\varepsilon_t} V)$$

This being defined, the solution of the S matrix and its assembly uses the procedure described in the previous section.

The S matrix is then known for the propagation of the waves through the structure and describing the connexion between the incident and the emergent medium. The knowledge of the incident waves amplitudes, in the TE and TM polarizations ($N_{0,i}^{+} = N_0^{+}(z_1)$ and $X_{0,t}^{+} = X_0^{+}(z_{n+1})$) and the absence of a contra-progressive incident wave allows to determine the amplitudes of the reflected waves ($N_m^{-}(z_1)$ and $X_m^{-}(z_1)$) and the transmitted waves ($N_m^{+}(z_{n+1})$

and $X_m^+(z_{n+1})$) for all the diffraction orders.

From these coefficients, the current density of energy carried by each diffracted wave can be calculated. The current carried by all the reflected, diffracted beams is

$$J_r^+ = \frac{\sigma}{2\mu_0\omega}\sum_m k_{z,m,i}\left(\left|N_{m,i}^+\right|^2 + \left|X_{m,i}^+\right|^2\right)\Theta\left(\varepsilon_i\frac{\omega^2}{c^2} - |\vec{q}_m|^2\right) \tag{6.29}$$

The current carried by all the transmitted, diffracted beams is defined as

$$J_t^+ = \frac{\sigma}{2\mu_0\omega}\sum_m k_{z,m,t}\left(\left|N_{m,t}^+\right|^2 + \left|X_{m,t}^+\right|^2\right)\Theta\left(\varepsilon_t\frac{\omega^2}{c^2} - |\vec{q}_m|^2\right) \tag{6.30}$$

These two values of the current density are, in general, related to the incident current density

$$J_i^+ = \frac{\sigma}{2\mu_0\omega}k_{z,0}\left[\left|N_0^+\right|^2 + \left|X_0^+\right|^2\right]$$

F. *ELDIM EZContrast XL*80*MS* scatterometer

The *ELDIM EZContrast XL*80*MS* scatterometer contains a Fourier lenses system to make the measurements of the hemispheric emission by the sample, for polar angles θ varying from 0° to 80° and azimuthal angles φ over the whole hemisphere (0° to 360°). The Fourier system (Fig. XII(b)) is a combination of lenses with increasing radius of curvature that collects the light emitted by the sample surface. The different light rays emitted at specific polar and azimuthal angles are redirected along the optical axis of the system and focused on a plane called the "Fourier plane" (Fig. XII(a)). The angular dependence becomes linear in the Fourier plane: $r = k\theta$. The radiance in the Fourier plane can be calculated as follows:

$$E(r, \varphi) = L(\theta, \varphi) S_0 \frac{\sin \theta}{k^2 \theta}$$

$L(\theta, \varphi)$ being the measured luminance of the object and S_0 being the surface analyzed by the Fourier lenses system.

The wavelength dependence of the radiance is preserved in the integrated power, reflecting the spectral profile of the electroluminescent emission. More precisely, 31 narrow (13 nm) bandpass filters were placed, in turn, on the path to the CCD two-dimensional photon sensor (Fig. XII(c)). The exact transmission of these filters is accounted for in the determination of the absolute recorded power value. Polarizers and wave-plates allow a full polarization analysis of the light.

Figure XIII shows the radiance spectra measured on (a) the firefly and (b) the diode. The light is emitted in both cases in a homogeneous way and no clear preferential directions can be determined. The polarization states of the emission were as well measured in both cases and no specific polarization could be detected. A precaution has to be taken in the firefly case: the analyzed specimen was dead and the light introduced by a external non-polarized light source. From these observations a possible polarization effect in the alive specimen cannot be ruled out.

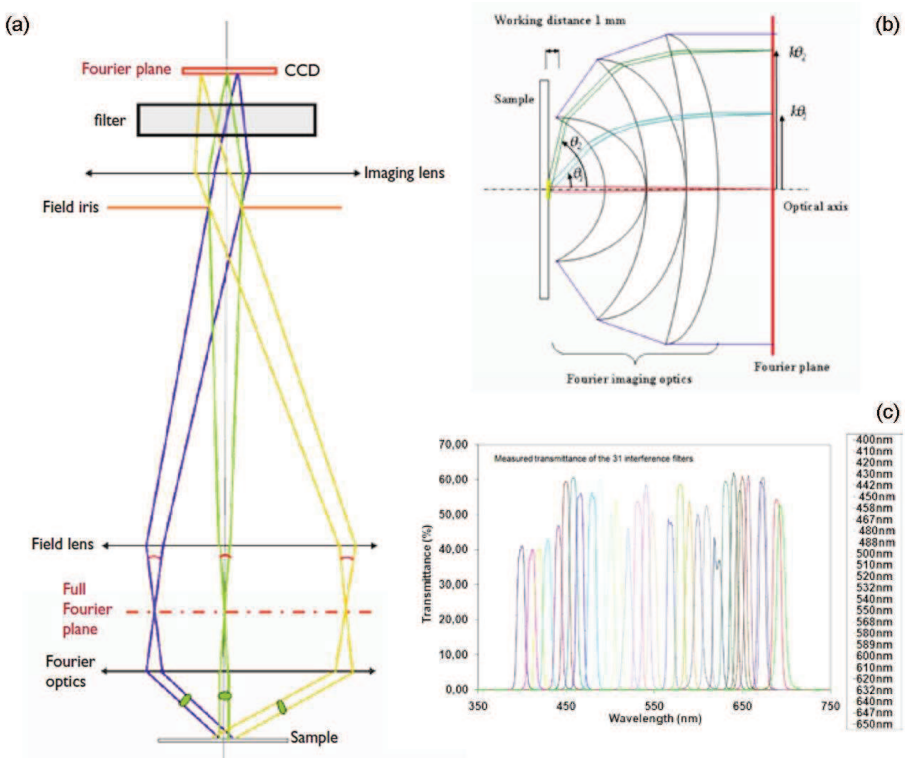

Figure XII: (a) Optical configuration of the *ELDIM EZContrast XL*80*MS*. (b) Schematic diagram of a standard Fourier lenses system. (c) Measured transmittance of the 31 bandpass filters. (Credit: Product data sheet *EZContrast MS*)

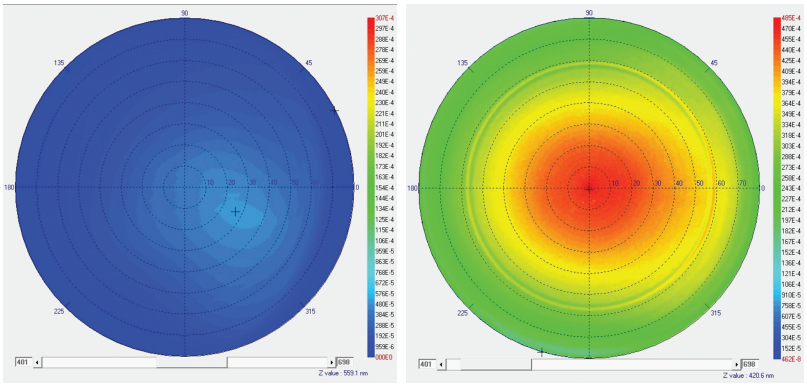

(a) Photoris (b) Patterned LED

Figure XIII: Measured radiance

Glossary

This Glossary is meant to clarify several terms used in this manuscript. Several definitions and explanations are taken from Concise Oxford English Dictionary [126] or Wikipedia.

Aposematic Denoting colorations or markings serving to warn or repel predators (*Zoology*).

Apterous Having no wings (*Entomology*).

Bathyal Relating to the zone of the sea between the continental shelf and the abyssal zone.

Benthic zone The ecological region at the lowest level of a body of water such as an ocean or a lake, including the sediment surface and some sub-surface layers.

Biomimetic Biomimetics is the study of the structure and function of biological systems as models for the design and engineering of materials and machines.

Bioluminescence The biochemical emission of light by living organisms such as glow-worms and deep-sea fishes.

Bloch's theorem Bloch's theorem states that the energy eigenfunction of a periodical system can be written as the product of a plane wave envelope function and a periodic function $u_{n\,\overrightarrow{k}}(\overrightarrow{r})$ with the same periodicity as the system:

$$\psi_{n\,\overrightarrow{k}}(\overrightarrow{r}) = \exp^{i\,\overrightarrow{k}.\overrightarrow{r}}\, u_{n\,\overrightarrow{k}}(\overrightarrow{r})$$

Brachypterous having rudimentary or abnormally small wings.

Bravais lattice The Bravais lattice is an infinite array of discrete points generated by a set of discrete translation operations described by:

$$\overrightarrow{R} = n_1\overrightarrow{a_1} + n_2\overrightarrow{a_2} + n_3\overrightarrow{a_3}$$

Brillouin zone The first Brillouin zone is a uniquely defined primitive cell in reciprocal space. The boundaries of this cell are given by planes related to points on the reciprocal lattice. The reciprocal lattice of a lattice (such as a Bravais lattice) is the lattice in which the Fourier transform of the spatial wave function of the original lattice (or direct lattice) is represented.

Decarboxylation A chemical reaction that removes a carboxyl group and releases carbon dioxide (CO_2).

Exoskeleton A rigid external covering for the body in some invertebrate animals, especially arthropods (*Zoology*).

Setae A stiff hair-like or bristle-like structure (*Zoology*).

LEE or light extraction efficiency The theoretical light extraction efficiency ζ is defined as the ratio of the light intensity extracted into free space I_{trans} over the light emitted in the active material I_{inc}

$$\zeta(\%) = \frac{I_{trans}}{I_{inc}}.100$$

LEE enhancement

$$\Delta\zeta(\%) = \frac{\zeta_{struct} - \zeta_{ref}}{\zeta_{ref}}.100$$

Lantern Another word to describe the bioluminescent organ of insects.

Light extraction cone The light extraction cone is defined as the three-dimensional opening where light can be extracted effectively without total internal reflection according to Snell's law.

Luminescence The emission of light by a substance that has not been heated, as in fluorescence or luminescence.

Macropterous Having long wings or fins.

Mimicry The close external resemblance of an animal or plant to another animal, plant or inanimate object (*Biology*).

Pelagic Relating to the open sea.

Peroxisome Peroxisomes are also called microbodies and are organelles found on eukaryotic cells. They are involved in the catabolism reactions of the cell.

Photophore A light-producing organ in certain fishes and other animals (*Zoology*)

Photocyte A cell, specialized to produce bioluminescence.

Phylogeny The evolutionary development and diversification of a species or group of organisms (*Biology*).

Plane waves Plane waves are constant-frequency waves whose wavefronts are infinite parallel planes of constant peak-to-peak amplitude normal to the wave vector $\overrightarrow{k}$ (*Physics*).

Pronotum The dorsal plate of the prothorax in insects. The prothorax being the anterior part of the insect thorax; it carries the first pair of legs (*Entomology*).

Ternary complex A Ternary complex refers to a protein complex containing three different molecules which are bound together.

Tracheole The fine respiratory tube of the trachea of an insect. The trachea being an air passage in the body of an insect (*Entomology*).

Transmittivity, Transmittance and Transmission William L. Wolfe gives a note about the difference in these terms in his book "Introduction to radiometry" [127]. "*It is generally accepted that the ending* ion *signifies a process. Emission is the process of radiating. Transmission is the process of transmitting. ... An* ance *ending is said to indicate the property of a particular sample. Thus, one reports the reflectance of sample 2306... . The* ivity *ending is meant to signify the property of the "generic brand", an idealized sample that represents all such samples of that material. ... For reflectivity, the sample must be pure, clean, and smooth enough that the reflection is not affected by any lack thereof. ...*"

Keeping these definitions in mind, we will use the term *transmittance* for the measurements and the term *transmissivity* for the simulations.

Bibliography

[1] M. Planck, *The Theory of Heat Radiation.* (P. Blakiston's Son & Co, 1914), 2nd ed. M. Masius (transl.).

[2] R. Kane and H. Sell, *Revolution in lamps: a chronicle of 50 years of progress* (The Fairmont Press Inc., 2001), 2nd ed.

[3] E. Wiedemann, "Über Fluoreszenz und Phosphoreszenz," Annalen der Physik **34**, 446–463 (1888).

[4] A. Jablonski, "Efficiency of anti-stokes fluorescence in dyes," Nature **131**, 839–840 (1933).

[5] L. L. Lucas and M. P. Unterweger, "Comprehensive review and critical evaluation of the half-life of tritium," Journal of Research of the National Institute of Standards and Technology **105**, 541 (2000).

[6] M. G. Jesus and M. G. F. J., "Triboluminescence of new uranyl salts," Journal of Chemical Education **55**, 340 (1978).

[7] A. Al-Hashimi, A. M. Eid, K. V. Ettinger, and J. Mallard, "On piezoluminescence in irradiated alkali halides," Radiat. Prot. Dosimetry **6**, 203–205 (1983).

[8] E. Huntress, L. Stanley, and A. Parker, "The preparation of 3-aminophthalhydrazide for use in the demonstration of chemiluminescence," Journal of the American Chemical Society **56**, 241–242 (1934).

[9] C. F. Moss and A. Surlykke, "Auditory scene analysis by echolocation in bats," J. Acoust. Soc. Am. **110**, 2207–2226 (2001).

[10] S. Johnsen, T. M. Frank, S. H. D. Haddock, E. A. Widder, and C. G. Messing, "Light and vision in the deep-sea benthos: I. bioluminescence at 500-1000nm depth in the Bahamian Islands," J. Exp. Biol. **215**, 3335–3343 (2012).

[11] M. Miya, T. W. Pietsch, J. W. Orr, R. J. Arnold, T. P. Satoh, A. M. Shedlock, H. Ho, M. Shimazaki, M. Yabe, and M. Nishida, "Evolutionary history of anglerfishes (teleostei: Lophiiformes): A mitogenomic perspective," BMC Evolutionary Biology **10** (2010).

[12] C. P. Kenaley and K. E. Hartel, "A revision of atlantic species of photostomias (Teleostei: Stomiidae: Malacosteinae), with a description of a new species," Ichthyol. Res. **52**, 251–263 (2005).

[13] J. M. Claes and J. Mallefet, "The lantern shark's light switch: turning shallow water crypsis into midwater camouflage," Biol. Lett. **6**, 685–687 (2010).

[14] P. J. Herring, "Luminescence in cephalopods and fish," Symp. Zool. Soc. Lond **38**, 127–159 (1977).

[15] K. J. Osborn, S. H. D. Haddock, F. Pleijel, L. P. Madin, and G. W. Rouse, "Deep-sea, swimming worms with luminescent "bombs"," Science **325**, 964 (2009).

[16] A. Heger, N. J. King, B. D. Wingham, A. J. Jamieson, P. M. Bagley, L. Allan, O. Pfannkuche, and I. G. Priede, "Benthic bioluminescence in the bathyal North East Atlantic: luminescent responses of *Vargula norvegica* (Ostracoda: Myodocopida) to predation by the deep-water eel (*Synaphobranchus kaupii*)," Mar. Biol. **151**, 1471–1478 (2007).

[17] D. Deheyn, J. Mallefet, and M. Jangoux, "Expression of bioluminescence in *Amphipholis squamata* (Ophiuroidea: Echinodermata) in presence of various organisms: a laboratory study," J. Mar. Biol. Assoc. UK **80**, 179–180 (2000).

[18] S. D. Miller, S. H. D. Haddock, C. D. Elvidge, and T. F. Lee, "Detection of a bioluminescent milky sea from space," P. Natl. A. Sci. **102**, 14181–14184 (2012).

[19] W. H. Biggley, E. Swift, R. J. Buchanan, and H. H. Seliger, "Stimulable and spontaneous bioluminescence in the marine dinoflagellates, *Pyrodinium bahamense*, *Gonyaulax polyedra*, and *Pyrocystis lunula*," J. Gen. Physiol. **54**, 96–122 (1969).

[20] S. H. D. Haddock, M. A. Moline, and J. F. Case, "Bioluminescence in the Sea," Ann. Rev. Mar. Sci **2**, 443–493 (2010).

[21] D. Deheyn and N. Wilson, "Bioluminescent signals spatially amplified by wavelength-specific diffusion through the shell of a marine snail," Proc. R. Soc. B **278**, 2112–2121 (2011).

[22] V. B. Meyer-Rochow, "Glowworms: a review of *Arachnocampa* spp. and kin," Luminescence **22**, 251–265 (2007).

[23] V. R. Viviani, J. W. Hastings, and T. Wilson, "Two bioluminescent diptera: the North American *Orfelia fultoni* and the Australian *Arachnocampa flava*. Similar niche, different bioluminescence systems," Photochem. Photobiol. **75**, 22–27 (2002).

[24] U. Stolz, S. Valez, K. V. Wood, M. Wood, and J. L. Feder, "Darwinian natural selection for orange bioluminescent color in a Jamaican click beetle," P. Natl. A. Sci. **100**, 14955–14959 (2003).

[25] R. Bellisario, T. E. Spencer, and M. J. Cormier, "Isolation and properties of luciferase, a non-heme peroxidase, from the bioluminescent earthworm, *Diplocardia longa*," Biochemistry **11**, 2256–2266 (1972).

[26] R. DeCock, "Larval and adult emission spectra of bioluminescence in three european firefly species," Photochem. Photobiol. **79**, 339–342 (2004).

[27] E. A. Meighen, "Bacterial bioluminescence: Organization, regulation, and application of the lux genes," FASEB J. **7**, 1016–1022 (1993).

[28] P. V. Dunlap and K. Kita-tsukamoto, "Luminous bacteria," Prokaryotes **2**, 863–892 (2006).

[29] J. C. Makemson, "Luciferase dependent oxygen consumption by bioluminescent vibrios," J. Bacteriol. **165**, 461–466 (1986).

[30] B. J. Bowden, "Some observations on a luminescent freshwater limpet from New Zealand," Biol. Bull. **99**, 373–380 (1950).

[31] J. J. Counsilman and P. P. Ong, "Responses of the luminescent land snail *Dyakia (Quantula) striata* to natural and artificial lights," J. Ethol. **6**, 1–8 (1988).

[32] V. S. Bondar, A. P. Puyzr, K. V. Purtov, S. E. Medvedeva, E. K. Rodicheva, and J. I. Gitelson, "The luminescent system of the luminous fungus *Neonothopanus nambi*," Doklady Biochemistry and Biophysics **438**, 138–140 (2011).

[33] K. Mori, S. Kojima, S. Maki, T. Hirano, and H. Niwa, "Bioluminescence characteristics of the fruiting body of *Mycena chlorophos*," Luminescence **26**, 604–610 (2011).

[34] D. D. Deheyn and M. I. Latz, "Bioluminescence characteristics of a tropical terrestrial fungus (basidiomycetes)," Luminescence **22**, 462–467 (2007).

[35] J. W. Hastings, "Biological diversity, chemical mechanisms, and the evolutionary origins of bioluminescent systems," J. Mol. Evol. **19**, 309–321 (1983).

[36] C. L. Prosser, ed., *Neural and integrative animal physiology - Comparative animal physiology* (Wiley-Liss, New York, USA, 1991), 4th ed.

[37] S. Dove, J. Horwitz, and M. McFall-Ngai, "A biochemical characterization of the photophore lenses of the midshipman fish, *Porichthys notatus* Girard," J. Comp. Physiol. A **172**, 565–572 (1993).

[38] N. F. Lepora, P. Verschure, and T. J. Prescott, "The state of the art in biomimetics," Bioinspir. Biomim. **8**, 01300 1–11 (2013).

[39] O. Karthaus, ed., *Biomimetics in Photonics* (CRC Press, 2013).

[40] S. A. Boden and D. M. Bagnall, "Nanostructured biomimetic moth-eye arrays in silicon by nanoimprint lithography," Proc. SPIE **7401** (2009).

[41] K. IOhara, M. Yoshimura, H. Tabata, and S. Shimuzu, "Structurally colored fibers," Chem. Fibers. Int. **50**, 15–23 (2000).

[42] J. P. Vigneron, M. Rassart, C. Vandenbem, V. Lousse, O. Deparis, L. P. Biró, D. Dedouaire, A. Cornet, and P. Defrance, "Spectral filtering of visible light by the cuticle of metallic woodboring beetles and microfabrication of a matching bioinspired material," Phys. Rev. E **73**, 041905 1–8 (2006).

[43] G. Chen, M. Craven, A. Kim, A. Munkholm, S. Watanbe, M. Camras, W. Götz, and F. Steranka, "Performance of high-power III-nitride light emitting diodes," Phys. Status Solidi A **205**, 1086–1092 (2008).

[44] M. Furno, T. C. Rosenow, M. C. Gather, B. Lüssem, and K. Leo, "Analysis of the external and internal quantum efficiency of multi-emitter, white organic light emitting diodes," Appl. Phys. Lett. **101**, 1–4 (2012).

[45] I. B. J. Sollas, "On the identification of chitin by its physical constants," Proc. R. Soc. Lond. B **79**, 474–481 (1907).

[46] E. Hecht, *Optics* (Addison-Wesley, USA, 1998), 3rd ed.

[47] I. Schnitzer, E. Yablonovitch, C. Caneau, and T. J. Gmitter, "Ultrahigh spontaneous emission quantum efficiency, 99.7% internally and 72% externally, from AlGaAs/GaAs/AlGaAs double heterostructures," Appl. Phys. Lett. **62**, 131–133 (1993).

[48] I. Schnitzer, E. Yablonovitch, C. Caneau, T. J. Gmitter, and A. Scherer, "30 percent external quantum efficiency from surface textured, thin-film light-emitting diodes," Appl. Phys. Lett. **63**, 2174–2176 (1993).

[49] M. Boroditsky, T. F. Krauss, R. Coccioli, R. Vrijen, and R. B. E. Yablonovitch, "Light extraction from optically pumped light-emitting diode by thin-slab photonic crystals," Appl. Phys. Lett. **75**, 1036–1038 (1999).

[50] R. Dylewicz, A. Z. Khokhar, R. Wasielewski, P. Mazur, and F. Rahman, "Nanostructured graded-index antireflection layer formation on InGaN for enhancing light extraction from light-emitting diodes," Appl. Phys. B **107**, 393–399 (2012).

[51] C.-W. Hsu, Y.-C. Lee, H.-L. Chen, and Y.-F. Chou, "Optimizing textured structures possessing both optical gradient and diffraction properties to increase the extraction efficiency of light-emitting diodes," Phot. Nano. Fund. Appl. **10**, 523–533 (2012).

[52] J.-M. Park, Z. Gan, W. Y. Leung, R. Liu, Z. Ye, K. Constant, J. Shinar, R. Shinar, and K.-M. Ho, "Soft holographic interference lithography microlens for enhanced organic light emitting diode light extraction," Opt. Express **19**, A786–A792 (2011).

[53] X.-H. Li, R. Song, Y.-K. Ee, P. Kumnorkaew, J. F. Gilchrist, and N. Tansu, "Light extraction efficiency and radiation patterns of III-nitride light-emitting diodes with colloidal microlens arrays with various aspect ratios," IEEE Photon. J. **3**, 489–499 (2011).

[54] Y. J. Lee, H. C. Kuo, T. C. Lu, B. J. Su, and S. C. Wang, "Fabrication and characterisation of GaN-based LEDs grown on chemical wet-etched patterned sapphire substrates," J. Electrochem. Soc. **153**, G1106–G1111 (2006).

[55] Y.-C. Lee, C.-H. Ni, and C.-Y. Chen, "Enhancing light extraction mechanisms of InGaN-based light-emitting diodes through the integration of imprinting microstructures, patterned sapphire substrates, and surface roughness," Opt. Express **18**, A489–A498 (2010).

[56] V. V. Lysak, J. I. H. Kang, and C.-H. Hong, "Air-structured embedded mirror for enhancement of light extraction efficiency in vertical light-emitting diodes," Optoelectron. Adv. Mat. **5**, 481–483 (2011).

[57] G. M. Wu, C. C. Yen, H. W. Chien, H. C. Lu, T. W. Chang, and T. E. Nee, "Effects of nano-structured photonic crystals on light extraction enhancement of nitride light-emitting diodes," Thin Solid Films **519**, 5074–5077 (2011).

[58] J.-Y. Cho, S.-H. Hong, K.-J. Byeon, and H. Lee, "Light extraction efficiency improvement in GaN-based blue light emitting diode with two-dimensional nano-cavity structure," Thin Solid Films **521**, 115–118 (2012).

[59] Z. Zuo, D. Liu, B. Zhang, J. He, H. Liu, and X. Xu, "Increasing the extraction efficiency of blue light emitting diodes via laser patterned Ga-polar p-GaN surface," Phys. Status Solidi A **208**, 2226–2230 (2011).

[60] J. Chen, Q. Wang, and H. Li, "Enhancement of extraction efficiency by metallic photonic crystal embedding in light-emitting diode," Optik **122**, 1079–1083 (2011).

[61] L. Strause, M. DeLuca, and J. Case, "Biochemical and morphological changes accompanying light organ development in the firefly *Photuris pennsylvanica*," J. Insect. Physiol. **25**, 339–347 (1078).

[62] Y. Oba, N. Mori, M. Yoshida, and S. Inouye, "Identification and characterization of a luciferase isotype in the japanese firefly, *Luciola cruciata*, involving in the dim glow of firefly eggs," Biochemistry **49**, 10788–10795 (2010).

[63] J. Sivinski, "The nature and possible functions of luminescence in coleoptera larvae," Coleops. Bull. **35**, 167–179 (1981).

[64] R. DeCock and E. Matthysen, "Aposematism and bioluminescence: experimental evidence from glow-worm larvae (coleptera: Lampyridae)," Evol. Ecol. **13**, 619–639 (1999).

[65] M. Edmunds, *Defence in Animals. A survey of anti-predator defences* (Longman, New York, USA, 1974).

[66] A. Gonzalez, F. Schroeder, J. Meinwald, and T. Eisner, "N-methylquinolinium 2-carboxylate, a defensive betaine from *Photuris versicolor* fireflies," J. Nat. Prod. **62**, 378–80 (1999).

[67] X. Fu, F. Vencl, N. Ohba, V. Meyer-Rochow, C. Lei, and Z. Zhang, "Structure and function of the reversible glands of the aquatic firefly *Luciola leii* (Coleoptera: Lampyridae)," Chemoecology **17**, 117–124 (2007).

[68] M. Knight, R. Glor, S. R. Smedley, A. González, K. Adler, and T. Eisner, "Firefly toxicosis in lizards," J. Chem. Ecol. **25**, 1981–1986 (1999).

[69] R. DeCock and E. Matthysen, "Glow-worm lavae biluminescence (coleptera: Lampyridae) operates as an aposematic signal upon toads (*Bufo bufo*)," Behav. Ecol. **14**, 103–108 (2003).

[70] R. H. Arnett, M. C. Thomas, P. E. Skelley, and J. H. Frank, eds., *American Beetles, Volume 2: Polyphaga: Scarabaeoidea through Curculionoidea.* (CR Press, Bota Raton, Florida, 2002).

[71] J. F. Case, "Flight studies on photic communication by the firefly *Photinus pyralis*," Integr. Comp. Biol. **44**, 250–258 (2004).

[72] J. E. Lloyd, "Aggressive mimicry in *Photuris*: Firefly femmes fatales," Science **149**, 653–654 (1965).

[73] T. Eisner, M. A. Goetz, D. E. Hill, S. R. Smedley, and J. Meinwald, "Firefly "femmes fatales" acquire defensive steroids (lucibufagins) from their firefly prey," P. Natl. Acad. Sci USA **94**, 9723–9728 (1997).

[74] T. Wilson and J. W. Hastings, "Bioluminescence," Annu. Rev. Cell Dev. Biol. **14**, 197–230 (1998).

[75] J. C. Day, L. C. Tisi, and M. J. Bailey, "Evolution of beetle bioluminescence: the origin of beetle luciferin," Luminescence **19**, 8–20 (2004).

[76] J. Vieira, L. P. da Silva, and J. C. G. E. da Silva, "Advances in the knowledge of light emission by firefly luciferin and oxyluciferin," J. Photoch. Photobio. B **117**, 33–39 (2012).

[77] M. Dubuisson, C. Marchand, and J.-F. Rees, "Firefly luciferin as antioxidant and light emitter: the evolution of insect bioluminescence," Luminescence **19**, 339–334 (2004).

[78] Y. Oba, T. Shintani, T. Nakamura, M. Ojika, and S. Inouye, "Determination of the luciferin contents in luminous and non-luminous beetles," Biosci. Biotechnol. Biochem. **72**, 1384–1387 (2008).

[79] H. H. Seliger and W. D. McElroy, "Spectral emission and quantum yield of firefly bioluminescence," Arch. Biochem. Biophys. **88**, 136–141 (1960).

[80] K. Niwa, Y. Ichino, S. Kumata, Y. Nakajima, Y. Hiraishi, D.-I. Kato, V. R. Viviani, and Y. Ohmiya, "Quantum yields and kinetics of the firefly bioluminescence reaction of beetle luciferases," Photochem. Photobiol. **86**, 1046–1049 (2010).

[81] W. A. Woods, H. Hendrickson, J. Masonland, and S. M. Lewis, "Energy and predation costs of firefly courtship signals," Am. Nat. **170**, 702–708 (2007).

[82] A. Bay, "Influence de l'ultra-structure de la lanterne abdominale des lucioles du genre *Photuris* (Lampyridae) sur le rendement externe de leur émission de lumière," Master's thesis, Facultés Universitaires Notre-Dame de la Paix (2009).

[83] H. Ghiradella, "The anatomy of light production: The fine structure of the firefly lantern," Microscopic Anatomy of Invertebrates **11A: Insecta**, 363–381 (1998).

[84] C. H. Hanna, T. A. Hopkins, and J. B. Buck, "Peroxisomes of the firefy lantern," J. Ultrastruct. Res. **57**, 150–162 (1976).

[85] H. Ghiradella and J. Schmidt, "Fireflies at one hundred plus: A new look at flash control," Integr. Comp. Biol. **44**, 203–212 (2004).

[86] M. Locke and J. T. McMahon, "The origin and fate of microbodies in the fat body of an insect," J. Cell Biol. **48**, 61–78 (1971).

[87] K. N. Smalley, D. E. Tarwater, and T. L. Davidson, "Localization of fluorescent compounds in the firefly light organ," J. Histochem. Cytochem. **28**, 323–359 (1963).

[88] L. Bonnaud. Discussion. Symposium Bioinspiration and Biomimetics , Les Treilles, Tourtour, April 1^{st} 2009.

[89] D. Deheyn. Discussion. SPIE Optics+Photonics, San Diego (CA), Aug. 13^{th} 2012.

[90] J. B. Buck, "The anatomy and physiology of the light organ in fireflies," Ann. N.Y. Acad. Sci. **49**, 397–482 (1948).

[91] M. I. Mackowski, Daniel W; Mishchenko, "Calculation of the t matrix and the scattering matrix for ensembles of spheres," J. Opt. Soc. Am. A **13**, 2266–2278 (1996).

[92] A. Bay, P. Cloetens, H. Suhonen, and J. P. Vigneron, "Improved light extraction in the bioluminescent lantern of a *Photuris* firefly (Lampyridae)," Opt. Express **21**, 764–780 (2013).

[93] J. P. Vigneron and V. Lousse, "Variation of a photonic crystal color with the Miller indices of the exposed surface," Proc. SPIE **6128**, 61281G (2006).

[94] P. Vukusic, J. R. Sambles, and R. J. Wootton, "Quantified interference and diffraction in single *Morpho* butterfly scales," Proc. Biol. Sc. **266**, 1403–1411 (1999).

[95] H. L. Leertouwer, B. D. Wilts, and D. G. Stavenga, "Refractive index and dispersion of butterfly chitin and bird keratin measured by polarizing interference microscopy," Opt. Express **19**, 24061–24066 (2011).

[96] J. D. Joannopoulos, S. G. Johnson, J. N. Win, , and R. D. Meade, *Photonic crystals-Molding the flow of light* (Princeton University Press, 2008), 2nd ed.

[97] C. Kittel, *Physique de l'état solide* (Dunod, France, 2007), 8th ed.

[98] J. P. Vigneron, J.-F. Colomer, N. Vigneron, and V. Lousse, "Natural layer-by-layer photonic structure in the squamae of hoplia coerulea (coleoptera)," Phys. Rev. E **72**, 653–654 (2005).

[99] A. Bay, M. Sarrazin, and J. P. Vigneron, "Search for an optimal light-extracting surface derived from the morphology of a firefly lantern," Opt. Eng. **52**, 1–7 (2013).

[100] U. W. Paetzold, W. Z. M. P. J. Kirchhoff, T. Merdzhanova, S. Michard, R. Carius, A. Gordijn, and M. Meier, "Thin-film silicon solar cell development on imprint-textured glass substrates," (2013). Article in press.

[101] J. G. R. W. M. G. D. D. M. Callahan, C. Battaglia, C. R. Bukowsky, C. Ballif, R. Grubbs, and H. A. Atwater, "Solar cell efficiency enhancement via light trapping in printable resonant dielectric nanosphere arrays," Phys. Status Solidi A **210**, 255–260 (2013).

[102] E. Garnett and P. Yang, "Light trapping in silicon nanowire solar cells," Nano Lett. **10**, 1082–1087 (2010).

[103] D. Dimova-Malinovska, "The state-of-the-art and future development of the photovoltaic technologies - the route from crystalline to nanostructured and new emerging materials," J. Phys.: Conf. Ser. **253**, 012007 (2010).

[104] A. Bay, N. André, M. Sarrazin, A. Belarouci, V. Aimez, L. A. Francis, and J. P. Vigneron, "Optimal overlayer inspired by *Photuris* firefly improves light-extraction efficiency of existing light-emitting diodes," Opt. Express **21**, A179–A189 (2013).

[105] H. J. Round, "A note on carborundum," Electr. World **19**, 309 (1907).

[106] R. Braunstein, "Radiative transitions in semiconductors," Phys. Rev. **99**, 1892–1893 (1955).

[107] N. Holonyak and S. F. Bevacqua, "Coherent (visible) light emission from Ga(As1-x Px) junctions," Appl. Phys. Lett. **1**, 82–83 (1962).

[108] S. Nakamura, T. Mukai, and M. Senoh, "Candelaclass highbrightness InGaN/AlGaN doubleheterostructure bluelight emitting diodes," Appl. Phys. Lett. **64**, 1687–1689 (1994).

[109] Http://www.digikey.com/us/en/techzone/lighting/resources/articles/led-efficacy-improvement.html, April 9th 2013.

[110] "Haitz's law," (2007). Nat. photonics **1**, 23.

[111] R. F. Leulmi, "Réalisation de sources lumineuses à haut rendement lumen/$ à base d'hétérostructures GaN/AlGaN," Master's thesis, Université de Sherbrooke (2008).

[112] D. Lynch, W. Hunter, and E. Palik, *Handbook of Optical Constants of Solids II* (Academic Press, Inc., 1991).

[113] J. Ho, C.-S. Jong, C. C. Chiu, C.-N. Huang, and K.-K. Shih, "Low-resistance ohmic contacts to p-type GaN achieved by the oxidation of Ni/Au films," J. Appl. Phys. **86**, 4491–4497 (1999).

[114] J. Smalc-Koziorowska, S. Grzanka, E. Litwin-Staszewska, R. Piotrzkowski, G. Nowak, M. Leszczynski, P. Perlin, E. Talik, J. Kozubowski, and S. Krukowski, "Ni-Au contacts to p-type GaN - structure and properties," Solid State Electron. **54**, 701–709 (2010).

[115] W. C. Chong and K. M. Lau, "Comparison of Ni/Au, ITO, and ATO-based current spreading layers for near-ultraviolet light-emitting diodes," Phys. Stat. Sol. **4**, 2646–2649 (2007).

[116] K. F. Stanger-Hall, J. E. Lloyd, and D. M. Hillis, "Phylogeny of north american fireflies (coleoptera: Lampyridae): implications for the evolution of light signals." Mol. Phylogenet. Evol. **45**, 33–49 (2007).

[117] M. A. Branham and J. W. Wenzel, "The origin of phoric behavior and the evolution of sexual communication in fireflies (Coleoptera: Lampyridae)," Cladistics **19**, 1–22 (2003).

[118] S. Stock, *Microcomputed* T*omography* - M*ethodology and* A*pplications* (CRC Press, Boca Raton, FL, 2009).

[119] P. Cloetens, W. Ludwig, J. Baruchel, D. V. Dyck, J. V. Landuyt, J. Guigay, and M. Schlenker, "Holotomography: Quantitative phase tomography with micrometer resolution using hard synchrotron radiation x-rays," Appl. Phys. Lett. **75**, 2912–2014 (1999).

[120] P. Cloetens, R. Barrett, J. Baruchel, J.-P. Guigay, and M. Schlenker, "Phase objects in synchrotron radiation hard x-ray imaging," J. Phys. D: Appl. Phys. **29**, 133–146 (1996).

[121] J. Banhart, ed., *Advanced Tomographic Methods in Materials Research and Engineering (Monographs on the Physics and Chemistry of Materials)* (Oxford University Press, Oxford, 2008).

[122] A. Bay and J. P. Vigneron, "Technique de matrices de transfert pour le calcul des réflectance et transmittance optiques," Revue des questions scientifiques **180**, 241–260 (2009).

[123] J. B. Pendry, *Low Energy Electron Diffraction* (Academic Press, London, 1974).

[124] J. B. Pendry and A. MacKinnon, "Calculation of photon dispersion relations," Phys. Rev. Letters **69**, 2772 (1992).

[125] R.B. Sidje, "Expokit: Software package for computing matrix exponentials." ACM Transactions on mathematical software **24**, 130–156 (1998).

[126] A. Stevenson and M. Waite, eds., *Concise Oxford English Dictionary* (Oxford University Press, Oxford, UK, 2011), 12th ed.

[127] W. L. Wolfe, *Introduction to radiometry* (SPIE Optical engineering press, Washington, 1998).